Vortices of Light and their Interaction with Matter

A thesis submitted in partial fulfillment of

the requirements for the degree of

Doctor of Philosophy

by

Shashi Prabhakar

(Roll No. 11330013)

Under the guidance of

Prof. R. P. Singh

Theoretical Physics Division

Physical Research Laboratory, Ahmedabad, India.

DISCIPLINE OF PHYSICS

INDIAN INSTITUTE OF TECHNOLOGY GANDHINAGAR

2014 - 2015

to

my family

Declaration

I declare that this written submission represents my ideas in my own words and where others' ideas or words have been included, I have adequately cited and referenced the original sources. I also declare that I have adhered to all principles of academic honesty and integrity and have not misrepresented or fabricated or falsified any idea/data/fact/source in my submission. I understand that any violation of the above can cause disciplinary action by the Institute and can also evoke penal action from the sources which have thus not been properly cited or from whom proper permission has not been taken when needed.

Shashi Prabhakar

(Roll No: 11330013)

Date: April 6, 2015

Thesis Approval

The thesis entitled

Vortices of Light and their Interaction with Matter

by

Shashi Prabhakar
(Roll No. 11330013)

is approved for the degree of

Doctor of Philosophy

Prof. R. P. Singh (Supervisor)	Dr. Goutam K. Samanta (DSC Member)
Prof. Jitesh R. Bhatt (DSC Member)	Prof. S. Ramachandran (Academic Chairman)

Date: April 7, 2015

Place: PRL, Ahmedabad

Acknowledgements

This thesis is the result of a very nice and revealing research time during 2009-14 at Physical Research Laboratory (PRL), Ahmedabad. It gives me a great pleasure to acknowledge all those who supported me directly or indirectly and made this thesis possible.

First and foremost, I wish to express my sincere thanks to my supervisor, Prof. R. P. Singh, for giving me the opportunity and the resources to conduct my doctoral research program at PRL. I owe my deep sense of gratitude to him. I am also very thankful to him for constant guidance that he has provided throughout my research endeavor. He helped in my study to large extent from basics of optics to image analysis as well as from independent thinking to scientific writing. His persistent support, far-sighted guidance and broad scientific experience made my research work possible. It is a great privilege for me to get a companionship with him. I consider myself fortunate to have him as my supervisor.

I thank Prof. J. N. Goswami, Director; Mr. Y. M. Trivedi and Wg. Cdr. (Retd.) Vibhas Gupta, Registrar; Prof. A. Joshipura, Prof. U. Sarkar, Prof. A. K. Singhvi and Prof. S. Rindani, former Deans of PRL; Prof. Prof. P. Janardhan, present Dean; Prof. S. Rindani, former area chairman and Prof. S. Mohanty current area chairman, for providing necessary facilities to carry out research work. I thank Dr. Goutam K. Samanta and Prof. Jitesh R. Bhatt for reviewing the work and motivating constantly during these five years.

I am highly obliged to Prof. J. Banerji for his suggestions and critical comments which helped me to improve scientific outcomes. The fruitful discussions with him always helped me to improve the quality of the scientific results and manuscripts. A big thank you for Dr. Goutam K. Samanta who has helped in keeping the motivation for perfectness inside me. Discussions on fundamentals and experimental techniques with Dr. Samanta was always enjoyable and fruitful.

I thank Prof. J. S. Ray, Prof. Angom D. Singh, Dr. D. Banerjee, Dr. N. Mahajan, Prof. R. Rangarajan, Mr. T. Sarvaiya, Prof. H. Mishra and Prof. K. P. Subramanian for teaching the courses during my course work at PRL which turned out to be very useful in tenure of research work. In this petabyte era of computational capabilities, data handling and computations have been a very crucial but tedious task. In this regard, I thank all the staff members of PRL computer center for providing excellent computational and internet facilities. Especially, I must acknowledge the help received from Jigar Raval, Samuel Johnson, Hitendra Mishra, Alok Srivastava and Tejas Sarvaiya from computer center. In addition, I express my appreciation for the co-operation and help extended by the library and *its staff members in general and Mrs. Nistha Anilkumar and Pragya Pandey in particular.*

I take this opportunity to thank my seniors, Ashok Kumar and Pravin Vaity, who introduced me to the world of Optics and paved a smooth way for further research in this area. Sincere discussion with them and sometimes "not" receiving ready made answers helped me a lot in understanding the subject. The work culture maintained by Ashok and Pravin in the lab was highly motivational. I am also thankful to Sunita Kedia from whom I have learnt "not busy" attitude. I have learnt a lot from Virendra Jaiswal and Jitendra Bhatt, whose occasional visits to lab were very informative.

I am thankful to all my colleagues, Gangi, Aadhi, Chithra, Apurv, Vinayak, Jabir, Ali and Vinayak in Lab for being friendly and co-operative during this research journey. Our academic and non-academic discussions have made my stay enjoyable and eventful in lab. I have learned a lot about different fields in which my colleagues are working. In one way, I have learnt about different fields, and not just one in the last five years of my life. I would like to thank the visitors which include summer and engineer trainees, particularly to Aabhaas, Shaival, Kinchit, Binal, Chirag, Mehul, Gaurav, Megh and others.

My special thanks and gratitude goes to my batchmates Devagnik, Fazlul, Kabitri and Tanushree. Their presence has made me feel that I am not alone and someone is there to care for me during odd days. Special thanks to Fazlul who has helped me in some of my experiments. He has also helped me in numerical techniques and computer related issues.

I would like to thank Prof. Sudhir K. Jain, Director; Prof. Amit Prashant, Dean; Prof. B. Datta, associate Dean; and the academic section of Indian Institute of Technology, Gandhinagar for the support and help. Special thanks to Mr. Piyush for his prompt response and help during registration.

This acknowledgement section remains incomplete if there is no mention of my wonderful seniors cum friends who were always there to support and help at my stay in hostel. My sportsman spirit became alive after I saw them playing volley ball, badminton and table tennis. My seniors Arun, Amrendra, Sunil, Siddharth, Koushik, Chinmay, Sushant and Yogita have helped to keep my loneliness away from me. I am also thankful to Ashwini, Arvind Singh, Pankaj, Vineet, Neeraj, Prashant, Bhaswar, Sandeep, Vimal, Ketan, Sudhanwa, Suman, Amzad, Srikant, Satinder, Arvind Saxena for making my stay comfortable. In addition, I express my sincere thanks to my dear juniors Avdhesh, Damu, Lekshmy, Midhun, Anjali, Arko, Bhavya, Dillip, Gaurav, both Girish, Gulab, Monojit, Naveen, Priyanka, both Tanmoy, Yashpal, Dinesh, Upendra, Wageesh, Arun, Gaurava, *Abhaya, Anirban, Guru, Ikshu, Kuldeep, Manu, Shraddha, Alok, Sanjay, Bivin, Deepak, Dipti, Jinia, Lalit, Rahul, Ashim, Chandana, Newton, Pankaj, Venky, Chandan, Hemant, Kuldeep, Venkata, Navpreet, Prahlad, Satish, Rukmani, Rupa, Yasir, Komal, Manish, Vaidehi, Sneha, Upasana, Lijo and several others who made my stay in PRL pleasant and having a wonderful experience.*

This thesis is incomplete if I do not acknowledge "Google". It has always made my life easier like a friend. Google has not put in such a situation that I have searched something and there was zero result(s). I also thank open-source packages like XUbuntu, Firefox, Zotero, Texmaker, PDFtk and others which had made my work very simple.

I am deeply indebted to my school teachers, specially Ms. Lipika Paul for excellent teaching and encouragement. A special thanks goes to my long time friends Gautam and Tribedi for their constant support and encouragements. Their constant push and motivational chats have helped me to recover from odd times.

Last, but not the least, I would be nowhere around here without the love and support of my parents. Words cannot express my gratitude for my parents, cousins and my family members. Finally, I must also acknowledge the love, support and blessings of friends, teachers, relatives and all known and unknown persons whom I met with or interacted with in life.

(shashi prabhakar)

Abstract

Optical vortices are singularities in the phase distribution of a light field. At the phase singularity, real and imaginary parts of the field vanish simultaneously and associated wavefront becomes helical. For an optical vortex of topological charge l, there are l number of helical windings in a given wavelength λ of light and it carries an orbital angular momentum of $l\hbar$ per photon. This dissertation concerns with the study of interaction of optical vortices with matter namely non-linear optical crystal β-Barium Borate (BBO) and Bose-Einstein condensate.

A new method to determine the order of optical vortex from just the intensity distribution of a vortex has been discussed. We show that the number of dark rings in the Fourier transform (FT) of the intensity can provide us the order. To magnify the effect of FT, we have used the orthogonality of Laguerre polynomials.

We have studied the interaction of optical vortices with BBO crystal. The spatial-distribution of degenerate spontaneous parametric down-converted (SPDC) photon pairs produced by pumping type-I BBO crystal with optical vortices has been discussed. For a Gaussian pump beam, we observe a linear increase in thickness of the SPDC ring with pump size. On the other hand, the SPDC ring due to optical vortex forms two concentric bright rings with an intensity minimum in the middle. We also observe that if the beam size is lower than a particular value for a given topological charge l of the vortex, then there will be no change in full-width at half maximum of the rings formed by down-converted photons.

We have experimentally verified the quantum inspired optical entanglement for classical optical vortex beams. The extent of violation of Bell's inequality for continuous variables written in terms of the WDF increases with the increase in their topological charge. To obtain this, we have used the FT of two-point correlation function that provides us the WDF of such beams.

Quantum elliptic vortex (QEV) is generated by coupling two squeezed vacuum modes with a beam splitter (BS). The Wigner distribution function (WDF) has been used to study the properties of this quantum state. We also study how this coupling could be used to generate controlled entanglement for the application towards quantum computation and quantum information. We observe a critical point above which the increase in vorticity decreases the entanglement.

We have also studied the annihilation of vortex dipoles in Bose-Einstein condensates. To analyze this, we consider a model system where the vortex-antivortex pair and gray soliton generated by annihilation of vortex dipoles are static and the system could be studied within Thomas-Fermi (TF) approximation. It is observed that the vortex dipole annihilation is critically dependent on the initial conditions for their nucleation. Noise, thermal fluctuations and dissipation destroy the superflow reflection symmetry around the vortex and antivortex pair. It is note worthy that some of our theoretical results have already been verified experimentally.

Keywords: Singular optics, Optical vortex, Spontaneous parametric down-conversion, entanglement, Wigner distribution function, Bell's inequality, Vortex dipole annihilation, Bose-Einstein condensates.

Contents

List of Figures

List of Tables

Chapter 1

Introduction

In optics, the concept of phase is important because it provides a visual perception of wave propagation and transformation along its path. The phase in a beam of light is characterized by the wavefront that is a surface of equal phase, which can have regular shapes like planer, spherical, cylindrical and even helical. The superposition of two wavefronts leds to the interference fringes and supported the wave theory of light, similar to Young's double slit experiment [1]. This thesis deals with the beams with helical wavefronts, in particular optical vortices. It includes the interaction of optical vortices with matter namely non-linear optical crystal β-Barium Borate (BBO) and Bose-Einstein condensate.

1.1 Optical vortices

The Laguerre Gaussian (LG) beams are the eigen modes of stable laser resonator which has cylindrical symmetry. These beams form infinite dimensional orthogonal set of solutions. The complex field distribution of LG beams are [2]

$$\begin{aligned} E_{lp}(r,\phi,z) &= \frac{C_{lp}^{LG}}{w(z)}\left(\frac{r\sqrt{2}}{w(z)}\right)^{|l|} \exp\left(-\frac{r^2}{w^2(z)}\right) L_p^{|l|}\left(\frac{2r^2}{w^2(z)}\right) \\ &\times \exp\left(ik\frac{r^2}{2R(z)}\right)\exp(il\phi)\exp\left[i(2p+|l|+1)\zeta(z)\right], \end{aligned} \tag{1.1}$$

where p and l are the radial and the azimuthal indices which represent orders of associated Laguerre polynomial $L_l^p()$. C_{lp}^{LG} is the normalization constant, and

$w(z)$, $R(z)$ and $\zeta(z)$ are beam parameters. These beams contain p dark rings in their intensity profile with a π phase jump.

Due to azimuthal phase term $\exp(il\phi)$, they have a twist of $2l\pi$ in their wavefront which acts as a screw dislocation [3, 4] and produces a vortex. The factor l is called as the order of the vortex or its topological charge, which determines how many times the phase should change by 2π on one complete rotation around the center of the vortex [5]. This generates phase singularity in the wavefront. Due to the same twist, these beams carry an orbital angular momentum (OAM) of $l\hbar$ per photon [6].

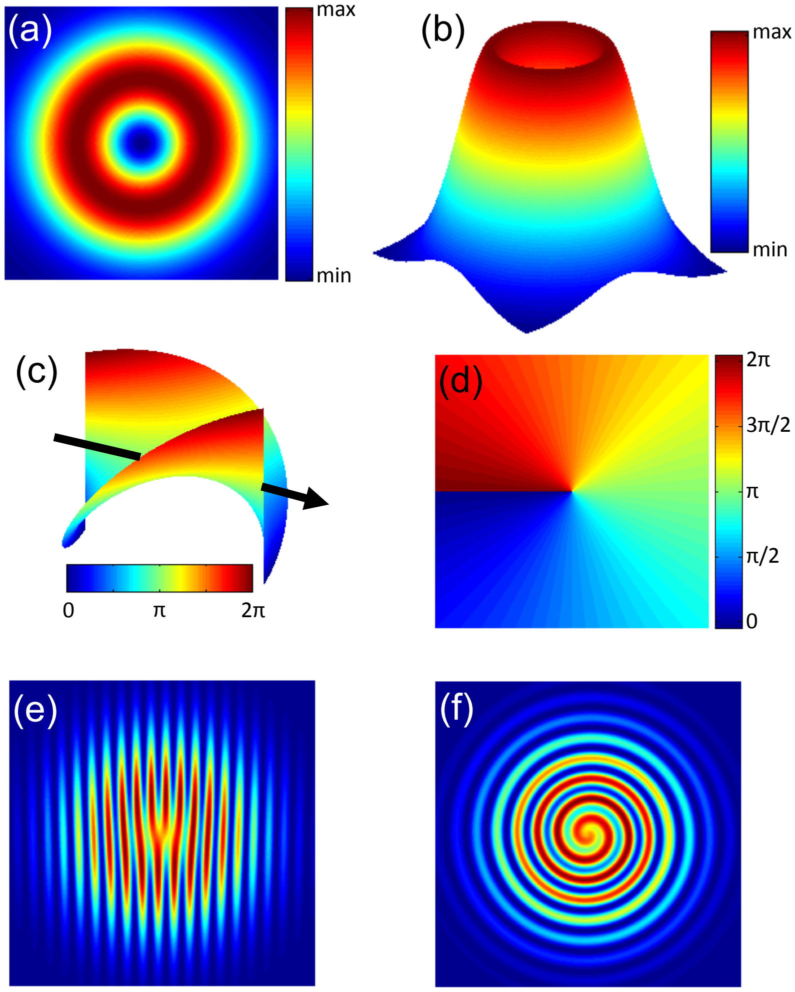

Figure 1.1: Optical vortex of order +1. (a, b) 2D and 3D intensity profile (c) wavefront (d) phase profile and (e, f) interference pattern with a plane reference beam and spherical beam.

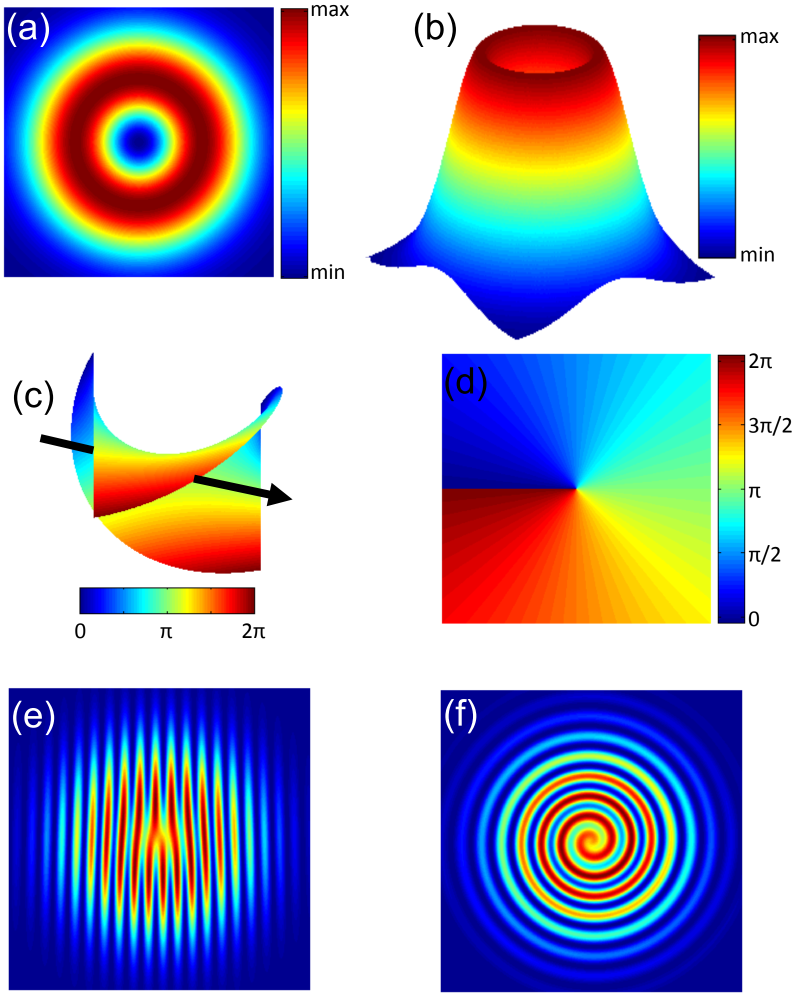

Figure 1.2: Optical vortex of order −1. (a, b) 2D and 3D intensity profile (c) wavefront (d) phase profile and (e, f) interference pattern with a plane reference beam and spherical beam.

When p=0, Eq. 1.1 reduces to a vortex beam equation

$$\begin{aligned} E_l(x,y,z) &= E_0(x+\text{sgn}\ iy)^l \frac{w_0}{w(z)^{l+1}} \exp\left(-\frac{x^2+y^2}{w(z)^2}\right) \\ & \exp\left(ik\frac{x^2+y^2}{2R(z)}\right) \exp\left(ikz - i(l+1)\zeta(z)\right), \end{aligned} \tag{1.2}$$

where sgn denotes the sign of topological charge which is +1 for positive and −1 for negative. The intensity profiles and the phase profiles for different indices $p = 0$, $l = +1$ and $p = 0$, $l = -1$ have been shown in Fig. 1.1 and Fig. 1.2 respectively. One can verify that Eq. 1.1 reduces to the Gaussian beam expression for p=0 and l=0, which has been shown in Fig. 1.3.

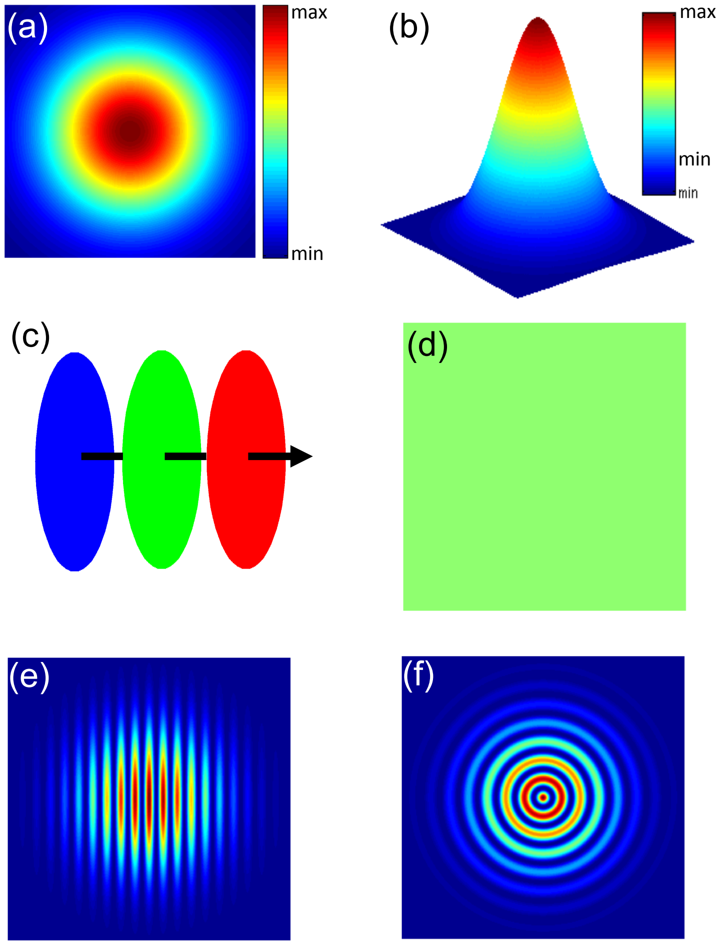

Figure 1.3: Gaussian beam. (a, b) 2D and 3D intensity profile (c) wavefront (d) phase profile and (e, f) interference pattern with a plane reference beam and spherical beam.

Optical vortices can also be observed in scattering of laser beam through rough surfaces or ground glass [7], however in laboratory, they can also be generated in a controlled manner [8]. In the speckle patterns formed by scattering of laser beams, many dark spots are observed which are actually optical vortices of order ± 1. These are formed by the interference of many scattered waves [9]. In isotropic random fields, the probability of creating positive and negative-charge vortex is the same, so the sum of all the vortex charges remains zero.

This OAM can be transferred to micron-sized particles placed along the propagation axis. This property of Laguerre-Gaussian beams finds practical interest in the field of optical trapping and micro-machining [10]. It must be noted that the OAM of LG beams are different from the angular momentum due to the polarization of light. These beams have found a variety of applications, such as in the optical trapping of atoms [11], optical tweezing and spanning [10], optical communication [12], imaging [13], and quantum information and computation [14].

1.2 Orbital angular momentum (OAM) of light

Light carries a linear momentum equivalent to $\hbar k$ per photon and, if circularly polarized, a spin angular momentum (SAM) of $\pm\hbar$ per photon [15]. In 1992, Allen et al. recognized that light beams with an azimuthal phase dependence of $\exp(il\phi)$ carry an orbital angular momentum (OAM) of $l\hbar$ per photon [6, 16, 17] that can be many times greater than the SAM and that such beams were readily realizable. This OAM is completely distinct from the familiar SAM, most usually associated with the photon spin, that is manifest as circular polarization.

The origin of OAM is easier to understand. The simplest example of a light beam carrying OAM is one with a phase in the transverse plane of $\Phi(r, \phi) = r^l \exp(il\phi)$ (simplified version of Eq. 1.2) where ϕ is the angular coordinate and l can be any integer, positive or negative. These beams have helical phase fronts with the number of intertwined helices and the handedness depending on the magnitude and the sign of l, respectively. One can see immediately that an electromagnetic field transverse to these phase fronts has axial components. Equivalently, the Poynting vector, which is at all times parallel to the surface normal of these phase fronts, has an azimuthal component around the beam and hence an angular momentum along the beam axis exists.

1.3 Interaction of optical vortices with non-linear crystal

Nonlinear optics is the study of phenomena that occur as a consequence of the modification of the optical properties of a material system by the presence of light.

Typically, only laser light is sufficiently intense to modify the optical properties of a material system. For example, second-harmonic generation occurs as a result of the atomic response that scales quadratically with the strength of the applied optical field.

In non-linear optics, the optical response can be described by expressing the polarization $\overrightarrow{P}(t)$ as a power series in the field strength $\overrightarrow{E}(t)$ [18],

$$\begin{aligned}\overrightarrow{P}(t) &= \epsilon_0 \left[\chi^{(1)}\overrightarrow{E}(t) + \chi^{(2)}\overrightarrow{E}^2(t) + \chi^{(3)}\overrightarrow{E}^3(t)\ldots\right] \\ &= \overrightarrow{P}^{(1)}(t) + \overrightarrow{P}^{(2)}(t) + \overrightarrow{P}^{(3)}(t)\ldots \end{aligned} \tag{1.3}$$

where the constant $\chi^{(1)}$ is known as linear susceptibility and ϵ_0 is the permittivity of free space. The quantities $\chi^{(2)}$ and $\chi^{(3)}$ are known as the second and third-order non-linear susceptibilities.

Nonlinear effects fall into two categories – parametric and non-parametric effects. A parametric non-linearity is an interaction in which the property of the nonlinear material is not altered by the interaction with the optical field. As a consequence of this, the process is 'instantaneous' and the total energy is conserved. This makes the phase matching polarization dependent. In non-parametric non-linearly, the property of the nonlinear material gets altered while interaction with the optical field and the energy conservation rule is not satisfied.

The nonlinear effects in certain crystals have been exploited in a number of applications such as frequency doubling, optical parametric oscillation and spontaneous parametric down-conversion [18, 19]. These phenomena can occur when an input electric field interacts with the dielectric properties of the medium in a nonlinear way. The phenomena of SPDC were first observed by Burnham and Weinberg [20] and theoretically studied by Hong and Mandel [19].

1.3.1 Spontaneous parametric down-conversion (SPDC)

The process of spontaneous parametric down-conversion (SPDC) has been used extensively for the generation of entangled photon pairs in many recent experiments. The purpose of these experiments range from Bell's inequality violation [21] to the implementation of quantum information protocols [22]. In the process of SPDC, a laser pump beam photon interacts with second-order nonlinear $\chi^{(2)}$ crystal, gets annihilated and gives rise to the emission of two photons. These two photons are generated simultaneously and follow the laws of energy and momentum conservation.

When a nonlinear crystal, for example Beta Barium Borate (β-BaB_2O_4), with a second order nonlinear susceptibility ($\chi^{(2)}$) is pumped by a highly intense laser, a *pump* photon (frequency ω_p and wave vector $\mathbf{k}_p$) splits into two photons called *signal* and *idler*. These two photons are generated simultaneously inside the crystal. This process is governed by energy and momentum conservation as

$$\hbar\omega_p = \hbar\omega_s + \hbar\omega_i, \tag{1.4}$$

$$\hbar\mathbf{k}_p = \hbar\mathbf{k}_s + \hbar\mathbf{k}_i \tag{1.5}$$

where ω is the frequency, $\mathbf{k}$ is the wave vector and suffices s and i denote signal and idler photons respectively. This information has been pictorially shown in Fig 1.4. The phase matching is determined by the frequency of the pump laser beam, and the orientation angle of the crystal's optic axis with respect to the pump.

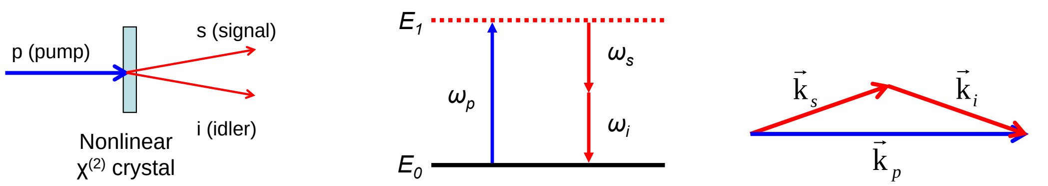

(a) SPDC Process (b) Energy Conservation (c) Momentum Conservation

Figure 1.4: Conservation laws in the process of SPDC.

SPDC is stimulated by random vacuum fluctuations [23, 24], and hence the photon pairs are created at random times. The conversion efficiency of SPDC is very low, on the order of 1 pair for 10^{12} incoming pump photons [25]. However, from one of the pair, if *signal* is detected at any time then its partner *idler* is known to be present [20].

1.3.2 Types of SPDC process

Based on the polarization of generated photons and phase-matching conditions, SPDC is classified into two types – type-I and type-II [26].

Type-I SPDC

In this process, the down-converted photons have same polarization [27]. This process is o → e + e type interaction and hence produces a single cone. In crystallography, o and e represent ordinary and extra-ordinary rays inside birefringent crystals. These also represent horizontally and vertically polarized light based on the birefringence of the crystal. Ring structure formed by the cone is shown in Fig. 1.5. The output of a type-I down-converted photon pair is a squeezed vacuum state that contains only even photon number terms [28].

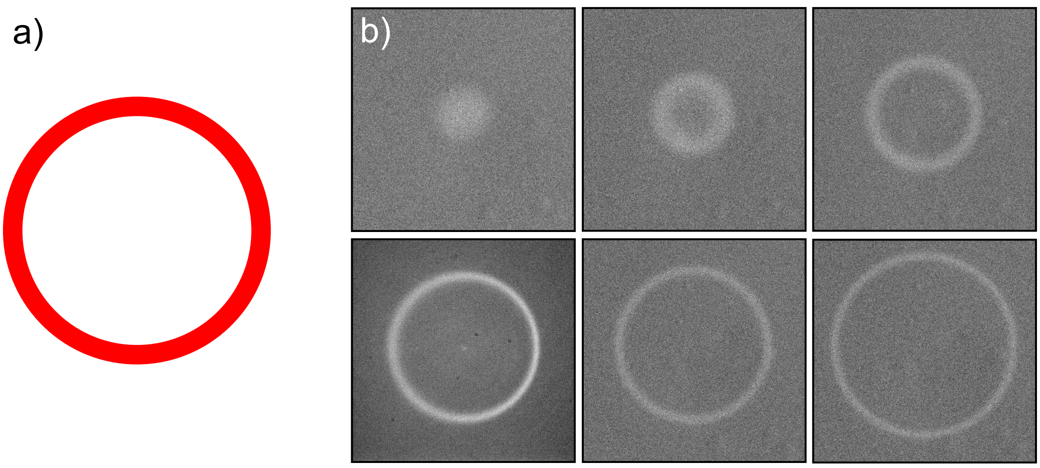

Figure 1.5: a) Theoretical and b) experimentally obtained ring structures formed by type-I SPDC process produced by pumping with a Gaussian beam. Experimental SPDC rings are obtained at different orientations of the crystal. Changing orientation of the crystal changes the thickness as well as the diameter of the SPDC ring. The center of the ring does not change by changing the crystal's orientation.

Type-II SPDC

In this process, the two down-converted photons have orthogonal polarizations [29, 30]. This process is o $\rightarrow$ o + e type interaction and produces two cones. Ring structure formed due to the two cones is shown in Fig. 1.6. One ring corresponds to o-ray and other ring corresponds to e-ray. The output of the type-II down-converted photon pair is a two-mode squeezed vacuum.

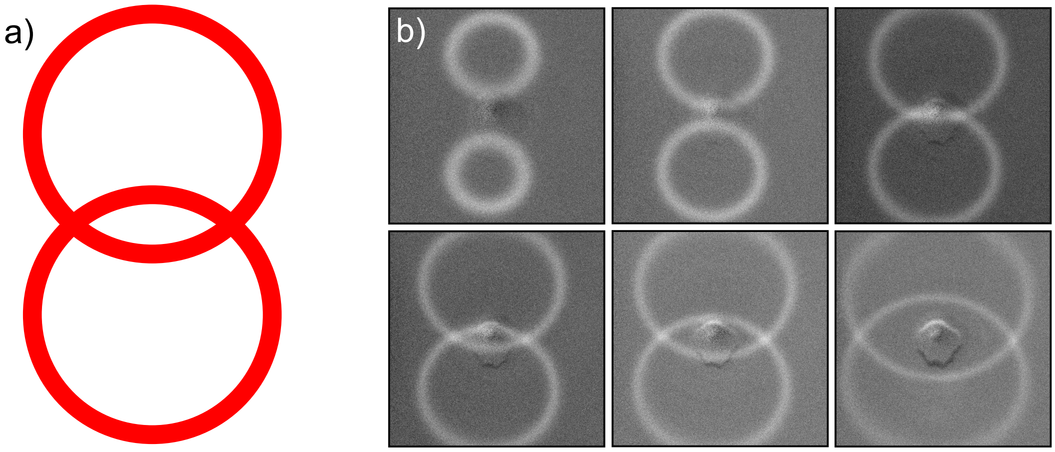

Figure 1.6: a) Theoretical and b) experimentally obtained ring structures formed by type-II SPDC process produced by pumping with a Gaussian beam. Experimental SPDC rings are obtained at different orientations of the crystal. Changing orientation of the crystal changes the thickness as well as the diameter of the SPDC ring. The seperation between the center of two rings does not change by changing the crystal's orientation.

1.4 Quantum elliptic vortex (QEV) state

Quantum elliptic vortex (QEV) can be generated in signal photon mode by coupling squeezed coherent states of two modes with beam splitters or a dual channel directional coupler (DCDC) [31]. The quantum interference due to the coupling between the two modes generates the controlled entanglement for quantum computation and quantum tomography. Although, Agarwal et al. have studied the properties of a generic vortex wave function of the form $(x \pm iy)^m$, which is perfectly symmetric, however, no real physical system can exhibit perfect symmetry. Therefore, a generalized quantum elliptic vortex provides a more realistic and more widely applicable vortex model.

Following the mathematical treatments of [32], with the choice of the parameters, $\eta_i = 1/(\sqrt{2}\sigma_i)$, for $i = x, y$, one can calculate the normalized spatial distribution of displaced QEV state of charge m as

$$\begin{aligned}\Psi^D_{qev}(x,y) &= \sqrt{\frac{2^{m-2}}{\sigma_x\sigma_y\Gamma(m+\frac{1}{2})\sqrt{\pi}}}\left[\frac{x-x_0}{\sqrt{2}\sigma_x} \pm \frac{y-y_0}{\sqrt{2}\sigma_y}\right]^m \\ &\times \exp\left[-\frac{1}{2}\left\{\left(\frac{x-x_0}{\sigma_x}\right)^2 + \left(\frac{y-y_0}{\sigma_y}\right)^2\right\}\right] \qquad (1.6)\end{aligned}$$

where $\sigma_i = \exp(2\zeta_i)$. It is centered at a point $(x_0,\ y_0)$, where $x_0 = \Re e(\alpha_x)$ and $y_0 = \Re e(\alpha_y)$. ζ is the squeezing parameter. A quantum state is said to be squeezed when the noise in one variable is reduced below the symmetric limit at the expense of the increased noise in the conjugate variable such that the Heisenberg uncertainty relation is not violated i.e. $\triangle x \times \triangle p_x = const.$ α is the eigenstates of the annihilation operator of coherent states $|\alpha\rangle$. The distribution $|\Psi^D_{eev}(x,y)|^2$ is shown to have elliptic vortex structure, with zero intensity at $(x_0,\ y_0)$, i.e. the point of displacement of the vacuum. The density and phase function is shown in Fig. 1.7 for $m = 1$. Inverting the ratio σ_x/σ_y rotates the ellipse by $\pi/2$. In this case, the two axes x, y are the defined as the quadratures, and not as spatial dimensions. Quadratures are similar to phase-space dimensions. In this type of study, the electric field for the optical beam are considered quantum mechanically and represented as a quantum state.

To study the properties of quantum states a number of (quasi)probability distributions have been defined. However, among all the (quasi)probability distributions, the Wigner function stands out, as it is real, nonsingular, yields correct quantum-mechanical operator averages in terms of phase-space integrals, and possesses positive definite marginal distributions [33]. Once the Wigner distribution is known, the other properties of the system can be calculated. Keeping this in mind we calculated the Wigner function of the QEV states [31]. We observed quantum interferences due to coupling between the two modes of the vortex.

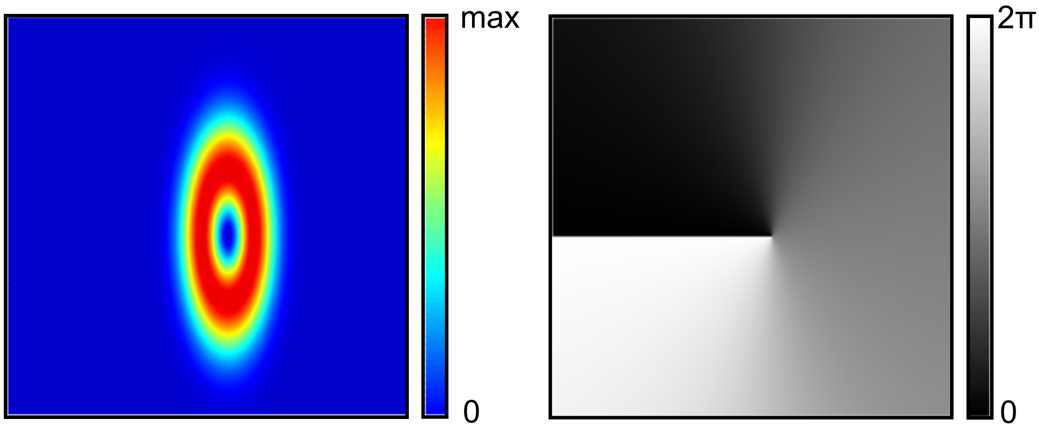

Figure 1.7: Density function (left) and phase (right) of an quantum optical elliptical vortex state. Here $\sigma_y = 1$, $\sigma_x/\sigma_y = 0.7$, $x_0 = y_0 = 0.3\sigma_y$ and $m = 1$.

1.5 Propagation of optical vortex in free space

A vortex embedded at the center of a Gaussian beam, when propagates in free space, the position of the vortex does not change while propagation. However, an off-axis vortex rotates about the center of beam during propagation [34]. This phenomena is clearly visible in Fig. 1.8.

The propagation of a vortex dipole has attracted a lot of interest since the last decade [35, 36, 37, 38, 39]. Bazhenov et al. [35] have experimentally generated the pair of vortices in a single beam by using diffraction gratings for the first time. Indebetouw studied the propagation of an array of vortices through free space and showed that the relative separation between the vortices is invariant during the propagation in the case of same type (sign) of charges whereas they will attract and annihilate each other in the case of oppositely charged vortices [36]. Chen and Roux have studied the annihilation of dipole vortices during their propagation as shown in Fig. 1.9. They found that the background phase function at a point where two dipoles annihilate have a continuous potential, which is the result of annihilation. They have used the same background phase function to accelerate the annihilation process [39]. Recently, the tight focusing properties and the propagation dynamics of a pair of vortices have been investigated theoretically [40, 41].

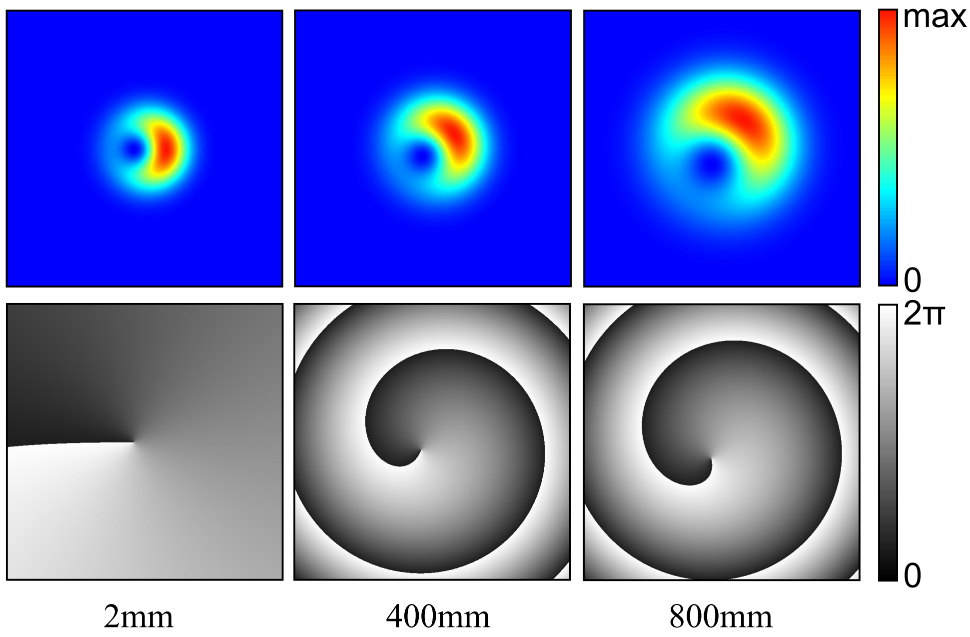

Figure 1.8: Free space propagation of an off-axis vortex beam with charge +1 at a distance of $0.3w_0$ from the center: intensity (top) and phase (bottom). Images are taken at distances 2 mm, 400 mm and 800 mm from waist plain.

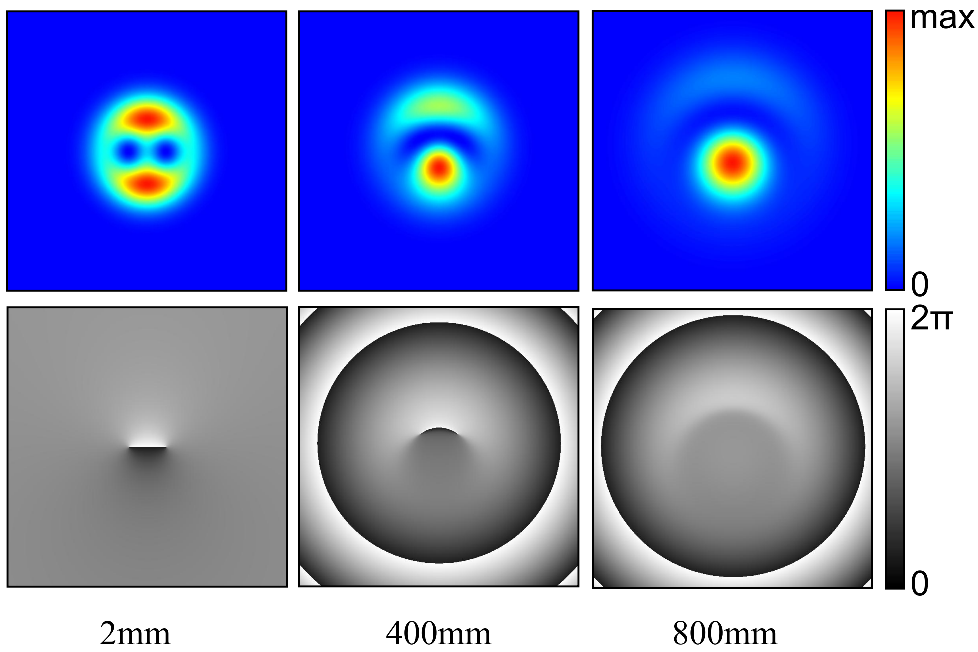

Figure 1.9: Free space propagation of a vortex dipole with charges (+1, −1) seperated by a distance of $0.6w_0$ symmetrically along the center: intensity (top) and phase (bottom). Images are taken at distances 2 mm, 400 mm and 800 mm from waist plain.

The propagation of vortices in a non-linear medium, like Bose-Einstein Condensate, has garnered a lot of interest for their importance to the fluid system. When an obstacle steers the condensate, vortex and vortex dipoles gets generated around the obstacle. The dynamics of these generated vortex and vortex dipoles holds a very important place in the field of hydrodynamics. As we have seen from Fig. 1.9 that when vortex dipoles propagate in free space, they get annihilated. We have attempted to study the steering of BEC with optical vortex which has not been studied earlier.

1.6 Vortices in Bose-Einstein condensate

At normal temperature and pressure, both bosonic and fermionic type of gases obey Maxwell-Boltzmann statistics, and consequently very difficult to differentiate one from the other. However, when the temperature of these gases are lowered ($\sim 10^{-9}K$), the inherent properties of bosonic and fermionic gases become significant and show different behavior. In case of bosons, lowering the temperature below a critical temperature T_c leads to the macroscopic occupation of the single particle ground state; whereas in case of fermions, the system enters into a state with a filled Fermi sea. One parameter which characterizes this transition is phase space density, which is defined as the number of particles occupying the volume equal to the cube of thermal de-Broglie wavelength λ_T [42]. At T_c, phase space density becomes of the order 1 and the system can be considered as quantum degenerate. The quantum degenerate bosonic system is also called Bose-Einstein condensate (BEC).

The gases in Bose-Einstein condensate state act as superfluid [43, 44]. One effect of this is that the viscosity becomes zero, meaning that normal rules of surface tension, such as capillarity, are no longer obeyed. A superfluid in a glass tube will literally “crawl” up the side of the tube in a thin film because of this property. This superfluidic system can be considered as one of the best system to study basic and fundamental theories of hydrodynamics at zero viscosity and zero temperature. One such study is the formation and annihilation of vortex dipoles. Vortices in BEC can be considered as basic excitations in the superfluids [42].

One of the important developments in recent experiments on atomic Bose-Einstein condensates (BECs) is the creation of vortices and the study of their dynamics [45, 46]. Equally important is the recent experimental observation of a vortex dipole, which consists of a vortex-antivortex pair, when an obstacle moves through a BEC [47] and observation of vortex dipoles produced through phase imprinting [48, 49]. In superfluids, the vortices carry quantized angular momenta and are the topological defects, which often serve as the conclusive evidence of superfluidity. In a vortex dipole, vortices of opposite circulation cancel each other's angular momentum and thus carry only linear momentum. This is the cause of several exotic phenomena like leap frogging, snake instability [50], orbital motion [51], trapping [52], and others. The effects of vortices are widespread in classical fluid flow [53] and optical manipulation [10]. A good description of vortices in superfluids is given in Ref. [42] and review articles [54, 55]. More detailed discussion of vortices is given in Ref. [56]. Number density and phase profile of a vortex dipole have been shown in Fig. 1.10. The sense of rotation of phase around the center of vortices are opposite of each other that shows the presence of a dipole.

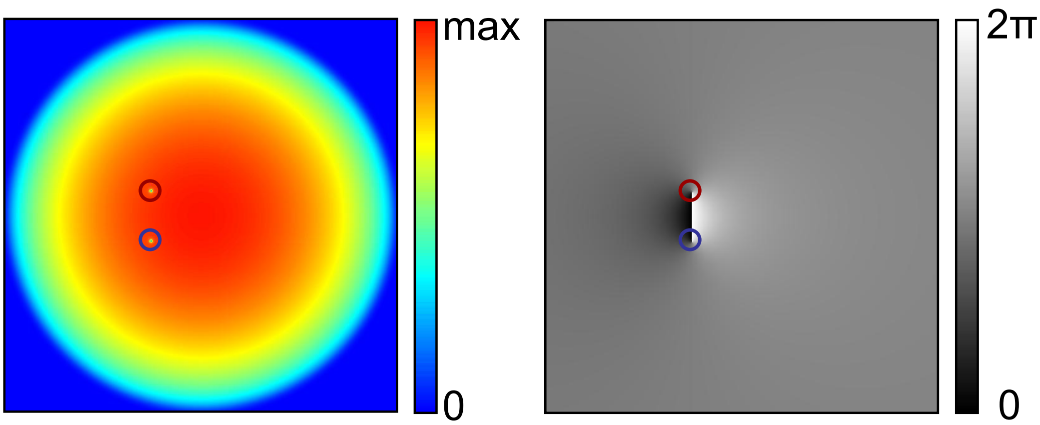

Figure 1.10: Number density (left) and phase (right) profile of condensate with vortex dipole. Two oppositely charged vortices are marked with two differently colored circles.

1.6.1 Trajectory of a vortex-dipole

The motion of a vortex ring in a trapped BEC may be understood in terms of two contributions to the velocity of each element in the ring. First, the precession due to the inhomogeneity of the condensate and secondly, the velocity induced by the other rings. In the present case, we have considered highly oblate BEC with few well separated vortex dipoles, hence the contribution due to the other rings can be neglected. The velocity on each element is then given by

$$\mathbf{v} = \omega_p \hat{\mathbf{k}} \times \mathbf{r} \tag{1.7}$$

where $\hat{\mathbf{k}}$ defines the direction of the circulation at the element, and ω_p is the precession frequency. This equation can be reduced to two equations in $x - y$ plane as

$$\frac{dx}{dt} = -\omega_p y + \frac{1}{2y} \tag{1.8}$$

$$\frac{dy}{dt} = \omega_p x \tag{1.9}$$

These two equations govern the motion of the vortex dipoles. The solution of these equations is shown in Fig. 1.11.

From the Fig. 1.11, one can observe that the vortex dipole come closer only along the diameter of the BEC, if they are generated symmetrically along the diameter of condensate. In the course of their motion, they can even be closer than the coherence length. However, vortex-dipole with a separation less than the coherence length is an ambiguous situation.

Among the important phenomena associated with the Bose-Einstein condensate (BEC), the creation, dynamics, and annihilation of vortex dipoles carry useful information associated with the system. Several methods have been suggested to nucleate vortices and recently, nucleation of the vortices has been observed experimentally by passing a Gaussian obstacle through the BEC with a speed greater than some critical speed [47]. The trajectories of these vortex dipoles are ring-structured as described in Refs. [57, 58] and shown in Fig. 1.11.

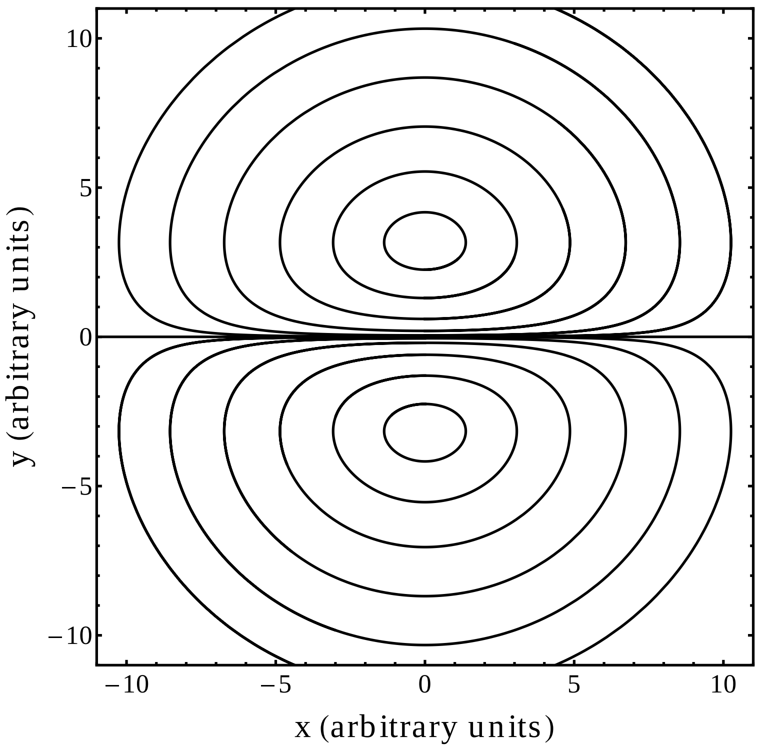

Figure 1.11: The trajectories of the vortex dipole in oblate BEC calculated numerically from the equation of motion (Equations 1.8 and 1.9). The energy is same in every case. The trajectories depend upon location of generation of vortex dipoles.

1.7 Aim of the thesis

Optical vortices have importance in various applications which include optical trapping and tweezing, optical communication, and quantum information and computation. Therefore, the study of their interaction with matter becomes an essential necessity. In this thesis work, we have characterized vortices and studied their linear as well as nonlinear interactions with matter.

1.8 Thesis overview

Chapter 1 contains the basic introduction of the subject i.e. optical vortices, spontaneous parametric down-conversion process. Basics of entanglement with quantum optical elliptical vortex state along with correlation properties for optical vortex beams similar to quantum entanglement are also discussed. The vortex dipoles and their dynamics in Bose-Einstein condensates including the review of the background material form a substantial part of the chapter. Chapter 2 is devoted towards the generation and characterization of optical vortices. This chapter discusses a method for the detection of order of vortices using their intensity distribution recorded with the CCD camera.

Chapter 3 focuses on the interaction of optical vortices with non-linear crystal. One such interaction is spontaneous parametric down-conversion (SPDC). This chapter discusses the spatial distribution of SPDC photons when the non-linear crystal is pumped with optical vortices. The process of SPDC generates photons in entangled states. Chapter 4 discusses the classical entanglement for an optical vortex beam which contains singularity. This chapter covers the experimental verification of entanglement present in such beams. Chapter 5 presents the theoretical study of entanglement of quantum elliptical vortex (QEV). The amount of entanglement of QEV can be controlled using the squeezing parameter. In recent times, entanglement of classical beams has evolved a great deal.

Annihilation of vortex dipoles is observed in optics. However, in case of Bose-Einstein condensates, annihilation is not observed. Chapter 6 deals with the annihilation of vortex-dipoles in Bose-Einstein condensate. This chapter also deals with the thermodynamical stability of vortex dipoles. The last chapter, chapter 7 of the thesis provides the summary and scope for future work.

Chapter 2

Generation of the vortex and finding its order

We know that the optical vortices are the solution of Maxwell equations and they can be generated using an optical cavity and mode-converters. However, they cannot be controlled in real time. To change the mode or beam profile, the whole cavity needs to be modified. To overcome these issues, we use computer generated holography technique for generation of optical vortex beams. The computer generated hologram (CGH) modifies the phase and amplitude of input Gaussian beam in such a way that the diffracted beam from hologram acquires the desired beam profile. Spatial light modulator (SLM) is used to do phase and amplitude modulation in real time. It allows us to change the beam profile along with the topological charge of vortex beams. In recent years with advancement of technology, spiral phase plate (SPP) in the form of vortex lens has been made available in the optical wavelength range which can imprint phase structure of the vortex on a Gaussian beam [59].

In this chapter, we have described the method for generation of optical vortex beams along with their characterization. Section 2.1 starts with the basic principle of conventional holography. The computer generated holography technique is introduced in section 2.1.1. The technique behind SPP is discussed in section 2.1.2. Section 2.2 describes the determination of the order of an optical vortex using the intensity pattern recorded with the CCD camera. The theory for the determination of order using the Fourier transform of the intensity distribution of an optical vortex is discussed in section 2.2.1, results in section 2.2.2 and finally conclude in section 2.2.3.

2.1 Generation of optical vortices

In this section, we discuss about the methods for generating optical vortices. Computer generated holography using spatial light modulators and spiral phase plates are two such commonly used methods in the laboratory.

2.1.1 Computer generated holography

Computer generated holography is one of the easiest methods to generate an optical vortex in laboratory. This technique is based on the principle of holography. In this section, we have discussed computer generated holograms and spatial light modulators.

Computer generated hologram (CGH)

Computer generated hologram (CGH) is an interference pattern of an object beam with a reference beam obtained numerically by using a computer [60, 61, 62]. When we consider the object beam as an optical vortex and the reference beam as a plane Gaussian beam then the interference pattern or hologram looks like a fork pattern. The reduced size of this pattern is either cast on a holographic sheet or printed by a high resolution laser printer on a transparency sheet [60]. On passing a laser beam through the branch point of generated fork pattern we obtain diffraction pattern consisting of various orders of optical vortex in different diffraction orders.

Let us consider the optical vortex of order m as object beam. The electric field for object beam can be written as

$$E_{\mathrm{obj}} = E_0(x \pm iy)^m \exp\left(-\frac{x^2+y^2}{w^2}\right), \tag{2.1}$$

where w is the spot size. In cylindrical coordinate system, E_{obj} can be written as

$$E_{\text{obj}} = E_0 r^m \exp(\pm im\theta) \exp\left(-\frac{r^2}{w^2}\right). \tag{2.2}$$

where $r = \sqrt{x^2 + y^2}$ and $\theta = \tan^{-1}(y/x)$. Considering the plane wave as reference beam, the electric field can be written as

$$E_{\text{ref}} = E_{r0} \exp\left[-i(k_x x)\right]. \tag{2.3}$$

The intensity distribution of the interference of this object and reference beam can be written as

$$I = \left| E_{r0} \exp(-ik_x x) + E_0 r^m \exp(\pm im\theta) \exp(-r^2) \right|^2. \tag{2.4}$$

Considering E_{r0}, E_0 and w as unity, we get the spatially varying transmission function as

$$T = 2\left[1 + \cos\left(k_x x \pm m\theta\right)\right]. \tag{2.5}$$

Apart from sinusoidal transmission function, holograms with other types of transmission functions can also be generated, e.g. for binary hologram, the transmission function becomes

$$T_{binary} = sign\left[2(1 + \cos(k_x x \pm m\theta))\right] \tag{2.6}$$

where $sign(x) = x/|x|$. Binary holograms are much easier to print on transparency sheet than the sinusoidal variation of optical density. Binary hologram has more diffraction efficiency than that of sinusoidal transmission grating.

Blazed gratings are also used to generate optical vortex with high diffraction efficiency in the first diffracted order. The transmission function for such a grating is

$$T_{blazed} = \frac{1}{2\pi} \text{Mod}\left(k_x x \pm m\theta, 2\pi\right) \tag{2.7}$$

where $\text{Mod}(\alpha, \theta)$ is the remainder on division of α by θ. The different kinds of gratings for the formation of an optical vortex of order m=1 have been shown in Fig. 2.1.

Amplitude holograms absorb most of the input power therefore their diffraction efficiency is poor. To overcome this limitation and to maximize the power

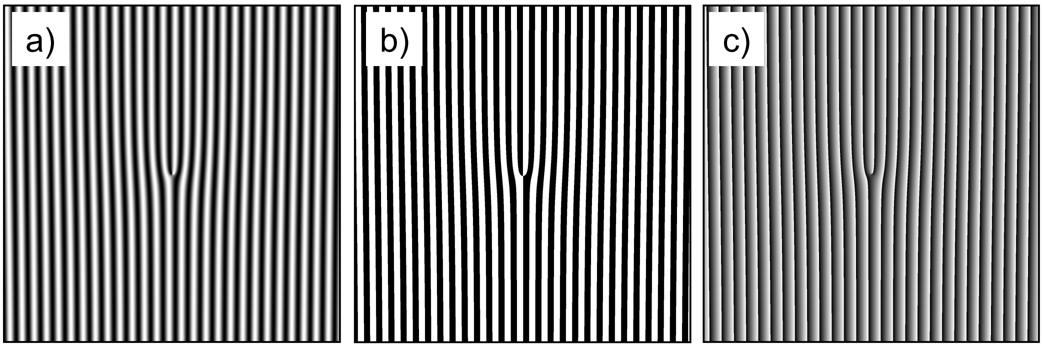

Figure 2.1: Computer generated holograms with different transmission functions for the generation of optical vortex of order 1, a) sinusoidal, b) binary and c) blazed.

of optical vortices phase only holograms are used. These holograms ideally do not absorb any power and modulate the phase of incident light according to the stored interference pattern.

Spatial light modulator (SLM)

Spatial light modulator (SLM) is a device which modulates light in amplitude and phase spatially [63, 64]. SLM consists of large number of square-shaped liquid crystals, arranged in two-dimensional array, in which the orientation of liquid crystal molecules can be altered by applied electric field. In our experiments, we have used SLMs (Holoeye LC-R 2500 and Hamamatsu x10468-05) which work in reflective mode. SLM can be used as a dynamic diffractive optical element.

The numerically obtained fork patterns are transferred into the SLM through the computer interface. The SLMs are connected to the computer using the outputs from graphics card which is installed in the PCI-e $\times 16$ slot. The purpose of the graphics card is to display the same content on both the displays i.e. computer monitor and SLM. The generated video signal corresponds to the input fork pattern displayed on the computer monitor that is transmitted to the SLM. The electrical voltages from the signal align the molecules of liquid crystals to form a fork type pattern. When the reference beam i.e. laser beam is incident on the SLM it results into optical vortices as diffracted orders and is shown in Fig. 2.2.

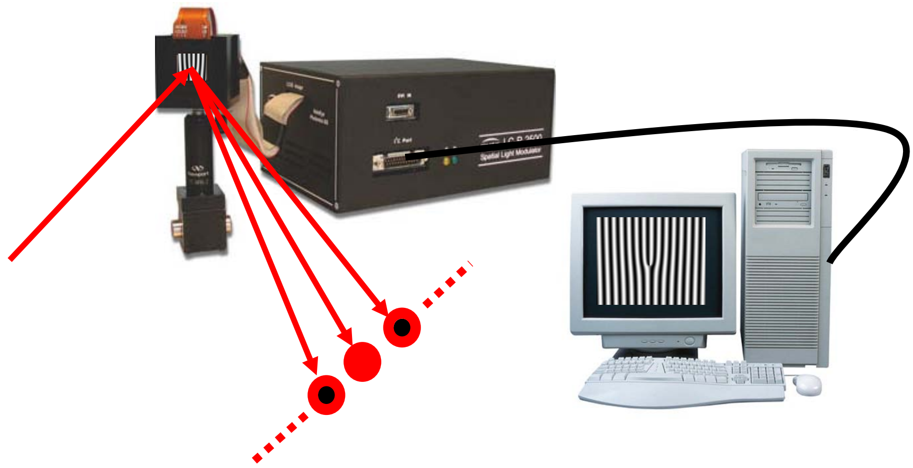

Figure 2.2: Diffracted orders from the SLM.

2.1.2 Spiral phase plate

The spiral phase plate (SPP) or vortex lens is also a type of mode converter that can generate optical vortices from laser beam by introducing a spiral phase [59]. SPP is a transparent disc whose thickness varies circumferentially but is uniform radially. These are constructed from a piece of transparent dielectric material. When a light beam passes through such plates then it suffers different path delays around the center of the disc as shown in Fig. 2.3. Light beams passing through the thicker part suffer longer optical path and hence greater phase shift. On the whole, due to spiraling thickness it generates spiral phase distribution of the optical vortex. The SPP is made for a particular wavelength of light.

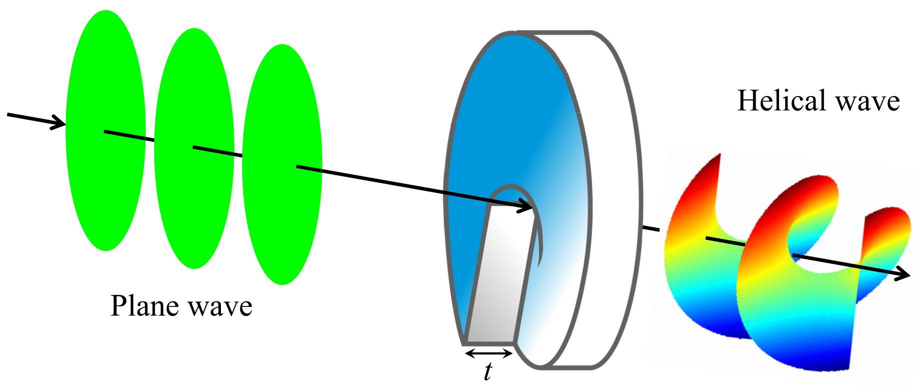

Figure 2.3: Generation of optical vortex using spiral phase plate. The thickness t is adjusted to generate order 2 vortex for the wavelength of laser used.

2.1.3 Generation of optical vortices using spatial light modulator (SLM)

In Fig. 2.4, we have shown a simple setup for the generation of optical vortices through a CGH with sinusoidal function. Gaussian beam from an intensity stabilized He-Ne laser (Spectra-Physics, 117A) is sent towards a beam splitter (BS). The transmitted beam from BS goes towards the SLM (Holoeye, LC-R 2500). The positions of the BS and the SLM are aligned in such a way that the transmitted beam from the BS falls normal to the SLM. Vortices of higher orders are produced in the first diffraction order by introducing different fork patterns onto the SLM via a computer (PC1). An aperture A is used to select the required first diffraction order produced from the SLM. It is then passed through a neutral density filter (NDF) to decrease the intensity of the vortex so that it does not saturate the CCD camera.

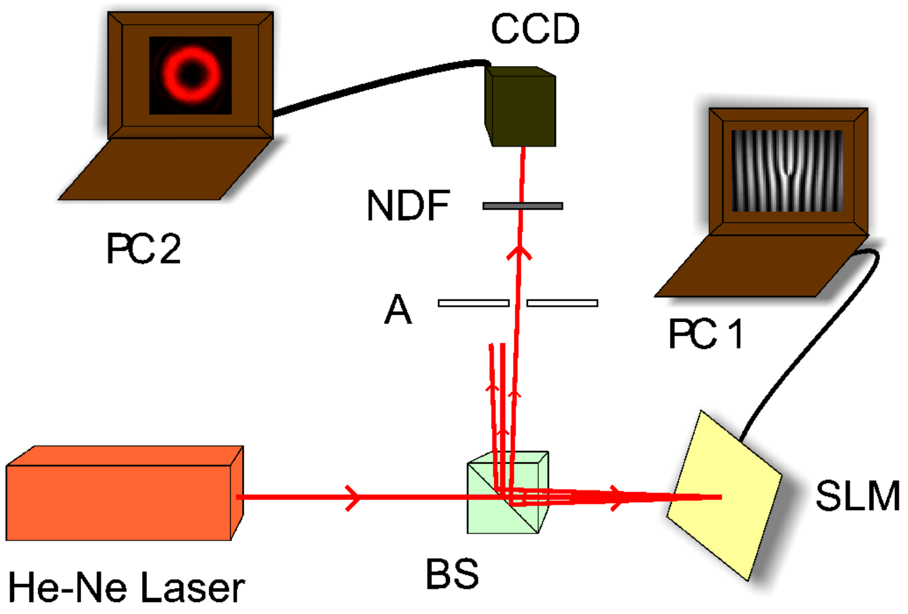

Figure 2.4: Experimental set-up for generating optical vortices and to find their order.

In Fig. 2.5, we show the intensity distribution of the optical vortex obtained from Eq. 2.9 and from experiment i.e. CCD camera. We would like to make it clear that the aperture A is being used just to select a particular diffracted order from the SLM, not to diffract the vortex. We take care that the selection does not introduce any diffraction ring to the vortex, which can be seen from the experimental intensity profiles of the vortices in Fig. 2.5.

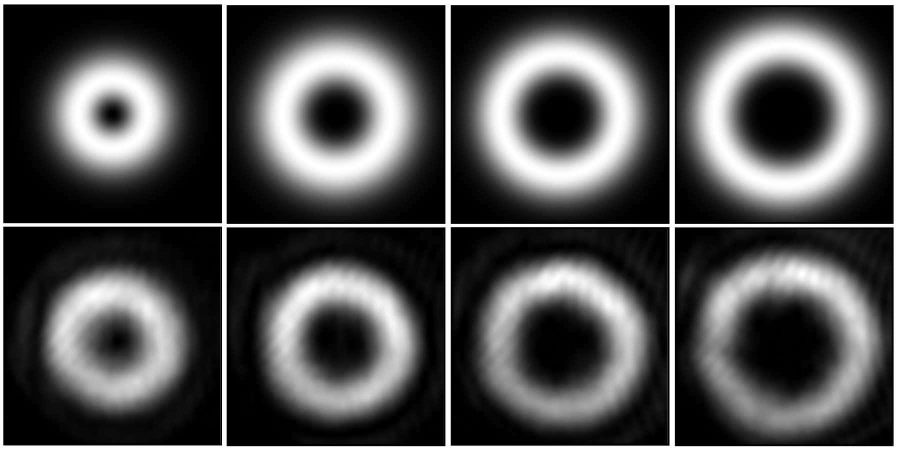

Figure 2.5: Intensity distribution of optical vortices of orders $m = 1$ to 4 (from left to right): theoretical (top) and experimental (bottom).

2.2 Determination of the order of vortex through intensity record

Detection and determination of the charge of optical vortices is one of the basic requirements in singular optics. Most of the techniques to determine the order of vortices are based on interferometry [65, 66, 67, 68]. The interferometry has been further extended to find the spatial coherence function which also provides information about the order of vortex [69]. All these methods require a good number of optical elements and their fine alignment. Aberrations in optical elements such as scratch and dig, dust particles on these elements and their misalignments disturb the characteristic interference pattern of the vortex. Therefore, efforts have been made to find the order of the vortex using techniques other than the interferometry [70, 71, 72, 73, 74].

In this section, we show that the order of a vortex can be obtained from the record of its intensity distribution itself. We know that when the order of the vortex increases, the size of the dark core at the center increases [75]. Moreover, the size of the dark core may vary depending on the resolution of the hologram used in the SLM [76]. Therefore, just by measuring the size of the dark core, it is difficult to discriminate the orders experimentally.

We provide a method to find the order of vortex by taking the Fourier transform (FT) of the recorded intensity of vortex and using the orthogonality of Laguerre polynomials.

2.2.1 Theoretical analysis

The field of a vortex of order m can be written as

$$E_m(x,y) = (x+iy)^m \exp\left(-\frac{x^2+y^2}{\sigma^2}\right), \tag{2.8}$$

where $\sigma = 1.69$ mm is the radius of the first diffraction order Gaussian beam at the CCD (see Fig. 2.4). The beam was generated by placing a grating without fork pattern at the SLM. The intensity of the vortex is given by

$$I_m(x,y) = \left(x^2+y^2\right)^m \exp\left(-2\frac{x^2+y^2}{\sigma^2}\right). \tag{2.9}$$

The FT of $I_m(x,y)$ has the expression

$$\mathcal{F}_m(\omega_1,\omega_2) = \int\limits_{-\infty}^{\infty}\int\limits_{-\infty}^{\infty} \left(x^2+y^2\right)^m \times \exp\left(-2\frac{x^2+y^2}{\sigma^2} - i(\omega_1 x + \omega_2 y)\right)\, dx\, dy, \tag{2.10}$$

where ω_1 and ω_2 are spatial frequencies. Expanding $(x^2+y^2)^m$ in a binomial series, Eq. 2.10 can be written as

$$\mathcal{F}_m(\omega_1,\omega_2) = \sum_{n=0}^{m} \binom{m}{n} \mathcal{I}_n(\omega_1)\mathcal{I}_{m-n}(\omega_2), \tag{2.11}$$

where

$$\mathcal{I}_n(\omega_1) = \int\limits_{-\infty}^{\infty} x^{2n} \exp(-2x^2/\sigma^2 - i\omega_1 x) dx. \tag{2.12}$$

Using the formula [77]

$$\int\limits_{0}^{\infty} x^{2n} \exp(-\beta^2 x^2) \cos ax\, dx = (-1)^n \frac{\sqrt{\pi}}{(2\beta)^{2n+1}} \exp\left(-\frac{a^2}{4\beta^2}\right) H_{2n}\left(\frac{a}{2\beta}\right) \tag{2.13}$$

and

$$H_{2n}(x) = (-1)^n 2^{2n} n! L_n^{-1/2}(x^2), \tag{2.14}$$

we get

$$\mathcal{I}_n(\omega_1) = \sqrt{\pi}\frac{\sigma^{2n+1}}{2^{n+1/2}} n! \exp\left(-\frac{\omega_1^2\sigma^2}{8}\right) L_n^{-1/2}\left(\frac{\omega_1^2\sigma^2}{8}\right), \tag{2.15}$$

and similarly for $\mathcal{I}_{m-n}(\omega_2)$. Substituting in Eq. 2.11, and performing the summation over n by means of the formula [77]

$$\sum_{n=0}^{m} L_n^{\alpha}(x) L_{m-n}^{\beta}(y) = L_m^{\alpha+\beta+1}(x+y), \tag{2.16}$$

we get

$$\mathcal{F}_m(\omega_1, \omega_2) = \frac{\pi\sigma^{2m+2}}{2^{m+1}} m! \exp(-\zeta) L_m(\zeta), \tag{2.17}$$

where $\zeta = (\omega_1^2 + \omega_2^2)\sigma^2/8$. In Eqs. 2.13 to 2.17, we have used the standard notations $H_n(x)$, $L_n(x)$ and $L_n^{\alpha}(x)$ to denote Hermite, Laguerre and generalized Laguerre polynomials respectively. By using the following orthogonality property of Laguerre polynomials

$$\int_0^{\infty} \exp(-\zeta) L_m(\zeta) L_n(\zeta)\, d\zeta = \delta_{m,n}, \tag{2.18}$$

one finds that the integral

$$C_{mn} = \int_0^{\infty} \mathcal{F}_m(\zeta) L_n(\zeta)\, d\zeta \tag{2.19}$$

will give a peak value for $m = n$. We have evaluated C_{mn} numerically by using the FT of the measured intensity profiles. We expect that this method is sensitive enough to detect any order of the vortex.

Before proceeding to our main result, it is important to realize that the FT of the vortex intensity can, in principle, determine the order of the vortex as the number of zeros of $L_m(\zeta)$ in Eq. 2.17 equals the order of the vortex. This is most clearly seen in the contour plot of the following quantity:

$$\mathcal{G}_m(\omega_1, \omega_2) = \log[1 + |\mathcal{F}_m(\omega_1, \omega_2)|]. \tag{2.20}$$

The zeros will appear as dark rings and thus the order of the vortex will be equal to the number of dark rings in the contour plot of $\mathcal{G}_m(\omega_1, \omega_2)$. The rationale behind plotting $\mathcal{G}_m$ instead of $\mathcal{F}_m$ was to identify the zeros more clearly.

2.2.2 Results and discussion

The fast-Fourier transform (FFT) of the measured intensity distributions is carried out numerically using Matlab. These images are processed in Matlab to reduce the noise and adjust the brightness and contrast. In Fig. 2.6, we show the contour plots of $\mathcal{G}_m(\omega_1, \omega_2)$ for vortices of different orders. The corresponding theoretical results are obtained by using Eqs. 2.17 and 2.20. It is clearly seen that the number of dark rings in each plot equals the order of the corresponding vortex and the experimental results are in excellent agreement with the theoretical predictions.

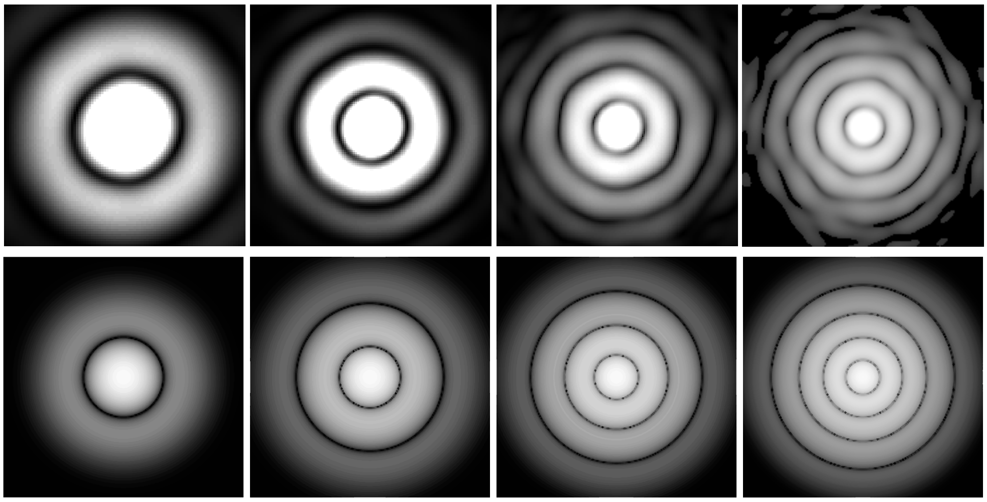

Figure 2.6: Distribution of $\mathcal{G}_m(\omega_1, \omega_2)$ computed from the intensity distributions of Fig. 2.5: experimental (top) and theoretical (bottom).

We mention parenthetically that for lower order vortices, a contour plot of $\mathcal{G}_m(\omega_1, \omega_2)$ will suffice to determine the order of the vortex. However, it will become difficult to see the rings beyond a certain order because of the dampening effect of the exponential factor in Eq. 2.17. *This is why our chosen method is based on the orthogonality property of Laguerre polynomials rather than relying upon a contour plot of $\mathcal{F}_m$ or $\mathcal{G}_m$.*

Using orthogonal relations of Laguerre polynomials, one can detect any order of the vortex. The results are shown in Fig. 2.7. It shows that for an optical vortex of order m, the normalized integral (Eq. 2.18) has maximum value when $m = n$.

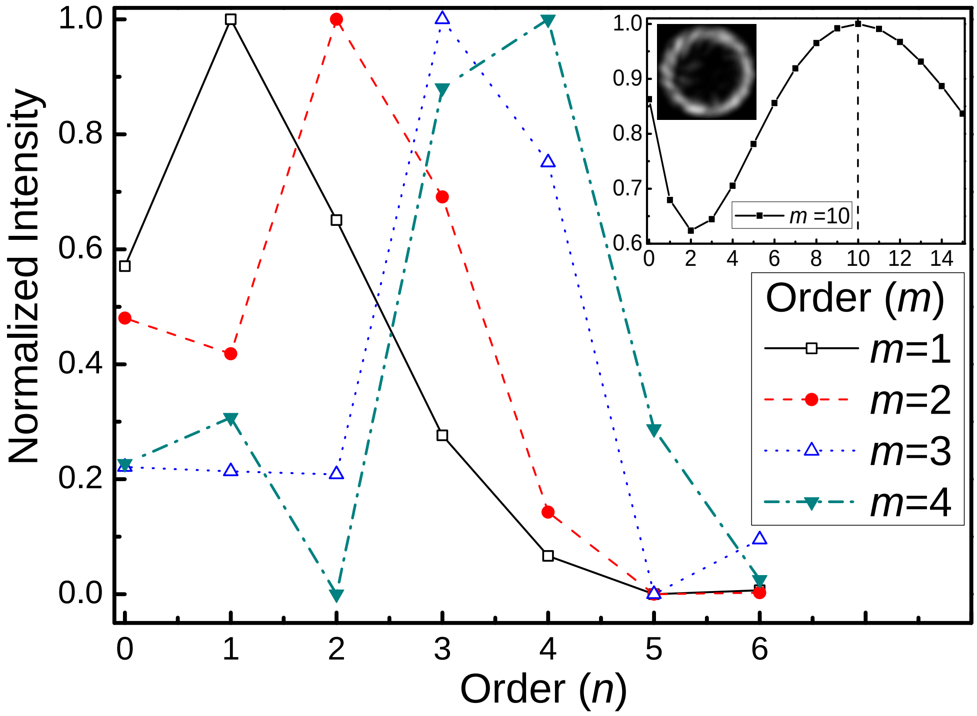

Figure 2.7: Normalized orthogonal integrals C_{mn} for optical vortices of orders $m = 1$ to 4. Inset shows C_{mn} and the intensity record of vortex for $m = 10$.

The sensitivity of this method can be easily established in the present context. For example, note that the outermost dark ring for 4th order vortex is not so distinct in Fig. 2.6 and thus it is not clear whether the vortex is of order 3 or 4. The orthogonality integral, in contrast, shows a clear peak for order m=4. In fact, our method applies even for a vortex of order $m = 10$, as shown in the inset of Fig. 2.7.

We would like to point out that unlike other methods where one need to find the FT of the field, in our case, it is the FT of the intensity of an un-diffracted vortex. This can be seen in our analytical treatment as well. Furthermore, our method does not use any annular aperture for diffraction. Therefore, the maximal topological charge that can be measured is not limited by the width of the annular aperture. As a demonstration, we have successfully applied our method for a vortex of order as high as $m = 10$. Moreover, for a given vortex, the only optical element one really requires is a neutral density filter (NDF) to reduce the intensity of the vortex to avoid saturation of the CCD. Thus, we have the least optics and the least aberrations.

2.2.3 Conclusion

In this work, we have outlined a simple technique to determine the order of a vortex based on the FT of its intensity profile and the orthogonality of the Laguerre polynomials. Since the phase information is lost in the intensity record of a vortex, our method cannot, however, determine the sign of its charge. At present, the method works for on-axis, isotropic vortices embedded in a Gaussian host. These limitations notwithstanding, the strong point of this technique is its simplicity and novelty. Since the experimentally recorded vortices do not have ideal Gaussian hosts, one experiences noise in the experimentally determined $\mathcal{G}_m(\omega_1, \omega_2)$ (see top row of Fig. 2.6) and C_{mn} in Fig. 2.7 does not reduce to zero for $m \neq n$. However, it still shows peaks for $m = n$ and is thus effective in determining the order of the vortex. Moreover, our method is fast. It takes just a fraction of second (0.85 seconds on Pentium IV, 3.4 GHz with 1.2 GB RAM) to calculate $\mathcal{G}_m(\omega_1, \omega_2)$ and a similar time in finding the C_{mn}. A Graphical User Interface (GUI) can be created using standard FFT routine for automating the process. This will help to get the order of vortex in real time. In conclusion, we have shown how complementary space can be used to provide us with the order of the vortex [78, 79].

Chapter 3

Spatial distribution of SPDC photons

The photon pairs generated through SPDC are entangled in the spatial degrees of freedom i.e. position-momentum entanglement [80] as well as entanglement in orbital angular momentum (OAM) [12]. The OAM entanglement can be described by a multi-dimensional Hilbert space [14, 81, 82], compared to the case of polarization entanglement which is limited to two dimensions only [83]. The produced photon pairs have been found to be entangled in time-bin also [84].

For any application of entangled photons generated through the SPDC, it is important to know the spatial distribution of these photons. For the Gaussian pump beam, the spatial distribution of SPDC photons has already been reported [27, 85, 86, 87]. However, for photons generated by pumping with higher order vortices, it has not been reported so far, although the phase-matching condition for an optical vortex pump beam has been studied theoretically by Pittman et.al. [88].

With the availability of low noise and high quantum-efficiency electron - multiplying CCD (EMCCD) cameras, the experiments with low photon level imaging has become possible [89]. To observe the shape of the SPDC ring formed by the Gaussian as well as optical vortex beams, we have carried out experiments using EMCCD. The observed experimental results are supported by our numerical results.

3.1 Theory

To numerically simulate the photon pair distribution in SPDC due to optical vortex beams, we start with the intensity distribution of an optical vortex of order l that is written as

$$I_l(x,y) = I_0(x^2+y^2)^{|l|} \exp\left(-\frac{x^2+y^2}{\sigma^2}\right), \tag{3.1}$$

where σ is the beam radius of host beam, I_0 is the maximum intensity in the bright ring. Clearly, Eq. 3.1 shows that the Gaussian beam can be considered as a special case of optical vortex with $l = 0$.

The nonlinear effects in crystals have been exploited in a number of applications such as frequency doubling, optical parametric oscillation and the SPDC [18]. When Beta-Barium Borate (BBO) is pumped by an intense laser, a *pump* photon (frequency ω_p and wave-vector $\mathbf{K}_p$) splits into a photon pair namely *signal* and *idler*. The energy and momentum conservation provide us with

$$\hbar\omega_p = \hbar\omega_s + \hbar\omega_i, \tag{3.2}$$

$$\mathbf{K_p} = \mathbf{K_s} + \mathbf{K_i}, \tag{3.3}$$

where suffices s and i denote signal and idler photons respectively. The phase matching is determined by the frequency of pump laser beam, and the orientation of crystal optic axis with respect to the pump. Equation 3.2 can be simplified as

$$\frac{1}{\lambda_p} = \frac{1}{\lambda_s} + \frac{1}{\lambda_i}, \tag{3.4}$$

where λ_p, λ_s and λ_i denote wavelengths of pump, signal and idler photons respectively. We have considered type-I non-linear BBO crystal which gives e $\rightarrow$ o + o type (e: extraordinary, o: ordinary) interaction. Hence, Eq. 3.3 can be written in terms of the momentum components as

$$\frac{2\pi n_e(\lambda_p,\Theta)}{\lambda_p} = \frac{2\pi n_o(\lambda_s)}{\lambda_s}\cos(\phi_s) + \frac{2\pi n_o(\lambda_i)}{\lambda_i}\cos(\phi_i) \tag{3.5}$$

$$\frac{2\pi n_o(\lambda_s)}{\lambda_s}\sin(\phi_s) = \frac{2\pi n_o(\lambda_i)}{\lambda_i}\sin(\phi_i) \tag{3.6}$$

where ϕ_s is the angle between $\mathbf{K_p}$ and $\mathbf{K_s}$, ϕ_i is the angle between $\mathbf{K_p}$ and $\mathbf{K_i}$ and Θ is the direction of optic axis with respect to $\mathbf{K_p}$ as shown in Fig 3.1. $n_e(\lambda_p,\Theta)$

and $n_o(\lambda_{s,i})$ are the extraordinary and ordinary refractive indices for respective wavelengths. These refractive indices are obtained from the Sellmeier equations [18] and for the BBO crystals used in the experiment can be written as

$$n_o(\lambda) = \sqrt{2.7359 + \frac{0.01878}{\lambda^2 - 0.01822} - 0.01354\lambda^2} \tag{3.7}$$

$$n_e(\lambda) = \sqrt{2.3753 + \frac{0.01224}{\lambda^2 - 0.01667} - 0.01516\lambda^2} \tag{3.8}$$

$$n_e(\lambda, \Theta) = n_o(\lambda)\sqrt{\frac{1 + \tan(\Theta)^2}{1 + \left[\frac{n_o(\lambda)}{n_e(\lambda)} \times \tan(\Theta)\right]^2}} \tag{3.9}$$

where λ is in μm.

In Fig. 3.1, we have given a sketch of the SPDC photon pair generation in non-collinear type-I SPDC process. **C** denotes the crystal optic axis. The angular separation between $\mathbf{K_p}$ and $\mathbf{K_s}$ is due to energy and phase-matching conditions (Eq. 3.5 and 3.6) required for the SPDC process. We have also shown generation of a pair of signal and idler photons and formation of the ring centered around $\mathbf{K_p}$. In the present case, we have assumed that the pump beam has circular symmetric i.e. same horizontal and vertical widths.

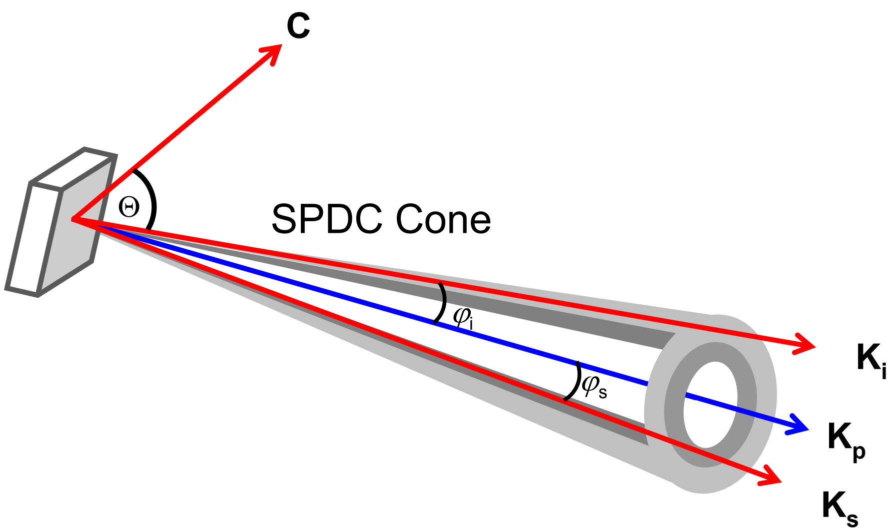

Figure 3.1: Sketch diagram for the SPDC ring formation after passing the pump beam through the BBO crystal. Light and dark gray levels represent generation of idler and signal photon SPDC rings respectively.

We have used a negative-uniaxial BBO crystal with non-linear coefficient d_{eff}

= 2.00 pm/V, thickness 5 mm and optic axis $\Theta = 29.7°$. The pump beam with wavelength $\lambda_p = 405$ nm is incident normal to the crystal. We plan to study the degenerate or near-degenerate case in which the signal and idler photons have almost same wavelength $\lambda_{s,i} = 810 \pm 5$ nm. The wavelengths for down-converted photons are chosen from the interference filters (IF) used in the experiment. With these experimental parameters, Eqs. 3.5 and 3.6 have been solved to determine ϕ_s and ϕ_i by Runge-Kutta (RK) method for a particular value of λ_s and λ_i that satisfies Eq. 3.4.

Numerical simulations have been performed by first considering a particular values λ_s and λ_i. Angles ϕ_s and ϕ_i are evaluated using RK method for chosen λ_s, λ_i and experimental parameters. The signal and idler photons are generated in cones having half-opening angle ϕ_s and ϕ_i as represented in Fig. 3.1 and appear as two rings on the detector plane. The center of these rings are concentric with the pump beam. Now, consider a single point on the intensity distribution of pump falling on the crystal. The stream of single photons passing through the chosen point generates SPDC rings whose radius depends on the distance between crystal and EMCCD. The intensity of the ring is proportional to the intensity at the selected point. The rings corresponding to signal and idler photons are then added to obtain the SPDC ring corresponding to pump photons. In the similar way, rings for all other points of pump intensity distribution are obtained and added. The obtained spatial distribution depends on the shape and size of the pump beam. This will provide the SPDC ring for λ_s and λ_i. The contributions due to whole wave-length range (810±5 nm)allowed by the IF has been considered to obtain the resultant spatial distribution of SPDC ring.

3.2 Experimental setup

The experimental set-up to study the SPDC photon pair distribution generated by the Gaussian as well as the optical vortex pump beam is shown in Fig. 3.2. The ellipticity of the diode laser (RGBLase 405 nm, 50 mW) has been removed by using a combination of lenses. The collimated beam is then sent to a spatial light modulator (SLM) (Hamamatsu LCOS SLM X-10468-05), which is interfaced with computer (PC1) with slightly tilted mirror for not losing the power. Blazed holograms have been used to generate OV with higher power in the first diffraction order [90]. The first diffracted order is selected with an aperture A3. Polarizer (P) and half-wave plate (HWP) are used to select and rotate the polarization of pump beam respectively. BBO crystal ($6\times6\times5$ mm^3) with optic axis at 29.7° is used for the spontaneous parametric down-conversion. As the size of OV beams of higher order becomes bigger than the size of the crystal, we have used a lens L1 (f=15 cm) to loosely focus the vortex beam on the crystal [91]. The BBO crystal is mounted on a rotation stage, so that phase-matching angle can be achieved by rotating the crystal towards its optic axis. After achieving phase-matching, the crystal remains unaltered for all the observations.

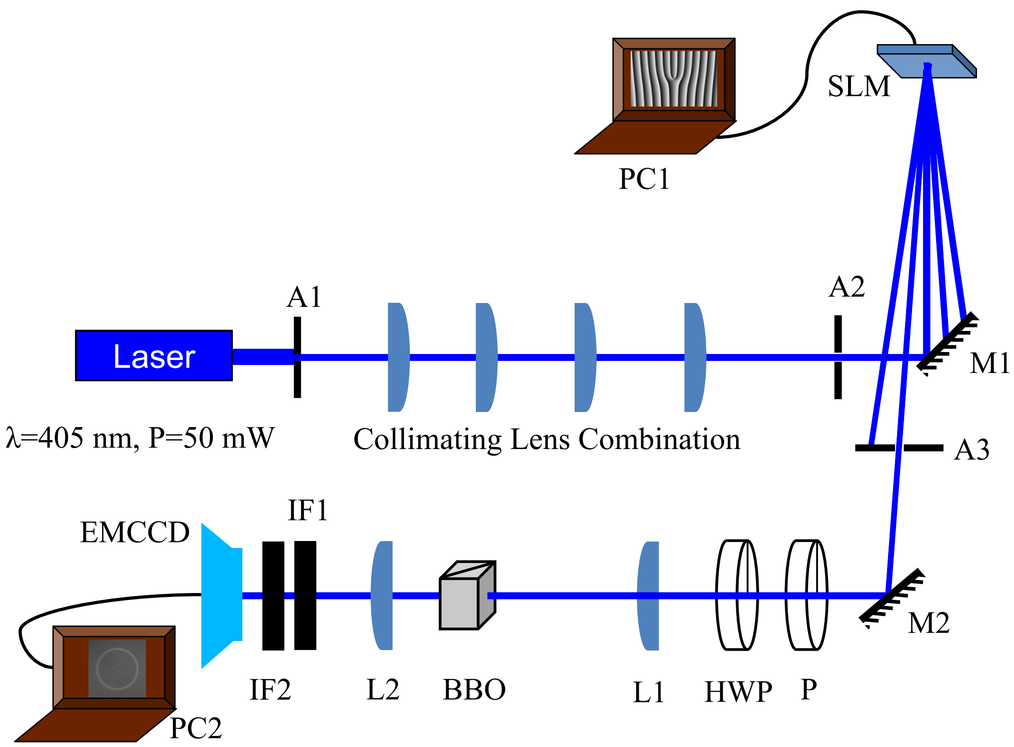

Figure 3.2: Experimental setup for the study of SPDC photon pair distribution with an optical vortex as pump beam.

When phase-matched, the output cone makes half angle of $\sim 4°$ with pump direction $\mathbf{K_p}$. The BBO crystal's optic axis has been chosen in such a way that it can down-convert only vertically polarized light. Therefore, when angle of the HWP is 0° (45°), then we will get (not get) down-converted photons. Image of the down-converted ring is recorded by Andor iXon$_3$ EMCCD camera using an imaging lens of focal length 5 cm. We have used the EMCCD in background correction mode. In this mode, background is obtained when $\lambda/2$ plate is at 45° and signal is obtained when $\lambda/2$ plate is at 0°. The central bright spot in experimental observations show the unfiltered pump beam. This could not be subtracted completely while subtracting the background due to slight shift in its position during the rotation of HWP from 45° to 0°. The interference filters IF1 and IF2 pass only the down-converted photons of wave-length 810±5 nm and block the pump photons of wave-length 405 nm. Two interference filters have been used to reduce the pump photons as much as possible that increase the signal to noise ratio in the SPDC ring.

The power of 405 nm laser falling on the BBO crystal was 2 mW. EMCCD was operated at -80°C. Further, we have taken images by accumulating 50 frames with exposure time of 1 s. We have used the complete 512×512 pixels of the camera. The readout rate was set at 1 MHz 16-bit. Since the observed SPDC rings are sufficiently intense, we have not enabled the electron-multiplication gain.

The size of pump beam has been measured by imaging the beam at the position of crystal with Point-Grey (FL2-20S4C) CCD camera. The images obtained from the CCD camera are read in Matlab for further processing. The 2-D curve fitting is used to obtain the best-fit intensity distribution obtained by Eq. 3.1 that provides us with beam-width of the pump (σ_{pump}). For our numerical calculations, we have used the best-fit value of σ_{pump} obtained experimentally.

3.3 Results and discussion

The objective of the experimental work is to characterize the spatial distribution of degenerate SPDC photon pairs produced by higher order vortices and verify the results obtained with numerical calculations. Before pumping the nonlinear crystal with high order vortices, we study the distribution of SPDC photons generated by the Gaussian beam of different widths.

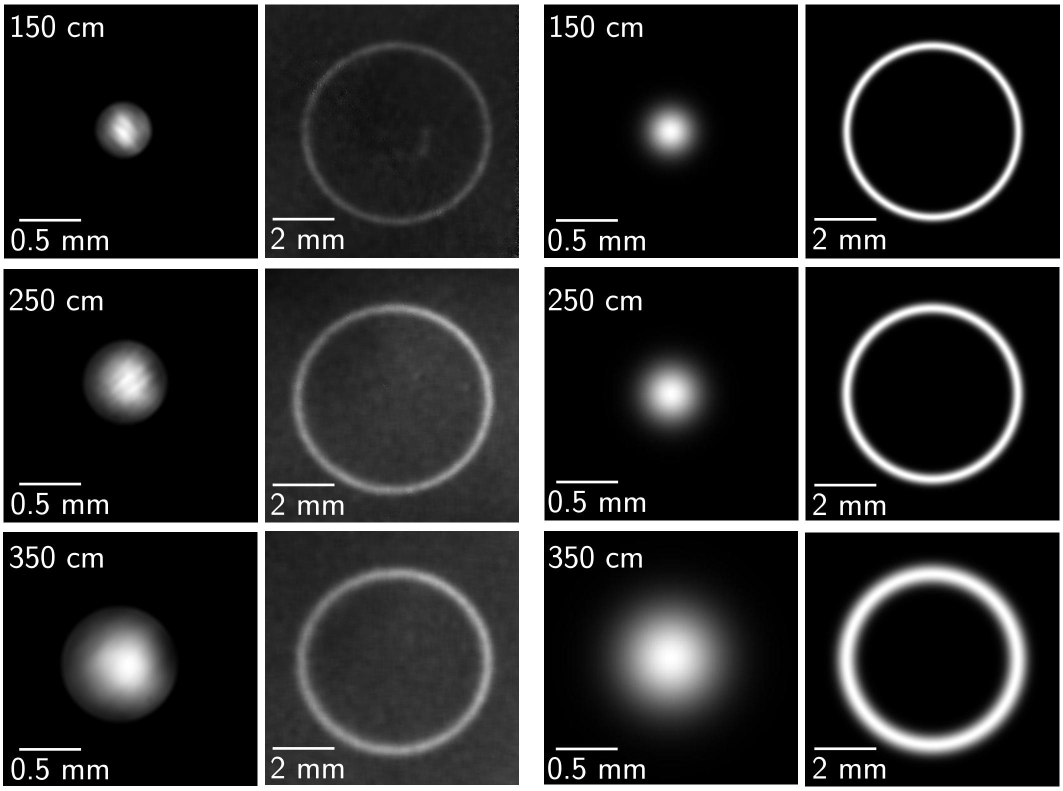

Figure 3.3: Experimental (left) and Numerical (right) are Gaussian pump and their corresponding SPDC rings. The three Gaussian beams have been taken by placing the crystal at distances 150 cm, 250 cm and 350 cm from the SLM.

To make a comparison of spatial distribution of down-converted photons due to the Gaussian and the vortex beams, the Gaussian beam is generated using the SLM by transferring the blazed grating hologram of topological charge 0 to the SLM. To vary the width of the Gaussian beam, we have used the beam at different propagation distances from the SLM (150 cm to 350 cm in the steps of 50 cms). As the size of beam is lower than the aperture size of the crystal at 350 cm from the SLM, lens (L1) was not used. The experimentally and numerically obtained SPDC rings are shown in Fig. 3.3. We observe an increase in thickness of the SPDC ring as the pump beam size increases.

To obtain a quantitative variation of SPDC ring, we use the line profile across the SPDC rings through their center. Numerically, we have observed that the SPDC ring fits with a Gaussian function. To calculate the width of SPDC ring

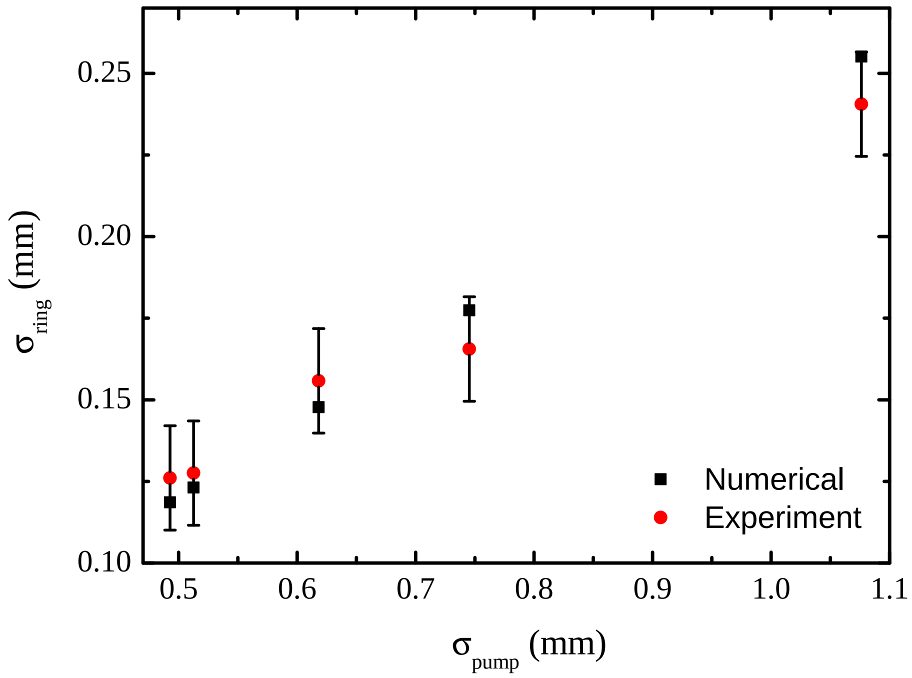

Figure 3.4: Variation of σ_{ring} with σ_{pump}. The curve shows the linear variation in thickness of the SPDC ring with the beam-width of Gaussian pump beam.

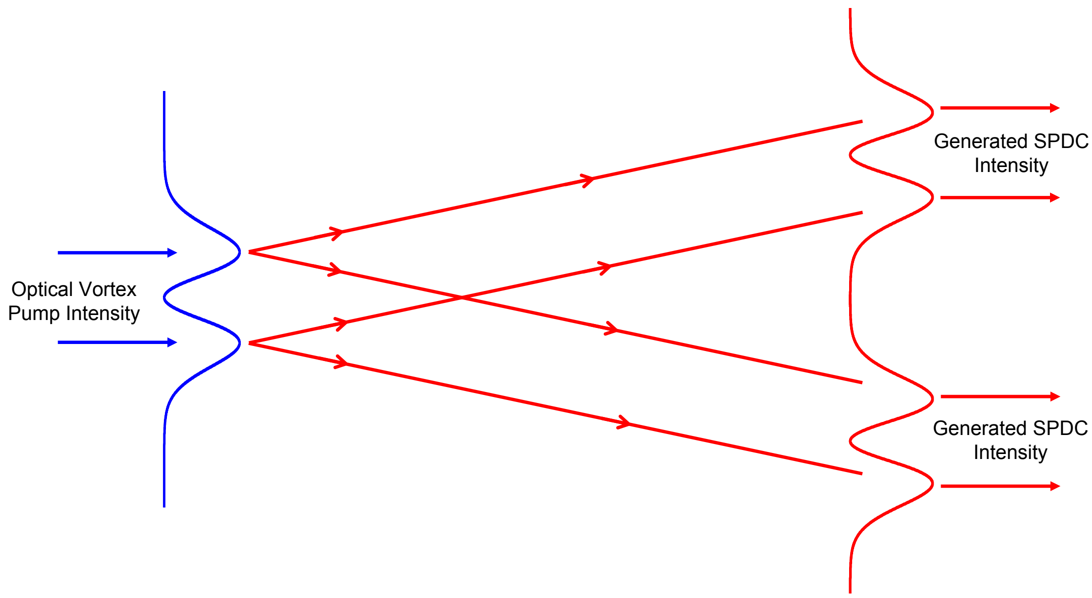

Figure 3.5: Schematic diagram for the generation of two rings when pumped with optical votex beams.

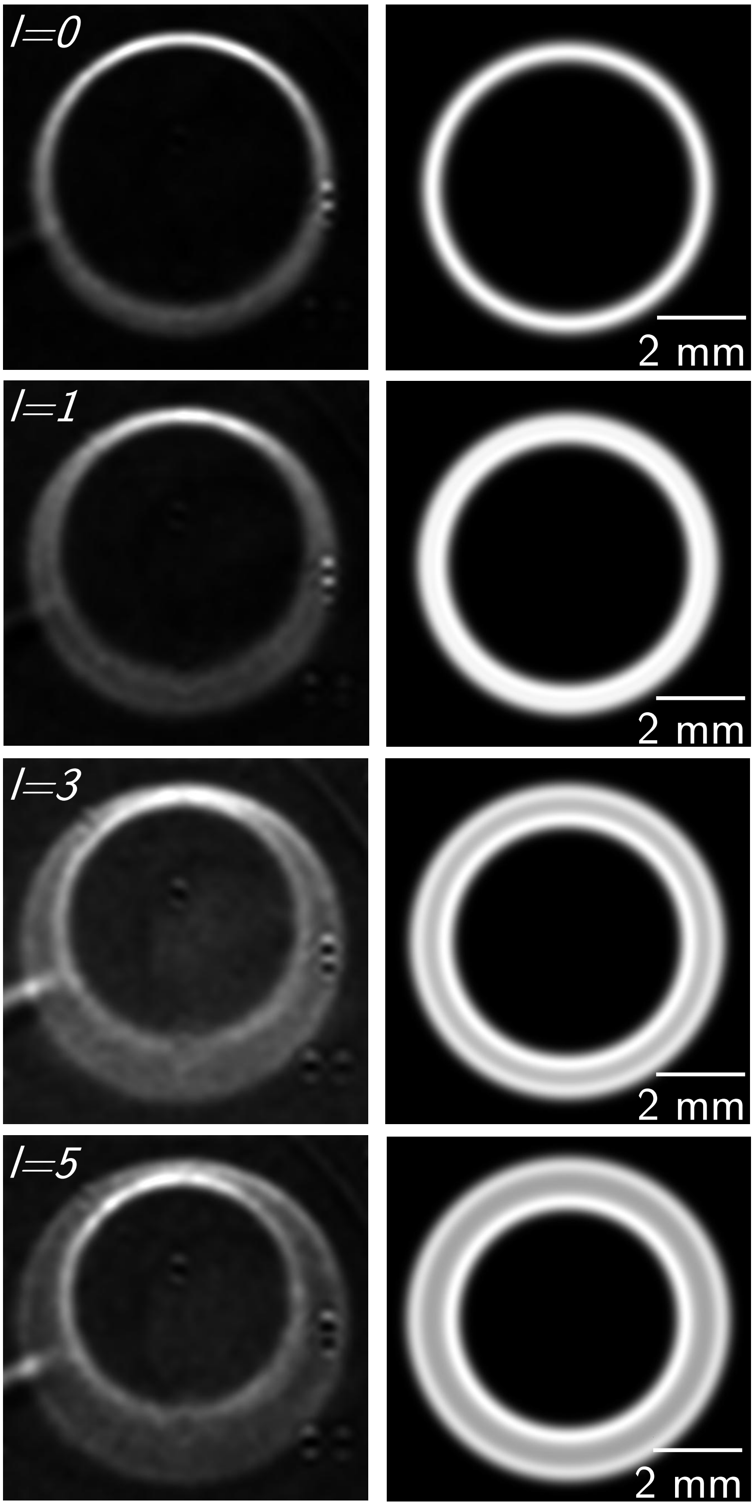

Figure 3.6: Experimental (left) and Numerical (right) SPDC rings due to an optical vortex pump beam for order 0, 1, 3 and 5. Spot in the center of experimental images correspond to the unfiltered pump beam.

(σ_{ring}), the profiles obtained are fitted with a Gaussian function as in Eq. 3.1 for l=0. The variation of thickness of the SPDC rings with the size of the pump beam is shown in Fig. 3.4. Numerical and experimental results are found to be in good agreement with each other. We find that our results are similar to the one obtained earlier [85].

Figure 3.5 shows the generation of two rings when the BBO crystal is pumped with OV. The blue and red lines show the intensity distribution of the pump and the SPDC photons. As the size of optical vortex goes beyond the aperture of BBO crystal, we have used lens (L1) to loosely focus it. It has been observed that the SPDC ring due to optical vortex forms two concentric bright rings with non-zero intensity in middle. The SPDC rings due to optical vortices are shown in Fig. 3.6. From these images, we can observe the increase in thickness of the SPDC ring along with two concentric rings.

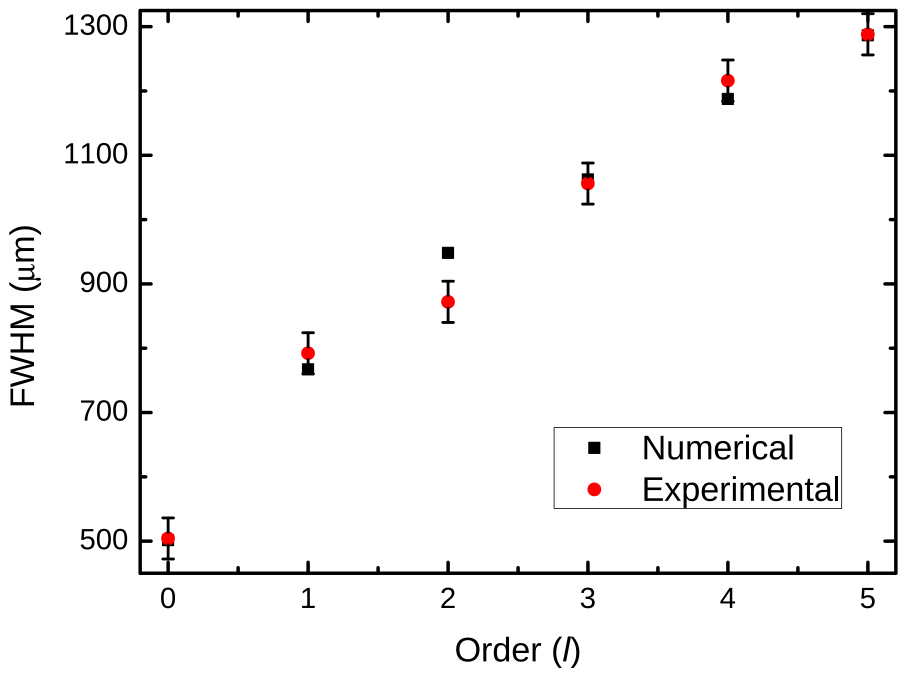

Figure 3.7: Variation of FWHM of SPDC ring for optical vortex pump beams with the order of optical vortices.

With the increase in topological charge of vortices, the full width at half maximum (FWHM) of the ring increases as shown in Fig. 3.7. The separation between the inner and the outer ring also increases with the increase in order. However, we can observe the asymmetry caused due to the crystal length. This asymmetry arises due to the longitudinal phase matching and depends on nonlinear crystal properties of the crystal, including crystal length [85]. This is one of the factors which affect the selection of entangled photons and consequently the total coincidence counts.

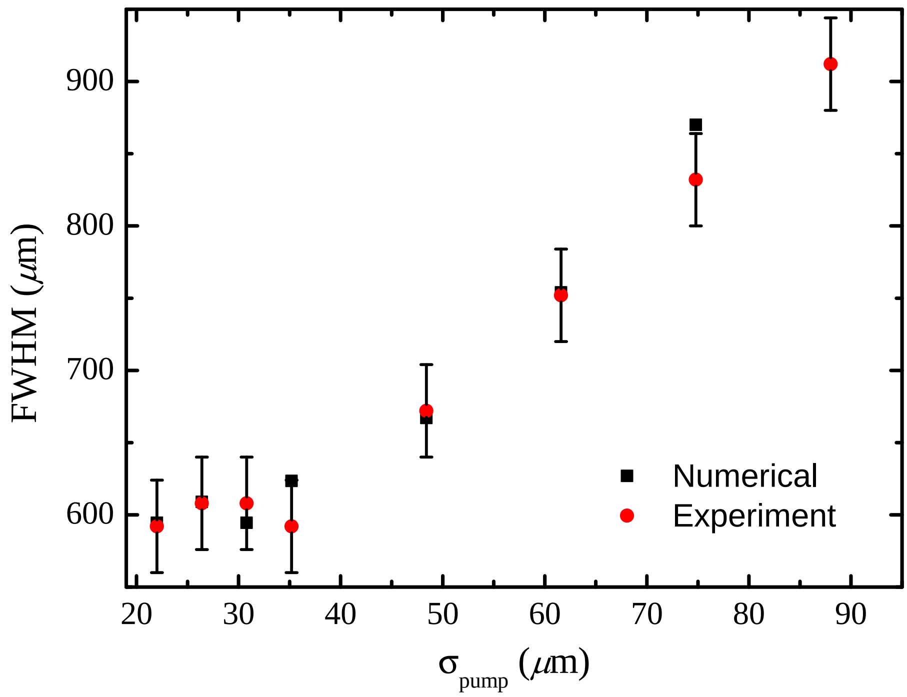

Figure 3.8: Variation of FWHM of SPDC ring for optical vortex pump beam of order l=2 with beam width of the host beam.

We have also observed that if σ_{pump} is lower than a particular value for the OV of topological charge l, then there will not be any change in FWHM. This variation has been studied by varying σ_{pump} and keeping the order l fixed. We have observed that the FWHM of the ring starts increasing only when σ_{pump} is more than a particular beam size, called critical beam size. The variation of FWHM of SPDC ring for order l=2 with σ_{pump} is shown in Fig. 3.8. In case of OV, the numerical and experimental results are in good agreement with each other.

The width of the SPDC ring is governed mainly by two parameters – pump beam size and crystal length. Both these parameters increase the width of the ring. In our experiment, same crystal of length 5 mm has been used throughout the study. The pump beam size was changed by changing the propagation distance from the SLM. The increase in the width of SPDC ring due to the crystal length cannot be avoided, as it is fixed. This was one of the reasons for the presence of critical pump-beam size below which the width of SPDC ring does not decrease. This holds true for Gaussian as well as Laguerre Gaussian beams.

3.4 Conclusion

The spatial distribution of entangled photons generated by pumping the nonlinear crystal with the light beam is of importance in the field of quantum information and quantum computation. We have observed a linear increase in thickness of the SPDC ring with beam radius of the Gaussian pump.

We have also observed the formation of two concentric SPDC rings if the crystal is pumped with optical vortex beams. One of the reasons for generation of two rings is the dark core of optical vortex i.e. unique intensity distribution of the vortex. The numerical and experimental widths of the SPDC ring are in good agreement with each other. The formation of two rings takes place when the pump beam size is more than the critical beam size. These observations would be useful in the experiments to maximize the coincidence counts. Physically, the broadened SPDC is a consequence of the greater spread of pump transverse wave-vectors, resulting in phase matching for a greater spread of signal and idler transverse wave-vectors.

Chapter 4

Violation of Bell's inequality for phase singular beams

Traditionally, entanglement has been regarded as an exclusive feature of quantum mechanics and provides a powerful resource for quantum information science especially in quantum computing, quantum cryptography, and quantum teleportation [92]. The quantum state of an entangled system cannot be factored out into the product of individual states. Bell's inequality measurement is one of the ways to measure the presence of entanglement in quantum entangled systems [93, 94]. The entanglement carries, in quantum context, a rich variety of implications such as nonlocality and Bell's inequality violation.

The term "classical" in "classical entanglement" indicates the non-quantum nature of classical electromagnetic field. Classical entanglement should not be confused with "entanglement present in classical optics" and hence cannot be used to reproduce non-classical correlations between measurements [95]. Rather, it can be considered as the presence of non-factorizable field of the light beam in two-conjugate variables, for example position and momentum. Thus, the main purpose of this study is to revisit the concept of the so-called "classical entanglement" for a beam of light.

In this study, we deal with bright beams of light like Gaussian and optical vortex beams. However, whether the beam is very intense or very weak, is a factor that does not have any effect on the amount of entanglement. In this study, the spatial coherence present in the beam plays a vital role. Study of the Wigner distribution function (WDF) has been found to be very useful since it can provide coherence information in terms of the joint position and momentum (phase-space) distribution for a particular optical field [96]. Using the WDF, one can study the continuous variable correlations present in classical beams. Recently, the famous Bell's inequality has been defined for classical sources using WDF and it has been shown theoretically that the optical vortex beams violate this inequality [97]. The calculation of inequality uses variable correlations existing between position and momentum of the vortex. Such quantum inspired inseparability has been termed as "classical entanglement" [98, 99].

In this chapter, we have demonstrated the experimental verification of "classical entanglement" using the WDF and two-point Bell's inequality for optical vortex beams obtained in ref. [97]. To verify the theoretical results, we produce different orders of vortex fields described by the LG modes using a spatial light modulator (SLM) [75]. The two-point correlation function has been found using the interference between vortices of the same order and is scanned using a shearing Sagnac interferometer (SSI) [100, 101]. Theory related to this study has been discussed in section 4.1, experimental details have been given in section 4.2. Results and discussion constitute in section 4.3 and finally we conclude in section 4.4.

4.1 Theoretical background

The WDF for optical vortex beams can be written as [96, 102]

$$W_{nm}(X, P_X; Y, P_Y) = \frac{(-1)^{n+m}}{\pi^2} L_n[4(Q_0 + Q_2)] \times L_m[4(Q_0 - Q_2)] \exp(-4Q_0), \tag{4.1}$$

where $\{X, P_X\}$ and $\{Y, P_Y\}$ are conjugate pairs of dimensionless quadratures and n is the azimuthal while m is the radial index of Laguerre Gaussian beam Eq. 1.1. Q_0 and Q_2 are

$$Q_0 = \frac{1}{4}\left[X^2 + P_X^2 + Y^2 + P_Y^2\right], \quad Q_2 = \frac{XP_Y - YP_X}{2}, \tag{4.2}$$

where the scaled variables X, P_X, Y and P_Y can be defined as

$$x(y) \rightarrow \frac{\sigma}{\sqrt{2}} X(Y), \quad p_x(p_y) \rightarrow \frac{\sqrt{2}\lambda}{\sigma} P_X(P_Y) \tag{4.3}$$

and follow $[\widehat{X}, \widehat{P}_X] = [\widehat{Y}, \widehat{P}_Y] = i$. σ is the beam waist of the Gaussian host beam.

WDF defined in Eq. 4.1 can be obtained by taking the Fourier transform (FT) of two-point correlation function (TPCF) that is defined as

$$\Phi(x, \epsilon_x; y, \epsilon_y) = \langle E(\epsilon_x + x/2, \epsilon_y + y/2) E^*(\epsilon_x - x/2, \epsilon_y - y/2) \rangle \,, \tag{4.4}$$

In fact in experiment, one measures TPCF only to determine the WDF.

4.1.1 Bell's inequality for continuous variable systems

For discrete entangled systems, the Bell-CHSH inequality can be written as [93, 103]

$$B = |S(a, b) + S(a, b') + S(a', b) - S(a', b')| < 2, \tag{4.5}$$

where (a, b), (a', b') are two analyzer settings and $S(a, b)$ is the joint probability corresponding to settings (a, b). The entanglement in quantum systems with continuous variables is characterized by probabilities. For continuous variable systems, WDF is expressed as an expectation value of a product of displaced parity operators. Banaszek and Wodkiewicz [104, 105] have argued that the WDF can be used to derive the analog of Bell's inequality in continuous variable systems.

Considering the transformation $\Pi(X, P_X; Y, P_Y) = \pi^2 W(X, P_X; Y, P_Y)$ in dimensionless quadratures, then the Bell-CHSH inequality B with chosen points $\{a,b\} \equiv \{X1, P_{X1}; Y1, P_{Y1}\}$ and $\{a',b'\} \equiv \{X2, P_{X2}; Y2, P_{Y2}\}$ can be written as

$$\begin{aligned} B \;=\; & \Pi_{nm}(X1, P_{X1}; Y1, P_{Y1}) + \Pi_{nm}(X1, P_{X1}; Y2, P_{Y2}) \\ & + \Pi_{nm}(X2, P_{X2}; Y1, P_{Y1}) \\ & - \Pi_{nm}(X2, P_{X2}; Y2, P_{Y2}) < 2. \end{aligned} \tag{4.6}$$

4.1.2 Bell's violation for first order vortex (n=1 and m=0)

From Eq. 4.1, the WDF of an optical vortex beam with topological charge 1 can be obtained as

$$W_{10}(X, P_X; Y, P_Y) = \exp\left(-X^2 - P_X^2 - Y^2 - P_Y^2\right) \frac{(P_X - Y)^2 + (P_Y + X)^2 - 1}{\pi^2}. \tag{4.7}$$

Choosing $X1 = 0, P_{X1} = 0, X2 = X, P_{X2} = 0, Y1 = 0, P_{Y1} = 0, Y2 = 0, P_{Y2} = P_Y$, the Bell-CHSH parameter can be can be written as

$$B = \Pi_{10}(0, 0; 0, 0) + \Pi_{10}(X, 0; 0, 0) + \Pi_{10}(0, 0; 0, P_Y) - \Pi_{10}(X, 0; 0, P_Y) \tag{4.8}$$

$$= e^{-P_Y^2}(P_Y^2 - 1) + e^{-X^2}(X^2 - 1) - e^{-P_Y^2 - X^2}[(P_Y + X)^2 - 1] - 1. \tag{4.9}$$

The maximum Bell's violation considering only two variables X and P_Y is $|B_{max}| \sim$ 2.17 which occurs at X ~0.45 and P_Y ~0.45. Considering all eight variables from Eq. 4.6, the maximum Bell's violation is $|B_{max}|$ ~2.24 at $X1 \sim -0.07$, P_{X1} ~0.05, $X2$ ~0.4, $P_{X2} \sim -0.26$, $Y1 \sim -0.05$, $P_{Y1} \sim -0.07$, $Y2$ ~0.26 and P_{Y2} ~0.4. The experimental verification for these results have been discussed in the following section.

4.2 Experimental setup

The experimental setup to find the two-point correlation function (TPCF) is shown in Fig. 4.1. Computer generated holography has been used to generate optical vortices [64]. A Gaussian laser beam from an intensity stabilized He-Ne laser (Spectra-Physics, 117A) is incident normally to the SLM (Holoeye, LC-R 2500) using the mirror M1 and the beam splitter BS1. The SLM is a liquid-crystal-based device that can modulate light and can be used as a dynamic diffractive optical element. Vortices of different orders are produced in the first diffracted order by introducing different fork patterns onto the SLM via a computer PC1. Apertures A1 and A2 are used to select an optical vortex of the desired order. A polarizer (P) is used to fix the polarization (here vertical) of the optical vortex. The vortex with the vertical polarization is coupled to the Shearing-Sagnac interferometer (SSI) that comprises the beam splitter BS2 and two mirrors, M2 and M3. A quarter-wave plate (QWP) and a half-wave plate (HWP) are kept in common path for the quadrature selection. A glass block mounted upon a rotation stage is also kept in the common path to introduce the shear in two transverse directions. This arrangement ensures that both the clockwise (cw) and the counter-clockwise (ccw) fields experience one reflection from and one transmission through the beam splitter. This removes the effect of deviations from 50% transmission and polarization-sensitivity of the beam splitters. The two counter-propagating beams are interfered and imaged using a Evolution VF cooled CCD camera that is connected to computer PC2.

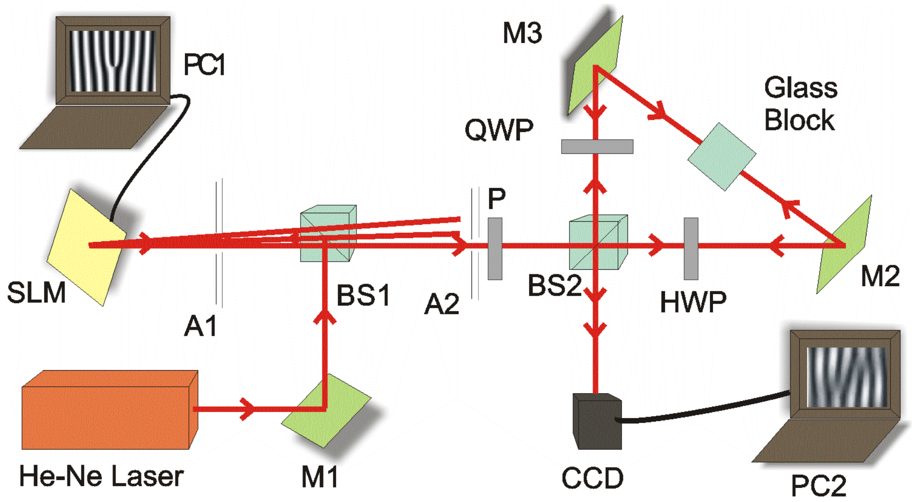

Figure 4.1: Experimental setup for determination of TPCF.

First, we have calibrated the shear in laser-beam produced by the glass block. For this, we put one polarizer inside the SSI. The clock-wise and counter clockwise propagation of beams were chosen by the rotation of the polarizer. We have put a normal grating on the SLM to propagate Gaussian beam inside the SSI. Then, we rotate the glass block such that there is no shear between the two beams. After this, we have provided some shear in the glass block which is mounted on a rotation stage with linear scale. The shear is varied in equal steps. The particular rotation in the glass block will provide us the shear in the beams propagating inside the SSI. We have recorded the intensity of two beams with CCD camera. These images were processed in MATLAB to determine the shear in between the two beams. The beam width w of the laser beam falling on the

CCD was determined using the 2D curve-fitting in MATLAB. The scaled shear was obtained using Eq. 4.3 corresponding to the linear scale on the rotation stage of glass block. We have achieved the required shears after calibrating the SSI. The amount of shear as a function of scale has been shown in Fig. 4.2.

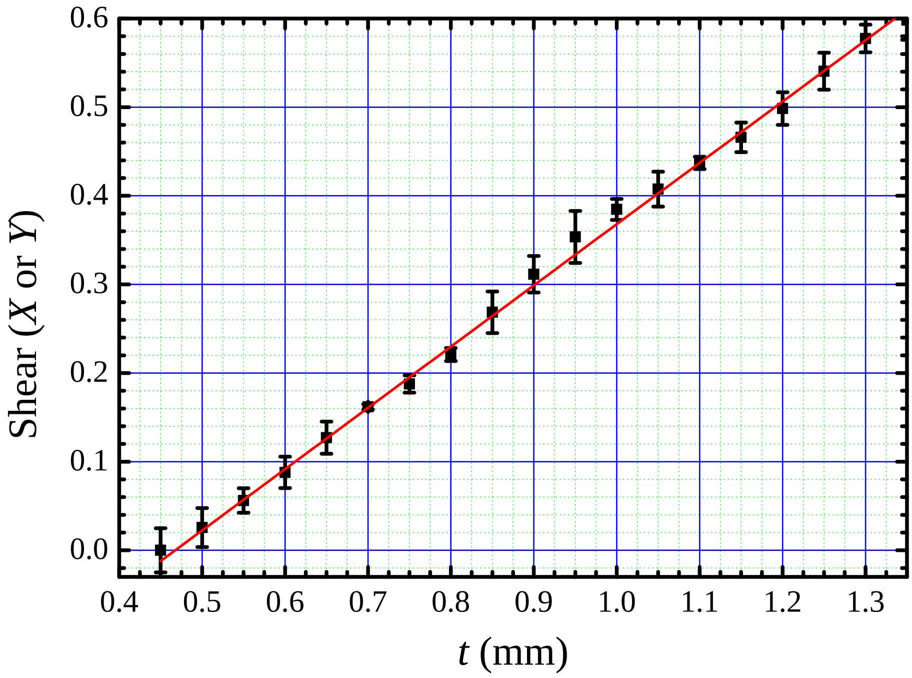

Figure 4.2: Calibration curve for dimensionless shear $(X,\ Y)$ in the SSI. The x-axis (t) denotes the position of linear scale in the mount on which the cube was mounted. The red line is the linear fit to our data.

4.3 Results and discussion

The main part of our experiment is to determine the TPCF [100, 69]. For various tilts of the glass block, we have recorded the interferograms by keeping the fast axes of the QWP and the HWP parallel to the incident beams' polarization direction. In this orientation, the wave plates have no effect on the polarization of the optical beam, and both the CW and CCW propagating fields travel equal optical path lengths inside the SSI. The recorded interferograms contain the information of $\mathrm{Re}[\Phi(X, \epsilon_x; Y, \epsilon_y)]$. Keeping the same lateral shear values, interferograms for $\mathrm{Im}[\Phi(X, \epsilon_x; Y, \epsilon_y)]$ is taken after rotating HWP by $\pi/4$ such that both the CW and CCW propagating fields rotate in polarization by 90°. Figure 4.3(a) shows the TPCF of a Gaussian beam, while 4.3(c) and 4.3(e) show for optical vortex of topological charge $n = 1$ at zero shear ($X = Y = 0$) and non-zero shear ($X = 0.1$, $Y = 0.1$) respectively. TPCF at non-zero shear (X, Y) was obtained by tilting the glass cube to corresponding positions along x and y axes suggested by Fig. 4.2.

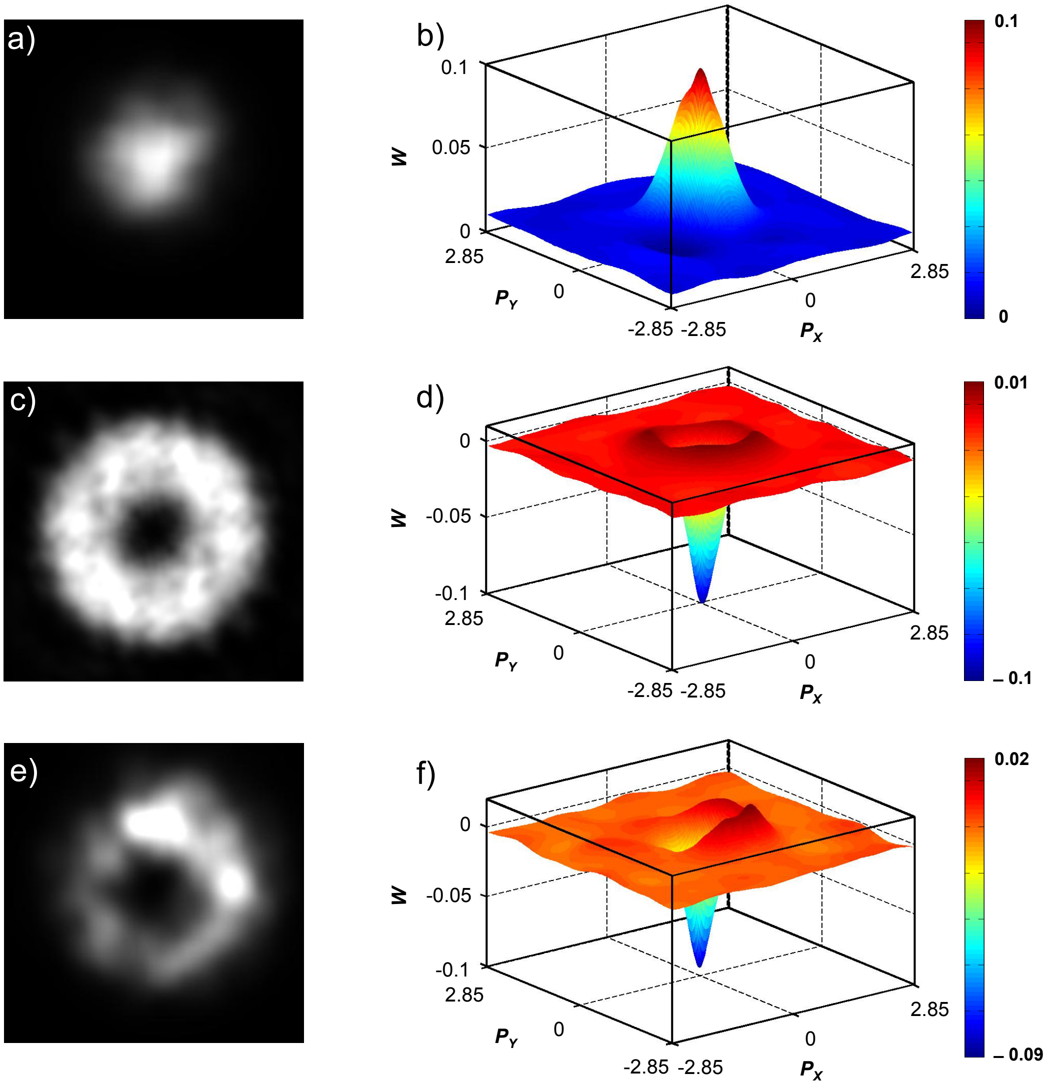

Figure 4.3: Experimentally obtained absolute value of TPCF (left column) and corresponding Wigner distribution function (right column) for Gaussian beam (first row) and optical vortex of topological charge $n = 1$ at zero shear $X = Y = 0$ (middle row) and non-zero shear $X = 0.1$ and $Y = 0.1$ (bottom row).

These TPCFs are obtained at zero shears (X=0, Y=0). To obtain the TPCF at different shears (X, Y), the glass cube is rotated to corresponding positions along x and y axes suggested by Fig. 4.2.

To obtain the WDF, we have taken the Fourier transform of the experimentally obtained TPCF [96]. Figure 4.3(b) shows the WDF of Gaussian beam while 4.3(d) and 4.3(f) show WDFs for optical vortex with topological charge $n = 1$ at zero shear ($X = Y = 0$) and non-zero shear ($X = 0.1$, $Y = 0.1$) respectively. This shows that our results are consistent with the previously obtained WDFs [96].

After obtaining four WDFs at choosen shears ($X1$, $Y1$), ($X2$, $Y1$), ($X1$, $Y2$) and ($X2$, $Y2$), the four dimensional addition was performed over $P_{X1}, P_{X2}, P_{Y1}, P_{Y2}$ axes to determine B as defined in Eq. 4.6. The experimentally obtained WDF is a two-dimensional (P_X, P_Y) function, keeping two dimensions (X, Y) to be constant. However, after addition of four WDFs, the dimension for B is a four-dimensional function (P_{X1}, P_{X2}, P_{Y1}, P_{Y2}) and other four dimensions ($X1$, $X2$, $Y1$, $Y2$) are fixed. Equation 4.6 shows the generation of a four-dimensional matrix after adding four two-dimensional functions. Proper axes should be considered while adding. The maximum value of B was determined to verify the violation of Bell's inequality.

Considering $X1$=0, P_{X1}=0, $X2$=X, P_{X2}=0, $Y1$=0, P_{Y1}=0, $Y2$=0, $P_{Y2} = P_Y$, the 2D surface plot of $|B|$ varying with X and P_Y described by Eq. 4.8 is shown in Fig. 4.4. From the plot, location of the maximum of $|B|$ has been determined that matches with the theory. The $|B_{max}|$ obtained from Fig. 4.4 is 2.1793, which indicates that the continuous variables of optical vortex field are non-separable.

It shows scatter since the vortices have been generated through diffraction from the SLM. One may see the experimental results of intensity correlations for different order of vortices formed using SLM vis a vis a Gaussian laser beam for a comparison [106]. In the present case, $|B_{max}|$ can be used to obtain the degree of entanglement since the earlier results also point out an increase in information entropy, a quantity proportional with the order of a vortex.

Fig. 4.5 shows the variation of maximum Bell's inequality violation ($|B_{max}|$) for Gaussian beam ($n = m = 0$) and optical vortices of order n =1–3, $m = 0$.

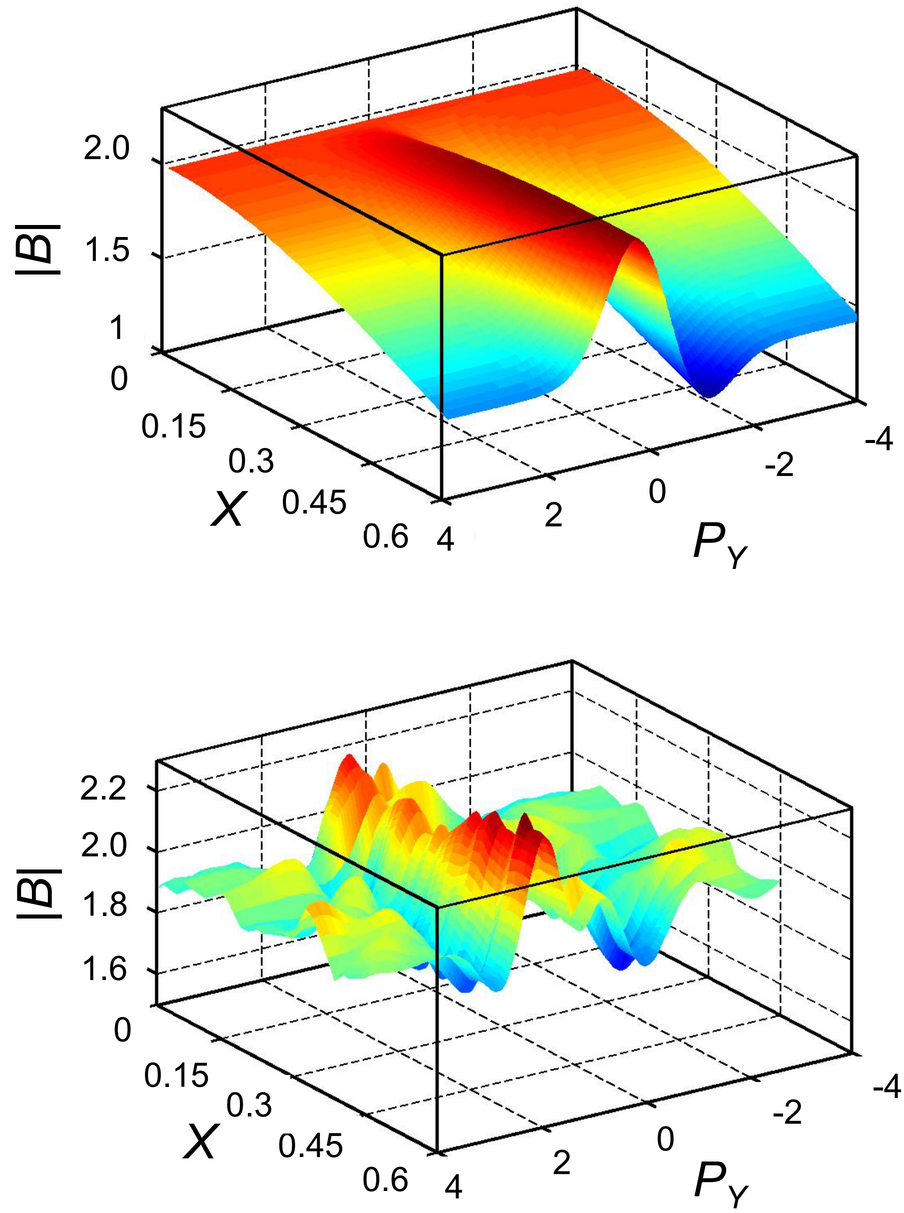

Figure 4.4: Variation of $|B|$ with X and P_Y (Eq. 4.8) for $n = 1$ and $m = 0$. Theoretical (top) and experimental (bottom).

Order (n)	$\lvert B_{max} \rvert$	(X_1, X_2, Y_1, Y_2)
0	2.00	(0.00, 0.58, 0.00, 0.00)
1	2.24	($-$0.07, 0.40, $-$0.05, 0.26)
2	2.35	(0.09, $-$0.40, 0.00, 0.00)
3	2.40	($-$0.09, 0.35, $-$0.01, 0.06)

Table 4.1: Theoretical values of variables providing $|B_{max}|$.

From the Fig. 4.5, it is clear that there is no Bell's inequality violation for Gaussian beam. However for optical vortex beams, the Bell's inequality has been violated. The amount of Bell's violation increases with the increase in order of the vortices. The amount of non-local correlations increases with the order of an optical vortex due to the increase in Bell's violation parameter (B_{max}). We have also performed experiments around the point of maximum and observed that amount of Bell's violation decreases as we move away from the point of maxima.

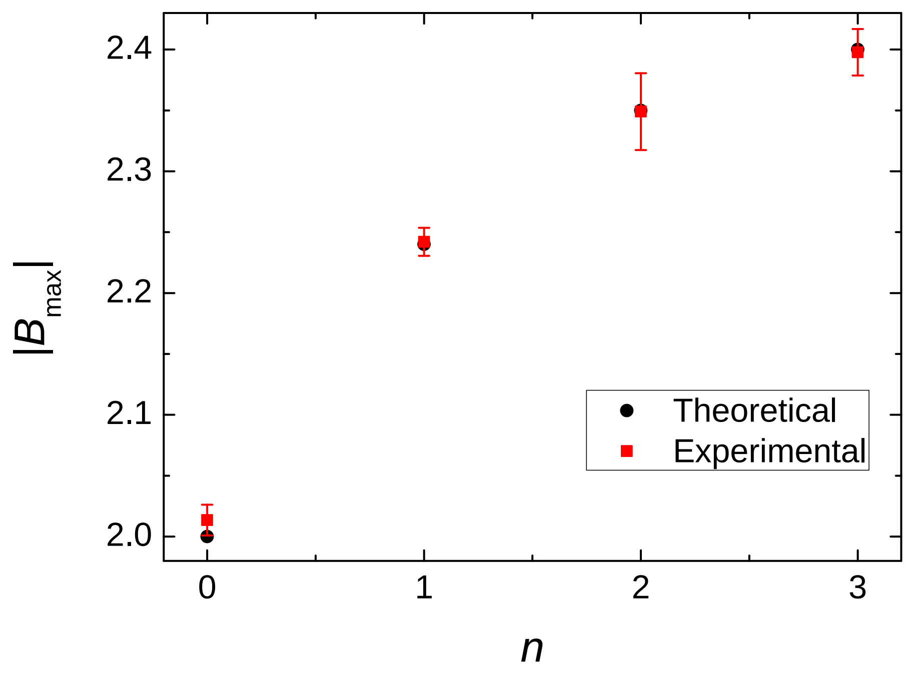

Figure 4.5: Variation of $|B_{max}|$ with the order of vortex n ($m = 0$).

To estimate the experimental error, the experiment was repeated for five times.

In every set of experiment, four WDFs were determined and for each WDF, two sets of interferograms corresponding to real and imaginary component of TPCF were recorded. $|B_{max}|$ was calculated for each set of experiments. The $|B_{max}|$ used in Fig. 4.5 is the average of five $|B_{max}|$ determined from each set of experimental interferograms. Errors are the standard deviations for five values of all the $|B_{max}|$.

4.4 Conclusion

In conclusion, we have experimentally verified the quantum inspired optical entanglement of classical optical vortex beams having phase singularities. We have shown that these classical beams violate Bell's inequality for continuous variables. The extent of violation of Bell's inequality increases with the increase in its topological charge. To obtain this, we have used the Fourier transform of two-point correlation function that provides us the Wigner distribution function of such beams. The violation of Bell's inequality in phase-space (x, p_x; y, p_y) clearly shows the existence of different spatial correlation properties for optical vortices compared to the Gaussian beam, which is similar to entanglement in quantum systems. One must be able to see this type of entanglement for electron vortex beams also due to the generic nature of vorticity.

The phrase "classical entanglement" has been used here to show the non-separability of position and momentum for a light beam. It does not imply non-locality for spatially separated photons associated with quantum entanglement. Our results suggest that the non-separability is enough for the violation of Bell's inequality.

Chapter 5

Entanglement of quantum optical elliptical vortex

Recently, quantum elliptic vortex (QEV) state has been generated by coupling squeezed coherent states of two modes with beam splitter (BS) or a dual channel directional coupler (DCDC) [107, 108, 109, 110, 111]. Both the components, BS and DCDC, find practical applications in optical coherence tomography. The QEV states studied by the authors can also be produced with experimental techniques which implement creation and annihilation operators [112]. To study the properties of quantum states a number of (quasi)probability distributions have been defined [113, 114, 115]. However, among all the (quasi)probability distributions, the Wigner distribution function (WDF) stands out, as it is real, nonsingular, yields correct quantum-mechanical operator averages in terms of phase-space integrals, and possesses positive definite marginal distributions. The WDF has come to play an ever increasing role in the description of both coherent and partially coherent beams and their passage through first order optical systems. Once the WDF is known, the other properties of the system can be calculated from it. Keeping this in mind, we calculated the WDF of the QEV states [31]. We observed quantum interferences due to coupling between the two modes.

We calculate the entanglement of a generalized elliptical vortex formed by quantized radiation field, using WDF for such states. We observed that there is a critical squeezing parameter above which the entanglement is less for higher vorticity, which is counter intuitive. By changing the squeezing parameter, the entanglement can also be controlled.

In this chapter, we discuss how this coupling could be used to generate controlled entanglement for application to quantum computation and quantum information. We show this by quantifying the entanglement in terms of the logarithmic negativity, a quantity evaluated in terms of symplectic eigenvalues of the covariance matrix corresponding to the state. We would like to emphasize that the logarithmic negativity can be used as a quantifier only for a Gaussian state in partitions of the kind 1xN (1 party entangled to a set of N other parties); it cannot be used for the general multi-partite states. Section 5.1 discusses the method for the generation of quantum elliptical vortex by using DCDC. In section 5.2, we have discussed the computation of WDF. The generation of controlled entanglement is discussed in section 5.3 and finally we conclude in section 5.4.

5.1 Generation of displaced QEV state using dual channel directional coupler (DCDC)

For two-mode states characterized by the annihilation operators a_1 and a_2, a coupling transformations can be generated by evolution under a Hamiltonian of the form $H = g(a_1^\dagger a_2 e^{i\phi} + \text{h.c.})$. Agarwal and Banerjee constructed circular vortex state using the above Hamiltonian H [107] described for BS/DCDC, and studied the properties of its entropy, while Kim et al. examined the question of the generation of entangled state by a beam splitter using Fock states as input fields [111]. Considering output operators $a_i^\dagger(out)$ are generated by the unitary transform $\mathcal{U}^\dagger a_i^\dagger(in)\mathcal{U}$ $(i = 1, 2)$, for the above mentioned Hamiltonian

$$\begin{bmatrix} a_1^\dagger(out) \\ a_2^\dagger(out) \end{bmatrix} = \begin{bmatrix} A_1 & A_2 \\ A_2 & A_1^* \end{bmatrix} \begin{bmatrix} a_1^\dagger(in) \\ a_2^\dagger(in) \end{bmatrix} \tag{5.1}$$

where $\mathcal{U} = e^{-iH}$. A_1 and A_2 denote transmissivity and reflectivity of the BS respectively and satisfy the relations $|A_1|^2 + |A_2|^2 = 1$, and $A_1^* A_2 + A_2^* A_1 = 0$. Mixing of equal amount $(A_1 = A_2)$ generates a circular vortex which has been dealt quantum mechanically elsewhere. In the cases where the coefficients of mixing (A_i) are not equal, they produce an elliptical vortex. As the asymmetry becomes larger and larger, more "which path" information is available, and the quantum interference effect is correspondingly diminished. Somewhat surprisingly, this reduced interference has been found to be extremely useful in a number of quantum information processing applications in linear optics, such as, quantum computing gates and quantum cloning machines.

We consider two separate squeezed coherent states (which are basically displaced vacuum modes) as our input states and couple them through a BS or DCDC. A quantum state is said to be squeezed when the noise in one variable is reduced below the symmetric limit at the expense of the increased noise in the conjugate variable such that the Heisenberg uncertainty relation is not violated. At this point, we change our label for the modes from (1, 2) to (x, y). If we look at any of the output states after m times the operation is performed, it is given by

$$|\Psi^D_{qev}\rangle = \left[\eta_x a^\dagger_x + i\eta_y a^\dagger_y\right]^m S_x(\zeta_x)S_y(\zeta_y)D_x(\alpha_x)D_y(\alpha_y)|0,0\rangle, \tag{5.2}$$

where $\mathcal{N}$ is the normalization constant and ζ_i is the squeezing parameter. $S_i(\zeta_i) = \exp(\zeta^*_i a^{\dagger 2}_i - \zeta_i a^2_i)$ and $D_i(\alpha_i) = \exp(\alpha^*_i a^\dagger_i - \alpha_i a_i)$ are the usual squeezing and displacement operators corresponding to x and y directions (the index $i = x, y$). α_i are the eigenvalues of the annihilation operator of coherent states $|\alpha_i\rangle$. We call these states displaced quantum optical elliptical vortex (DQEV). The term in square bracket, generated by BS/DCDC, is responsible for the elliptical vortex. If we put $\eta_x = \eta_y = 1$, $\zeta_x = \zeta_y = \zeta$ (real), it reduces to the displaced circular vortex state in a displaced circular Gaussian beam (DCCV): $|\Psi^D_{ccv}\rangle$. $|\Psi^D_{ccv}\rangle$, a circular vortex in circular beam, is discussed in detail in using Q function. For the case $\zeta_x \neq \zeta_y$, the beam profile becomes elliptical, whereas $\eta_x \neq \eta_y$ refers to elliptical vortex. The parameters in the generator of the vortex term η_i are trivially connected to the reflection and transmission of the BS, or the coupling ratios for DCDC, as described in Eq. 5.1.

5.2 Computation of Wigner distribution function of the QEV state

We change our variables to shifted (displaced) and scaled ones as $X_1 = \frac{x-x_0}{\sigma_x}$, $Y_1 = \frac{y-y_0}{\sigma_y}$, $P_{x_1} = \frac{\sigma_x}{\sqrt{2}}(p_x - p_{x0})$, $P_{y_1} = \frac{\sigma_y}{\sqrt{2}}(p_y - p_{y0})$, $X_2 = \frac{\sigma_y}{2\sigma_x}(x - x_0)$, $Y_2 = \frac{\sigma_x}{2\sigma_y}(y - y_0)$, $P_{x_2} = \frac{\sigma_y^3}{\sqrt{2}}(p_x - p_{x_0})$, $P_{y2} = \frac{\sigma_x^3}{\sqrt{2}}(p_y - p_{y_0})$. By considering $x_0 = \Re(\alpha x)$ and $x_0 = \Re(\alpha x)$, we have calculated the four-dimensional WDF [116] of QEV state as defined in Eq. 1.6

$$
\begin{aligned}
W(x, y, p_x, p_y) &= \frac{2^{(m-4)m!}}{\pi\sqrt{\pi}\Gamma(m+\frac{1}{2})}\left[-2(\sigma_x^2+\sigma_y^2)\right]^m \\
&\quad \times \exp\left[-(X_1^2 + X_2^2 + P_{X_1}^2 + P_{Y_1}^2)\right] \\
&\quad \times L_m^{-1/2}\left[\frac{P_{X_2}^2 + P_{Y_2}^2 - X_2^2 - Y_2^2}{\sigma_x^2+\sigma_y^2}\right] \qquad (5.3)
\end{aligned}
$$

where $L_m^{-1/2}$ is associated Laguerre polynomial (ALP). We point that the effect of $D_i(\alpha_i)$ is nothing but producing a displacement of the center of the beam as well as the vortex (x_0, y_0). So, we drop this term and call these states as QEV. Note that in Eq. 5.3, the changed variables in the Gaussian term are different from the changed variables in the argument of the ALP term. In case of circular vortex the hole and vortex terms factor out as a product $r^{2m}L_m^0$ [117], along with the Gaussian term. In the present case, the usual Gaussian term is factored out nicely, but the hole term (r^{2m}) is not separated out from the Laguerre term. We notice that it is embedded in the ALP term. Here, one can be reminded of the Rodrigues' formula for the ALP,

$$
L_m^\alpha = \frac{(-1)^m}{m!}e^{x^2}x^{-2\alpha}\frac{d^m}{dx^m}\left[e^{-x^2}x^{2(m+\alpha)}\right]. \qquad (5.4)
$$

Eq. 5.4 ensures that the elliptical vortex may be expressed as a combination of circular vortices from 0 to m.

5.3 Entanglement of QEV state

In this section, we study entanglement of the vortex states with change in one of the squeezing parameters. The measure of entanglement has been done in terms of logarithmic negativity, which is well defined for the Gaussian states. It is well known that a two mode squeezed state or two squeezed mode state can be completely characterized by its first and second statistical moments given the covariance matrix Σ. The squeezed vacuum state also falls under the class of Gaussian states. Now, we focus on our method for generating the vortex state by the propagation of light through a BS or coupled waveguides, the unitary operations, which currently are used in quantum architectures and quantum random walks. Here, we would like to draw attention to the lemma: "If U is a unitary map corresponding to a symplectic transformation in the phase space, i.e. if $U = \exp(-iH)$ with Hermitian H and at most bi-linear in the field operators, then $\delta A[U\rho U^\dagger] = \delta A[\rho]$" [118]. The proof of the lemma ensures that single-mode displacement and squeezing operations, as well as two-mode evolutions as those induced by a beam splitter or a parametric amplifier; do not change the Gaussian character of a quantum state. As the generalized vortex states, we considered, are generated only by such operations, it qualifies to be Gaussian. Note that since the first statistical moments can be arbitrarily adjusted by local unitary operations, it does not affect any property related to entanglement or mixedness and thus the behavior of the covariance matrix Σ is all important for the study of the entanglement. Therefore, the logarithmic negativity E_N, a quantity evaluated in terms of the symplectic eigenvalues of the covariance matrix Σ, and measure of the entanglement for a Gaussian state, can be applied to measure the entanglement for the QEV states. The elements of the covariance matrix Σ are given, in terms of conjugate observables, in the symmetrized form

$$\Sigma = \begin{bmatrix} \alpha & \mu \\ \mu^T & \beta \end{bmatrix} \tag{5.5}$$

with

$$\begin{aligned} \alpha &= \begin{bmatrix} \langle x^2 \rangle & \langle \frac{xp_x + p_x x}{2} \rangle \\ \langle \frac{xp_x + p_x x}{2} \rangle & \langle P_x^2 \rangle \end{bmatrix}, \\ \beta &= \begin{bmatrix} \langle y^2 \rangle & \langle \frac{yp_y + p_y y}{2} \rangle \\ \langle \frac{yp_y + p_y y}{2} \rangle & \langle P_y^2 \rangle \end{bmatrix}, \end{aligned}$$

$$\text{and} \quad \mu \quad = \quad \begin{bmatrix} \langle \frac{xy+yx}{2} \rangle & \langle \frac{xp_y+p_yx}{2} \rangle \\ \langle \frac{yp_x+p_xy}{2} \rangle & \langle \frac{p_xp_y+p_yp_x}{2} \rangle \end{bmatrix}. \tag{5.6}$$

The structure of Σ ensures that it is the transpose of itself ($\Sigma^T = \Sigma$). The symmetric operator averages in the matrix elements of Σ are calculated from the WDF using the relation

$$\langle \widehat{O} \rangle = \int \int_{-\infty}^{\infty} dx\; dp_x \int \int_{-\infty}^{\infty} dy\; dp_y\; \widehat{O}\; W(x, y, p_x, p_y). \tag{5.7}$$

The condition for entanglement of a Gaussian state is derived from the Peres-Horodecki positive partial transpose (PPT) criterion, according to which the smallest symplectic eigenvalues $\nu_<$ of the transpose of matrix Σ should satisfy

$$\nu_< < \frac{1}{2}, \tag{5.8}$$

where $\nu_< = \min[\nu_+, \nu_-]$. In this definition eigenvalues (ν_+, ν_-) are given by

$$\nu_\pm = \sqrt{\frac{\Delta(\Sigma) \pm \sqrt{\Delta(\Sigma)^2 - 4\mathrm{Det}(\Sigma)}}{2}} \tag{5.9}$$

where $\Delta(\Sigma) = \mathrm{Det}(\alpha) + \mathrm{Det}(\beta) - 2\mathrm{Det}(\mu)$, Det denotes the determinant. Thus according to the condition in Eq. 5.8, when $\nu_< \geq 1/2$, Gaussian states become separable. The corresponding quantification of entanglement is given by the logarithmic negativity of E_N defined as

$$E_N = \max\left[0, -\ln(2\nu_<)\right]. \tag{5.10}$$

At this point, we note an interesting observation from Fig. 5 and 6 in Ref. [119] as shown in Fig. 5.1 here, which is not mentioned by the authors of that reference. We note that in both the plots the entanglement show similar periodicity over mixing ratio, but lagging/leading with a phase factor of $\pi/2$, as outcome of BS/DCDC coupling. The separable state acquires entanglement due to the action of BS/DCDC. Especially in DCDC the entangled state again becomes separable after certain distance, and the process repeats periodically. It is interesting to note similar oscillation from one to the other type has also been reported elsewhere. It means that through DCDC a two (separate) squeezed state mode (TSSM) is converted to a two mode squeezed state (TMSS) and again to TSSM

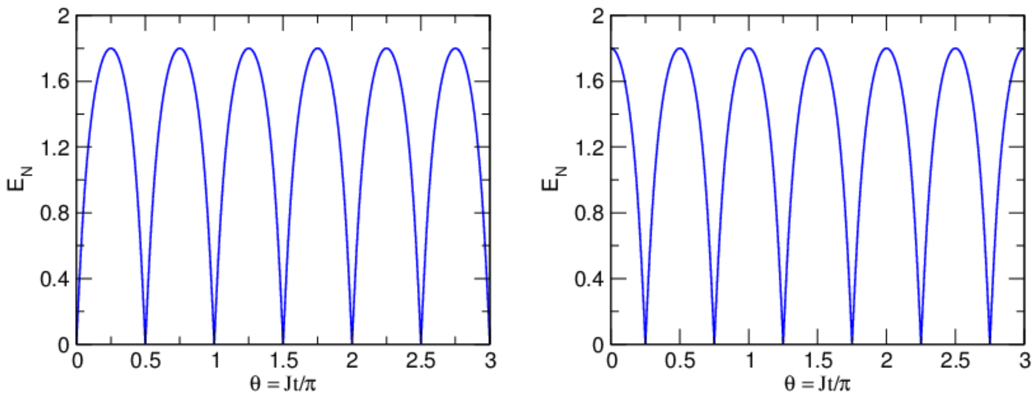

(a) Time evolution of logarithmic negativity E_N for the state $|\zeta\rangle = |\zeta_a\rangle \bigotimes |\zeta_b\rangle$, separable two mode squeezed state as an input. Here $|\zeta_i\rangle = \exp(0.5r(i^{\dagger^2} - i^2)|0\rangle$ and $i \rightarrow a, b$.

(b) Time evolution of logarithmic negativity E_N for the initial entangled state $|\xi\rangle = \exp(r(a^\dagger b^\dagger - ab))|00\rangle$, an entangled two mode squeezed state as an input.

Figure 5.1: Comparision of time dependent logarithmic negativity E_N for (a) separable $|\zeta\rangle$ and (b) entangled $|\xi\rangle$ two mode squeezed state as input. Here amount of squeezing is taken to be $r = 0.9$. These plots are obtained from arXiv:0907.2432v3.

periodically. Our states, described by the WDF in Eq. 5.4, describe both the extreme cases, along with the generalized states, in between.

Remembering the fact that the effect of $D_i(\alpha_i)$ is nothing but shifting the center of the beam as well as the vortex, we choose $x_0 = y_0 = p_{x_0} = p_{y_0} = 0$, in the WDF, without loss of any new information, and compute the dependence of entanglement on squeezing parameter. The states in between may also be described by the QEV state, expressed by Eqs. 5.2-5.3. We report a critical squeezing parameter, above which, higher AM means lower entanglement. We have computed the entanglement for a choice of parameters $\sigma_y = \sqrt{5\sigma_x}$. In terms of ζ_i, the relationship is linear: $\zeta_y = \frac{\ln 5}{4} + \frac{\zeta_x}{2}$. We have plotted the entanglement, E_N, in Fig. 5.2, for $m = 0$ to 5, i.e. for different orders of the vortex, as a function of σ_x. First of all, we analyze our observation for $m = 0$. For this state, we observe entanglement, which is counter intuitive. $m = 0$ means that no vortex is formed, thus there should be no entanglement, as it is TSSM. The

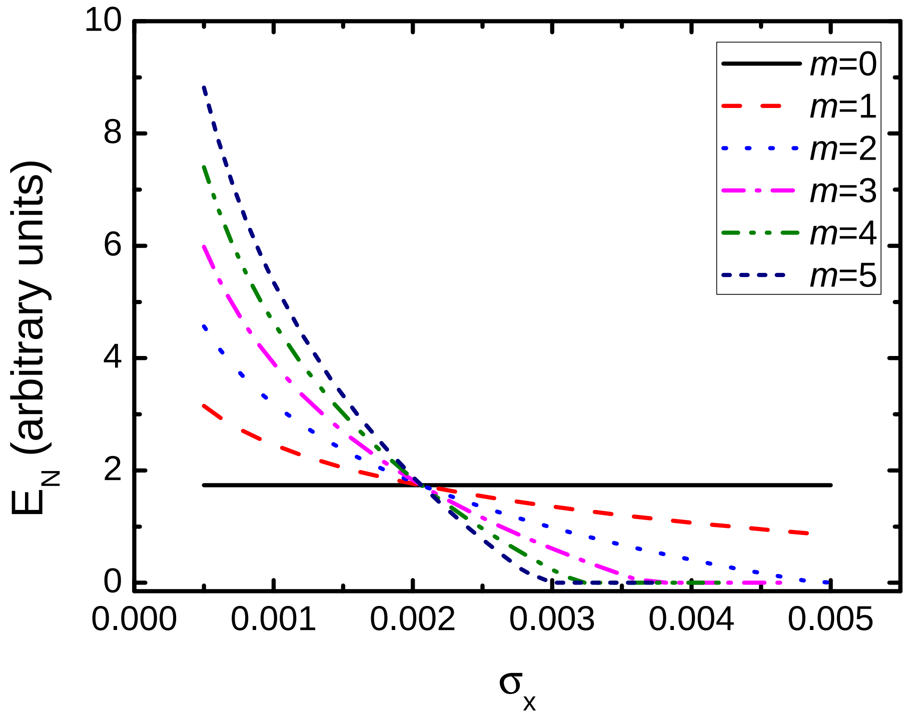

Figure 5.2: Plot of entanglement E_N (in arbitrary units) versus σ_x, for different charge (m) of QEV. Note that the finite constant entanglement for m=0 and critical point of squeezing parameter, where the curves $m \neq 0$ cross each other.

reason for this apparent contradiction is explained below. It is definitely true that if the two squeezing parameters are random, then the state would be separable. However, we suspect that due to our (or, logically speaking, any) choice of a specific relation between the squeezing parameters, some sort of entanglement is generated. Thus we argue that the constant entanglement, generated in our computation, is due to the non-random choice of squeezing parameters. The observation of the constant value of the entanglement supports the logic that as it is generated with some fixed relationship, it remains constant. We have verified the fact that some other fixed relationship produces entanglement, with some other constant value. However, the other dependencies of the parameters will be considered in future correspondences, if found with interesting features.

Similar properties are again evident from the plot of entanglement vs. ζ_x, in Fig. 5.3. The intercepts of the plots vary as $\ln K$, defined after Eq. 5.3. The important observation in both the figures is that the above a critical point, $\sigma_x = 0.002$ ($\zeta_x = -3.1073 = 3.1073e^{i\pi}$), the higher charge or the higher OAM

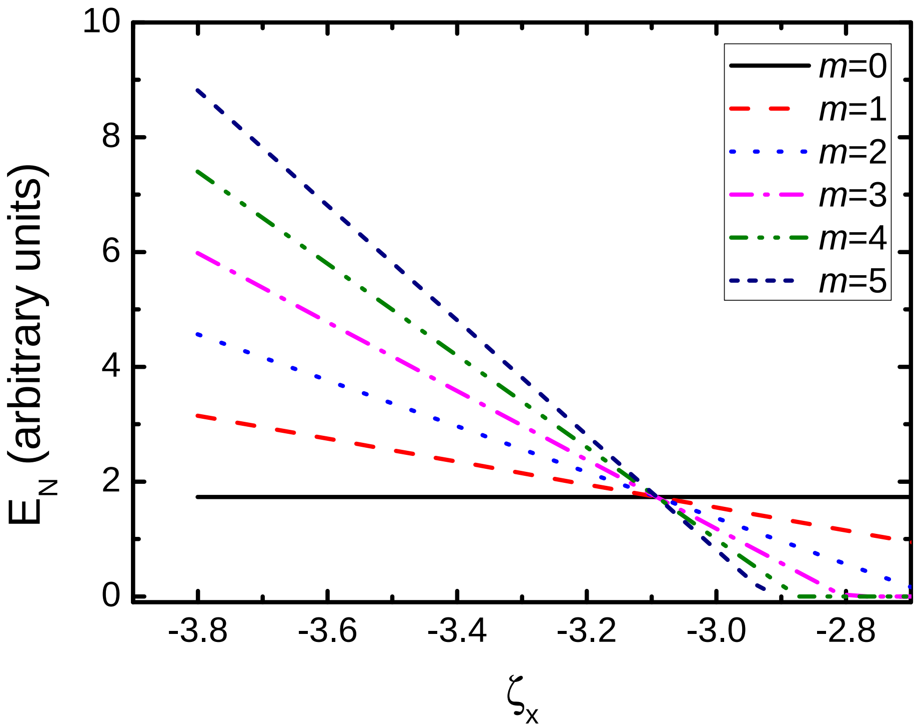

Figure 5.3: Plot of entanglement E_N (in arbitrary units) versus ζ_x, for different charge (m) of QEV. Note that the finite constant entanglement for m=0 and critical point of squeezing parameter, where the curves $m \neq 0$ cross each other.

corresponds to lower entanglement. The squeezing parameter ζ_i is complex in general. However, most of the studies consider only real positive values of the parameter. We report our work in the complex domain of the parameter from the expression of ζ_x mentioned above, where the negativity is realized in the phase factor of the complex squeezing parameter. A critical value of the squeezing parameter, above which the resolution of the Mach-Zehnder interferometer decreases, has been reported [120] previously also. It implies that the different domains of the generally complex squeezing parameters should be explored for the different experimental setups.

5.4 Conclusion

To conclude, we proposed the two well-known mechanisms, using DCDC and BS, to generate a quantum optical elliptic vortex (QEV) states. We have argued that the QEV is a Gaussian state as squeezing or coupling between the two modes do not change this property. Thus the entanglement follows the Peres-Horodecki PPT criterion and the logarithmic negativity of the lowest eigenvalue of the covariance matrix. We have computed the entanglement of such quantum elliptical vortex from the four-dimensional WDF, which is used to find out covariance matrix and therefore, the logarithmic negativity. We show that by changing the squeezing parameter one can control the entanglement. We observed a critical point above which the increase in vorticity decreases the entanglement.

Chapter 6

Annihilation of vortex dipoles in Bose-Einstein condensate

In recent years, the propagation dynamics of optical vortices in linear and non-linear media have gained interest in the literature [36, 38, 121, 122, 123, 124]. The trajectories of the vortices while propagation show that the vortices move around in the transverse plane of the beam. They display interesting dynamical behavior, which includes moving toward each other, rotating around each other, or annihilating each other. For example, propagation dynamics of a non-centered vortex and annihilation of a vortex dipole are shown Figs. 1.8 and 1.9. In Fig. 1.9, annihilation of the vortex dipole is clearly visible from the intensity as well as the phase distribution. There are two main factors which govern the propagation dynamics of vortices – the intensity gradient and the phase gradient produced by the vortices and the host beam which depend on position of the vortices in the host beam. After the annihilation of an optical vortex dipole, formation of soliton has also been observed [58, 125, 126].

In optics, annihilation of vortex dipoles embedded in a Gaussian host beam has been studied extensively [123, 124]. These annihilation events can be accelerated by manipulating the background phase function of the beam [39]. In non-linear systems like BEC, the annihilation of a vortex dipole in the BEC formed by an obstacle that can be a Gaussian or a vortex beam of light, has been mentioned in a number of theoretical studies [51, 127, 128, 129]. Large number of factors, such as position of the generated vortex and the anti-vortex, density function, scattering length affect the annihilation events. Thus the factors affecting the annihilation of BEC vortices are very much similar to annihilation of optical vortices. However, there is a lack of extensive study on this topic and more importantly, no definite signatures of vortex dipole annihilation in BEC were observed in the experiment [47]. The study of vortex dipole annihilation in BEC will shed light on the process which influences the separation between vortex-antivortex and conditions for annihilation along with other phenomena arising from the dynamics of vortices of the dipole.

In this chapter, we present analytical as well as numerical results related to vortex dipole annihilation for an oblate BEC at zero temperature. The results are obtained using Gross-Pitaevskii (GP) equation. Condensate with diametric vortex dipole and gray soliton are studied and this is described in section 6.2. Section 6.2 contains studies done in the strong as well as weak interacting systems. Annihilation of vortex dipoles is analyzed from the energies obtained from the analytical calculations. The numerical results, confirming the analytic results, are discussed in Section 6.3, and we then conclude.

6.1 Superfluid vortex dipole and its generation

There are several theoretical and experimental proposals to generate vortices in non-rotating traps. These include stirring of the condensate using blue-detuned laser or several laser beams [47, 57], adiabatic passage [130], Raman transitions in binary condensate systems [131], laser beam vortex guiding [132], and phase imprinting [49]. Among these methods, the easiest one to nucleate vortex dipoles is by stirring a BEC with a blue-detuned laser beam which can be a Gaussian or a vortex beam. When the velocity of the laser beam exceeds a critical velocity, vortex-antivortex pairs are released from the localized dip in the number density created due to the laser beam. These vortex dipoles then move through the BEC and exhibit various interesting dynamics [48, 57, 133]. The critical velocity depends on the number density, width and intensity of the laser beam, and the frequency of the trapping potential. This nucleation process exhibits a high degree of coherence and stability, allowing us to map out the annihilation of the dipoles. In an axis-symmetric trap, a vortex dipole is a metastable state of superfluid flow with long lifetime.

In the mean-field approximation, the dynamics of a dilute BEC is very well described by the GP equation

$$i\hbar\partial_t\Psi(\mathbf{r},t) = [\mathcal{H} + U|\Psi(\mathbf{r},t)|^2]\Psi(\mathbf{r},t), \tag{6.1}$$

where $\mathcal{H}$, U and Ψ are the single-particle Hamiltonian, interaction strength and order parameter of the condensate respectively. The order parameter, Ψ, is normalized to N, the total number of atoms in the condensate. In the present case, the single-particle Hamiltonian $\mathcal{H}$ consists of the kinetic-energy operator, an axis-symmetric harmonic trapping potential, and a Gaussian obstacle potential, that is,

$$\mathcal{H} = -\frac{\hbar^2}{2m}\nabla^2 + \frac{m\omega^2}{2}(x^2 + \alpha^2 y^2 + \beta^2 z^2) + V_{\rm obs}(x,y,t), \tag{6.2}$$

where α and β are the anisotropies along y and z axis respectively, m is the mass of particles used in condensate, ω is the trapping potential, and $V_{\rm obs}(x,y,t)$ is the repulsive Gaussian obstacle potential. Experimentally, a blue-detuned laser beam is used to generate the $V_{\rm obs}(x,y,t)$ and it can be written as

$$V_{\rm obs}(x,y,t) = V_0(t)\exp\left[-2\frac{(x-vt)^2 + y^2}{w_0^2}\right], \tag{6.3}$$

where $V_0(t)$ is the potential at the center of the Gaussian obstacle at time t, v is the velocity of the obstacle along x-axis, and w_0 is the radius of repulsive obstacle potential. In the present work, we consider the motion of obstacle along x-axis only. Defining the oscillator length of the trapping potential as $a_{\rm osc} = \sqrt{\hbar/(m\omega)}$, and considering $\hbar\omega$ as the unit of energy, we can then rewrite the equations in dimensionless form with transformations $\tilde{\mathbf{r}} = \mathbf{r}/a_{\rm osc}$, $\tilde{t} = t\omega$, and the transformed order parameter assumes the form

$$\phi(\tilde{\mathbf{r}},\tilde{t}) = \sqrt{\frac{a_{\rm osc}^3}{N}}\Psi(\mathbf{r},t). \tag{6.4}$$

For the sake of notational simplicity, hereafter we denote the scaled quantities without tilde in the rest of the manuscript. In a pancake-shaped trap $\alpha = 1$ and

$\beta \gg 1$ and the order parameter can then be written as

$$\phi(\mathbf{r}, t) = \psi(x, y, t)\zeta(z) \exp(-i\beta t/2), \tag{6.5}$$

where $\zeta(z) = [\beta/(2\pi)]^{1/4} \exp(-\beta z^2/4)$. The Eq. 6.1 is then reduced to the two dimensional form

$$\left[-\frac{1}{2}\left(\frac{\partial^2}{\partial x^2} + \frac{\partial^2}{\partial y^2}\right) + \frac{x^2 + y^2}{2} + \frac{V_{\rm obs}(x, y, t)}{\hbar\omega} \right.$$
$$\left. + u|\psi(\mathbf{r}, t)|^2 - i\frac{\partial}{\partial t}\right] \psi(\mathbf{r}, t) = 0, \tag{6.6}$$

where $u = 2aN\sqrt{2\pi\beta}/a_{\rm osc}$, with a as the s-wave scattering length, is the modified interaction strength. In the present work, we consider condensate consisting of ^{87}Rb atoms in $F = 1$, $m_F = -1$ state with $a = 99a_0$ [134]. We have neglected a constant term corresponding to the energy along axial direction as it only shifts the energies and chemical potentials by a constant without affecting the dynamics. We solve this equation numerically using the Crank-Nicholson method [135].

6.2 Condensates with vortex dipole or gray soliton

To analyze the vortex dipole annihilation, we consider a model system where the vortex-antivortex dipole pair and gray soliton, which may be generated when annihilation of vortex dipole occurs, are static. However, we vary the distance of separation and examine the energy of the total system. The present system can be studied under two regimes: strongly interacting system, and weakly interacting system. The strongly interacting system is studied considering ϕ with Thomas-Fermi (TF) approximation and the weakly interacting system is studied considering the Gaussian form of ϕ.

6.2.1 Strongly interacting system with Thomas Fermi (TF) approximation

For the $Na/a_{\rm osc} \gg 1$ case, we use TF approximation to determine the steady state density profile and energy of the condensate. To begin with, we consider a condensate with vortex dipole and later, with gray soliton.

Diametric vortex dipole

We consider a condensate consisting of N atoms in a purely harmonic potential

$$V(x,y) = \frac{x^2+y^2}{2}. \tag{6.7}$$

Consider that the condensate has a vortex dipole, consisting of a vortex and an antivortex located at $(0, v_2)$ and $(0, -v_2)$, respectively. The cores of the vortex and antivortex can be approximated as circular regions centered around $(0, v_2)$ and $(0, -v_2)$ and with radii equal to the coherence length ξ. At the cores, we consider the density to be equal to zero. Hence, we use the TF approximation and adopt the following piecewise ansatz for density of the condensate

$$n(x,y) = \begin{cases} 0 & \text{for } x^2+y^2 > R^2 \\ 0 & \text{for } [x^2+(y\pm v_2)^2] \leqslant \xi^2 \\ \left[\dfrac{\mu - V(x,y)}{u}\right] & \text{for } \begin{cases} x^2+y^2 \leqslant R^2 \ \& \\ [x^2+(y\pm v_2)^2] > \xi^2, \end{cases} \end{cases} \tag{6.8}$$

where $R = \sqrt{2\mu}$ is the spatial extent of the condensate in TF approximation, and $\xi = 1/R$ is the coherence length at the center of the trap. Normalizing this ansatz yields

$$\frac{\pi\left(2 - 4R^4 + R^8 + 4R^2 v_2^2\right)}{4R^4 u} = 1. \tag{6.9}$$

This equation defines the radius of the condensate. The TF ansatz can be used to calculate the total potential energy arising from the regions outside the cores of the vortices and is given as

$$E_0 = \frac{\pi\left[1 - 3R^8 + R^{12} + 3R^2 v_2^2\left(2 + R^2 v_2^2\right)\right]}{12R^6 u}. \tag{6.10}$$

The main energy contribution from the vortex dipole is the kinetic energy due the velocity field associated with it. This energy can be approximated as [136]

$$E_{\rm KE} = \frac{R^2}{u}\mathrm{Log}\left(\frac{2v_2}{\xi}\right). \tag{6.11}$$

This relation is valid when $\xi \ll v_2 \ll R$ and in the present work, $\xi \sim 0.06$ and $R = 15.5\ a_{\rm osc}$. In order to estimate the energy contributions from the cores of the vortices, we approximate the density within the cores as

$$n(x,y) = \begin{cases} \dfrac{2n_0[x^2+(y-v_2)^2]}{x^2+(y-v_2)^2+\xi^2} & \text{for } [x^2+(y-v_2)^2] < \xi^2 \\ \dfrac{2n_0[x^2+(y+v_2)^2]}{x^2+(y+v_2)^2+\xi^2} & \text{for } [x^2+(y+v_2)^2] < \xi^2, \end{cases} \tag{6.12}$$

where n_0 is the average TF density on the circle $x^2+(y\pm v_2)^2 = \xi^2$. Assuming that the normalization is still defined by equation Eq. 6.9, Eq. 6.12 can be used to calculate energy contribution from the core region. The energy within the core consist of

$$E_{\rm c}^{\rm q} = \frac{6\pi n_0}{8}, \tag{6.13}$$

$$E_{\rm c}^{\rm tr} = \pi\xi^4({\rm Log}[4]-1)n_0, \tag{6.14}$$

$$E_{\rm c}^{\rm int} = 2\pi u\xi^2(3-{\rm Log}[16])n_0^2, \tag{6.15}$$

where, $E_{\rm c}^{\rm q}$, $E_{\rm c}^{\rm tr}$ and $E_{\rm c}^{\rm int}$ are the energies arising from the quantum pressure, trapping potential and interaction within the core region, respectively. Thus, the total energy of the condensate with a vortex dipole is

$$E_{\rm vd} = E_0 + E_{\rm KE} + E_{\rm c}^{\rm q} + E_{\rm c}^{\rm tr} + E_{\rm c}^{\rm int}. \tag{6.16}$$

The variation of $E_{\rm vd}$ as a function of v_2 is shown in Fig. 6.1.

Gray soliton

For gray soliton extending from $(0,\ -v_2)$ to $(0,\ v_2)$ along y-axis, we use the following piecewise ansatz in the TF approximation

$$n(x,y) = \begin{cases} 0 & \text{for } x^2+y^2 > R^2, \\ \left[\dfrac{\mu - V(x,y)}{u}\right] & \text{for } \begin{cases} x^2+y^2 \le R^2, \\ |x| > \xi, \\ |y| > v_2, \end{cases} \\ \left[\dfrac{\mu - V(x,y)}{u}\right]\dfrac{2x^2}{x^2+\xi^2} & \text{for } |x| \le \xi \ \&\ |y| \le v_2. \end{cases} \tag{6.17}$$

And, the normalization condition leads to following constraint on the radius of the condensate

$$\frac{1}{12R^3u}\left[3\pi R^7 + 4v_2\left(10 + 6R^4 - 3\pi\left(1 + R^4\right)(-2+\pi)R^2v_2^2\right)\right] = 1. \tag{6.18}$$

For the gray soliton, other than the quantum pressure, there is no need to separate out the energy associated with the trapping and interaction potential within the soliton. So, the total energy of the system is

$$E_{\rm s} = E_0 + E_{\rm c}^{\rm q}, \tag{6.19}$$

where, E_0 is the potential energy associated with the system and $E_{\rm c}^{\rm q}$ is the energy arising from the quantum pressure. These are given as

$$\begin{aligned} E_0 &= \int\int\left[V(x,y)n(x,y) + \frac{u}{2}n(x,y)^2\right]{\rm d}x{\rm d}y, \\ E_{\rm c}^{\rm q} &= \frac{1}{2}\int_{-\xi}^{\xi}\left[\int_{-v_2}^{v_2}|\nabla_{xy}\sqrt{n(x,y)}|^2{\rm d}y\right]{\rm d}x. \end{aligned} \tag{6.20}$$

From the expression of the $n(x,y)$ in Eq. 6.17, we obtained

$$\begin{aligned} E_0 &= \frac{1}{180R^5u}\left\{15\pi R^{11} + 3\left[236 - 75\pi + 20(19-6\pi)R^4 + 15(8-3\pi)R^8\right]v_2\right. \\ &\quad \left. +10R^2\left[-28 + 9\pi + 6(-3+\pi)R^4\right]v_2^3 - 9(-4+\pi)R^4v_2^5\right\} \end{aligned} \tag{6.21}$$

$$E_{\rm c}^{\rm q} = -\frac{(8+3\pi)v_2\left(-3R^2 + 3\xi^2 + v_2^2\right)}{48u\xi}. \tag{6.22}$$

Interestingly, the $E_{\rm c}^{\rm q}$ has a $1/\xi$ dependence, which is to be expected as smaller ξ implies larger density variation and translates to higher quantum pressure.

For illustration, the vortex dipole and gray soliton inside the condensate is shown in Fig. 6.2. The vortex dipole is located at (1, 0) and (−1, 0) while the gray soliton extends from (−1, 0) to (1, 0) along the x-axis. In the case of vortex dipoles, the phase varies from 0 to 2π, if one goes around the point of singularity. While in the case of gray soliton, there is a phase discontinuity of π along the line forming the soliton. The number density at the point of singularity is zero. In Fig. 6.1, E_s is plotted as a function of v_2 and the values varies from 0.05 $a_{\rm osc}$ to 2.0 $a_{\rm osc}$. From the figure, it is evident that for $v_2 \leqslant 0.2$, the value of $E_{\rm vd}$ is higher than $E_{\rm s}$ and hence, the gray soliton is the energetically favored state of the system. However when $v_2 > 0.2$, the vortex dipole state is the energetically favorable. This analytical result provides a compelling reason to study the annihilation of vortex dipoles and formation of gray solitons.

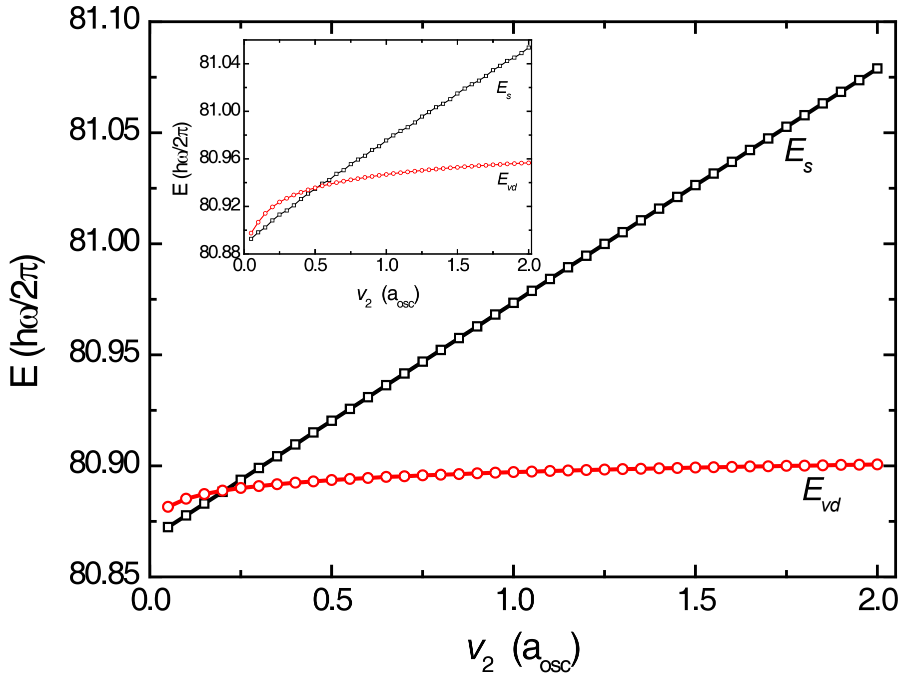

Figure 6.1: Comparing the energy of vortex dipole and band soliton under TF approximations. The crossover in energy can be seen through ansatz chosen and the analytical expressions obtained. Inset shows the variation of energy obtained by solving GP equation numerically. The difference in the value of v_2 for crossover in energy is due to the too ideal wave-function considered for the analytical calculations.

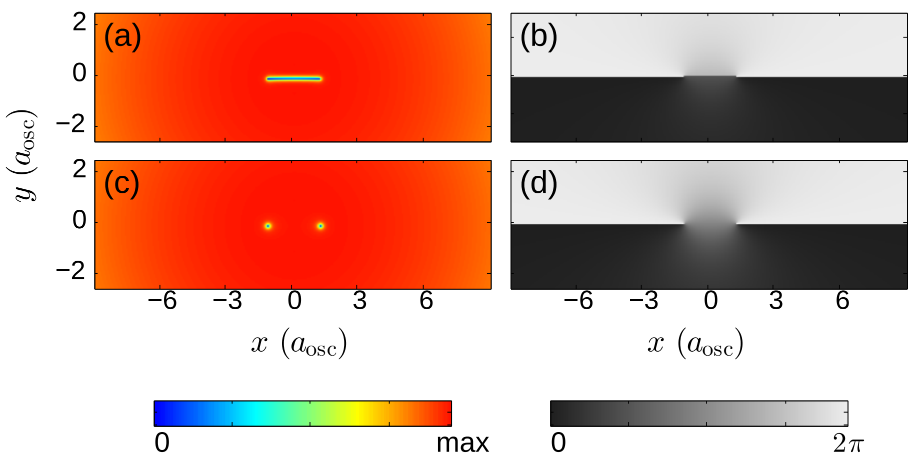

Figure 6.2: Band soliton (top) and vortex dipole (bottom) with density profile (left) and phase profile (right) obtained numerically.

6.2.2 Weakly interacting system with Gaussian approximation

In $Na/a_{\rm osc} \ll 1$ regime, a simplistic model of a vortex dipoles in the BEC of trapped dilute atomic gases can be considered as the superposition of harmonic oscillator eigenstates. The minimalist wave function which supports a vortex and antivortex at coordinates $(-a/c, -\sqrt{b/d})$ and $(-a/c, \sqrt{b/d})$ is

$$\psi(x,y) = e^{-i\mu t}\left(ia - b + ixc + dy^2\right)e^{-(x^2+y^2)/f}, \tag{6.23}$$

where a, b, c, d, and f are positive variational parameters and μ is the chemical potential of the system. The wave function is a superposition of the scaled ground state and the first and the second excited states of harmonic oscillator along the x and y-axes, respectively. The wave function is ideal for weakly interacting condensates.

We have considered that the vortex and antivortex are located on the diameter of the condensate. Without loss of generality, we consider the diameter as coinciding with the y-axis, which is equivalent to $a = 0$ in Eq. 6.23. Such an assumption does not modify the qualitative descriptions, but expressions are far less complicated. The wave function is then

$$\psi(x,y,t) = e^{-i\mu t}\left[-b + icx + dy^2\right]e^{-(x^2+y^2)/f}. \tag{6.24}$$

The nontrivial phase of the wave function θ is discontinuous along $x = 0$ line for $-\sqrt{b/d} \leqslant y \leqslant \sqrt{b/d}$. Across the discontinuity, there is a phase change from $-\pi$ to π as we traverse along x-axis from 0^- to 0^+ and this phase variation is shown in Fig. 6.3. So, there is a discontinuity across the y-axis and this is the typical phase pattern associated with vortex dipoles. For the present case, the ground state wave function is

$$\psi_{\rm g}(x,y,t) = -be^{-i\mu t}e^{-(x^2+y^2)/f}, \tag{6.25}$$

and from the normalization condition

$$\int_{-\infty}^{\infty}\int_{-\infty}^{\infty} |\psi_{\rm g}|^2 {\rm d}x{\rm d}y = 1, \tag{6.26}$$

we get the constraint equation

$$b^2 = \frac{2}{f\pi}. \tag{6.27}$$

For general considerations, rewrite the additional term as

$$\delta\psi(x, y, t) = e^{-i\mu t}\left(icx + dy^2\right)e^{-(x^2+y^2)/f}. \tag{6.28}$$

So that the total wave function $\psi = \psi_g + \delta\psi$, where $\delta\psi$ represents an elementary excitation of the condensate. We can calculate the total energy of the system, without the obstacle potential, as

$$E_{vd} = \int_{-\infty}^{\infty}\int_{\infty}^{\infty}\left[\frac{1}{2}|\nabla_{\perp}\psi(x, y)|^2 + \frac{x^2+y^2}{2}|\psi(x, y)|^2 + \times\ u|\psi(x, y)|^4\right]\mathrm{d}x\mathrm{d}y. \tag{6.29}$$

This is the energy of the condensate with a vortex dipole with the assumption that it is a weakly interacting system. Energy without the vortex may be calculated trivially [42]. In general, the energy added to the system due to the vortex dipole is not large compared to the total and for obvious reason, the angular momentum of the condensate is still zero.

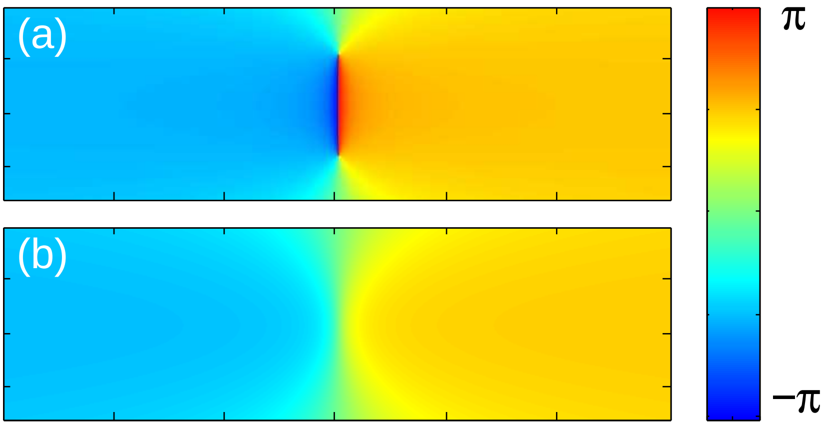

Figure 6.3: Phase pattern resulting due to a (a) vortex dipole and (b) gray soliton.

A slight modification to the wave function can describe a solitonic solution along y-axis. The form of the modified wave function is

$$\psi(x, y) = \left[b + icx + dy^2\right]e^{-(x^2+y^2)/f}, \tag{6.30}$$

where except for the change in the sign of b, all the terms remain unaltered as in Eq. 6.23. It is a *gray* soliton as the density $n \propto (b + dy^2)^2 + (cx)^2$ has a dip but is different from zero. The phase varies smoothly from $-\pi/2$ to $\pi/2$ along the normal to the line which connects $(0, -\sqrt{b/d})$ and $(0, \sqrt{b/d})$. This phase variation is shown in Fig. 6.3(b).

Using the wave function in Eq. 6.30, we can then evaluate the total energy of the system E_{gs} and calculate the energy difference between two possible states of the system

$$\Delta E = E_{\text{vd}} - E_{\text{gs}}, \tag{6.31}$$

which after evaluation is

$$\Delta E = \frac{bdf^2\pi}{256}\left[64b^2u + 15d^2f^2u + 8f(8 + c^2u)\right]. \tag{6.32}$$

The most general solution is when all the constants are positive, then $\Delta E > 0$ and the gray soliton is lower in energy. This shows that when the vortex-antivortex collides, it is energetically favorable for them to decay into gray soliton. As discussed in the results section, this is confirmed in the numerical calculations.

The analysis so far is for an ideal system at zero temperature, where we have neglected the quantum and thermal fluctuations and perturbations from imperfections. In addition, there is dissipation from three body collision losses in the condensates of dilute atomic gases.

6.3 Numerical Results

For the numerical computation, we choose ^{87}Rb with $N = 2 \times 10^6$ atoms. The trapping potential and obstacle laser potential parameters are similar as those considered in Ref. [47], i.e., $\omega/(2\pi) = 8$ Hz, $\beta = 11.25$, $V_0(0) = 93.0\ \hbar\omega$ and $w_0 = 10\ \mu$m. To nucleate the vortices on the edges of the condensate, the obstacle potential V_{obs} is initially located at $(-12.5\ a_{\text{osc}}, 0)$ and moves along the x direction at a constant velocity with decreasing intensity until V_{obs} vanishes at $(5.18\ a_{\text{osc}}, 0)$.

6.3.1 Vortex dipole nucleation

We study the nucleation of vortices by $V_{\rm obs}$ with the translation speed v ranging from 80 μm s^{-1} to 200 μm s^{-1}. Vortices are not nucleated when the speed is 80 μm s^{-1}. However, a vortex-antivortex or a vortex dipole is nucleated when the speed is in the range 90 μm s^{-1} $< v <$ 140 μm s^{-1}. Increasing the speed of obstacle generates two pairs of vortex dipoles when 140 μm s^{-1} $\leqslant v <$ 160 μm s^{-1} and more than two when $v \geqslant$ 160 μm s^{-1}. In other words, the number of vortex dipoles created can be controlled with the speed of the obstacle. Creation of vortex dipoles above a critical speed v_c is natural as the vortex nucleation must satisfy the Landau criterion [137]. The density and phase of the condensate after the nucleation of vortex dipole for v = 120 μm s^{-1} is shown in Fig. 6.4. The figure clearly shows nucleation dynamics of the vortex dipoles.

From numerical calculations, we have determined $v_c \approx$ 90 μm s^{-1}. This is, however, less than the local acoustic velocity of the medium $s = \sqrt{nU/m}$, which depends on the local condensate density. This also explains the reason for the predominant vortex dipole nucleation around the edge of the condensate where n is lower and s is accordingly lower.

6.3.2 Vortex dipole annihilation

To determine the energetically preferred state of the system, we examine the energy of the condensate with vortex dipole and gray soliton as a function of the separation v_2. The result is shown as the inset plot in Fig. 6.1. Like in the TF calculations, vortex dipole is the stable solution for larger v_2 but for $v_2 < 0.5a_{\rm osc}$ gray soliton is the stable solution. However, in the numerical results, the critical value of v_2 at which the vortex soliton overtakes gray soliton as the stable solution is higher than the TF values. This may be an account of the piecewise nature of the TF ansatz.

It is observed that the vortex dipole annihilation is critically dependent on the initial conditions of the nucleation, in particular, the vortex-antivortex separation, v_2. The annihilation occurs when the vortex dipole is generated with $v_2 < 0.5a_{\rm osc}$, which is consistent with the analytical results and solutions of time-independent

GP equation. The initial v_2 is, however, is dependent on the velocity v of the obstacle potential. For this reason, the annihilation events are observed only for specific range of v. As an example, the annihilation event when v is 120 μm s^{-1} is shown in Fig. 6.4. In Fig. 6.4, we can notice the density minima arising from the annihilation and propagating away from the obstacle potential.

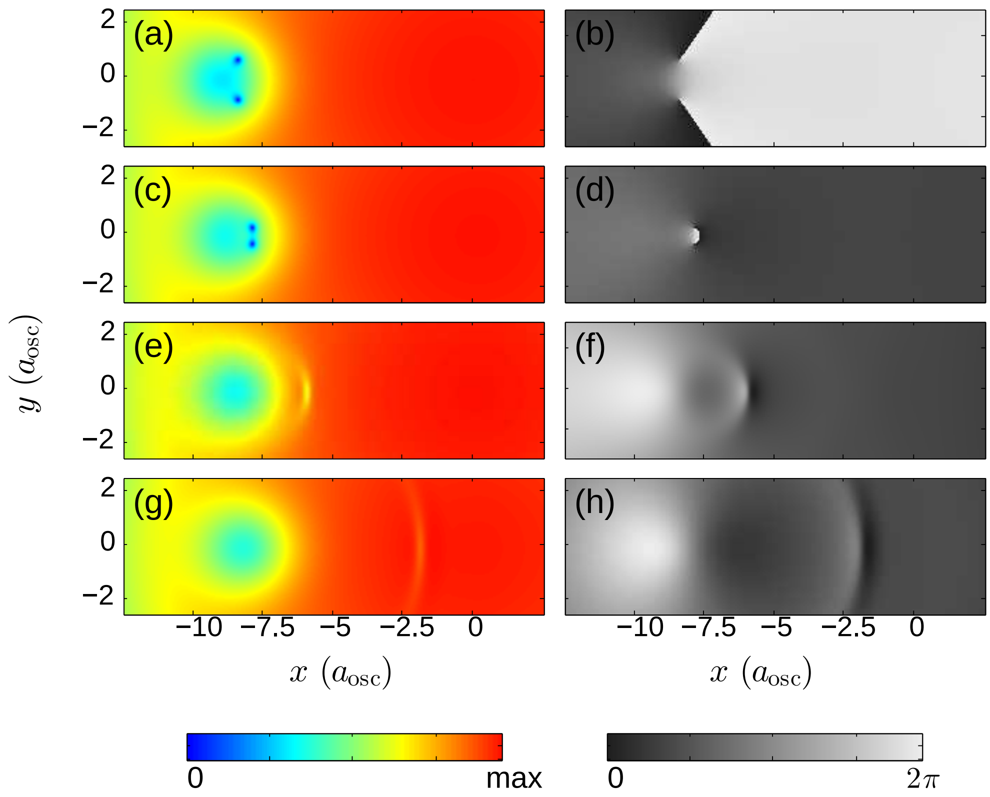

Figure 6.4: A vortex dipole is nucleated when the obstacle potential traverses the condensate at a speed of 120 μm s^{-1}. The vortex dipole, however, passes through and overtakes the obstacle. Later, as seen in (e), the vortex dipole annihilates and generates a gray soliton. The figures in the left panel show the density distribution and those on the right show the phase pattern of the condensate. From top to bottom, $t = 2.9$, 3.1, 3.3, and 3.5 respectively.

A reliable and qualitative way to describe occurrence of annihilation could be achieved by observing the density at the cores of vortex and antivortex which form the dipole. For the vortex, the matter density at the core when v is 120 μm s^{-1} is shown in Fig 6.5. In the plot, at time ≈ 3.19 (scaled unit), the core density starts increasing. This is because the core starts to fill in with the atoms from around the vortex after the annihilation. This filling process may not complete till it reaches the edge of the condensate and gets reflected inside the condensate.

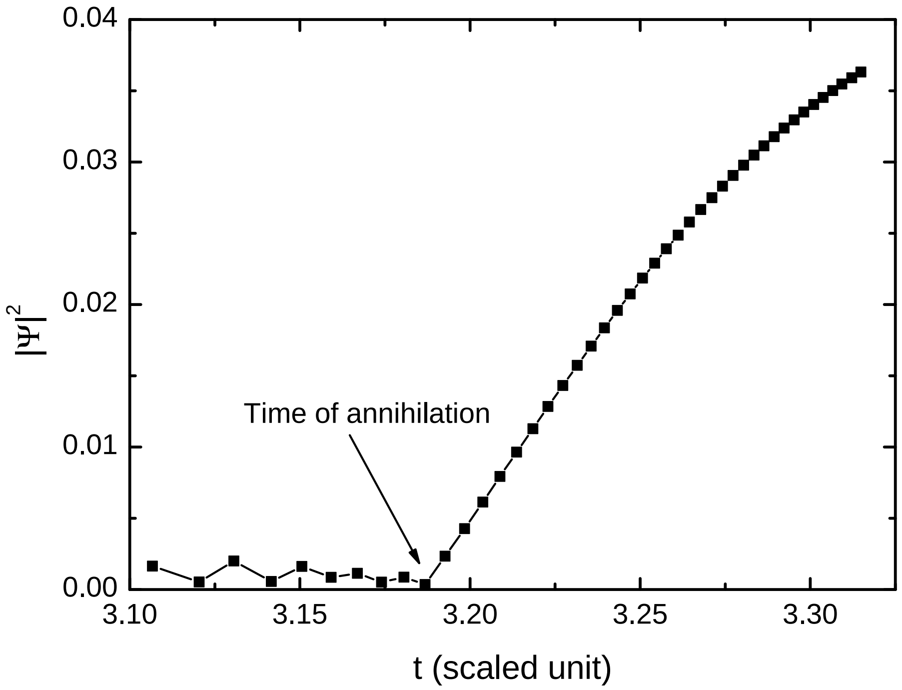

Figure 6.5: Density variation at the core of the vortex with time. After the vortex dipole annihilation, density increases till it reaches the bulk value. The values correspond to the obstacle speed of 120 μm s^{-1}. After annihilation, the number density has been considered from the location of minimum density. X-axis denotes the time elapsed from the starting of obstacle at $(-12.5a_{\rm osc}, 0)$.

After the annihilation of vortex-antivortex dipole pair, a gray soliton gets generated. We can clearly observe the propagation of this soliton in Fig. 6.6. The speed of propagation is 2000 μm s^{-1} which is similar to the speed of sound in condensate. During the propagation, the number density on the location of the soliton increases which is clearly visible from Fig. 6.6 as well as from Fig. 6.5. To estimate the energy of gray soliton, we have obtained the stationary state with the same position of vortex dipoles and obstacle potential. The energy difference between stationary state and dynamic state will provide us with the energy of gray soliton as discussed in ref [138]. The energy released due to the annihilation is 0.004 $\hbar\omega$ and is similar to the energy difference observed in Fig. 6.1, obtained from the TF approximation. We have also observed that this soliton gets reflected back-and-forth from the edge of the condensate. This reflection is similar to the reflection of any pulse from the circular edges.

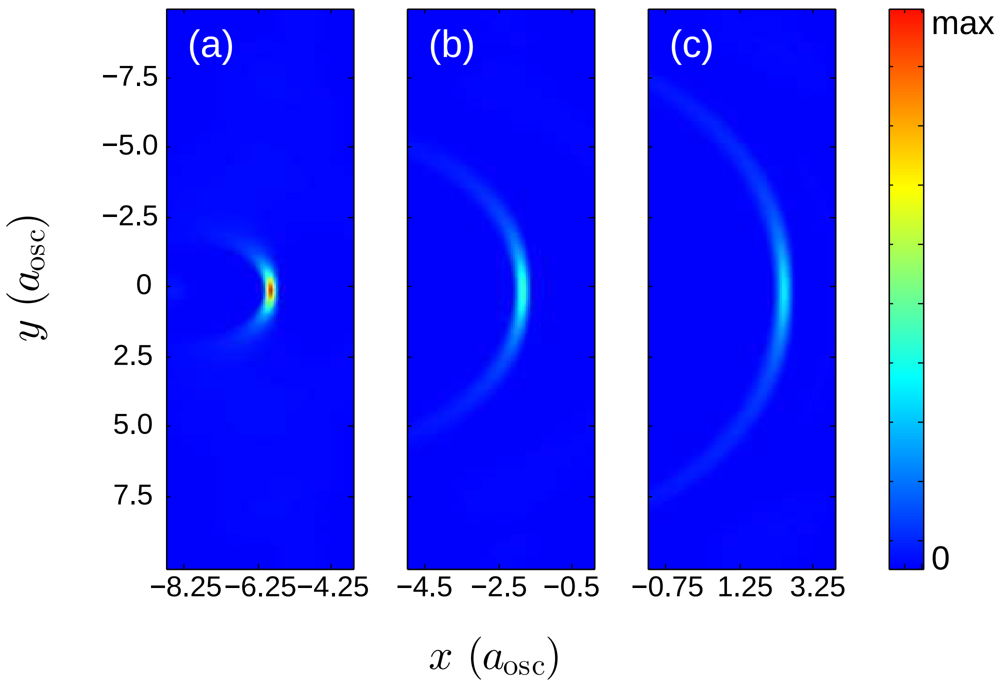

Figure 6.6: The propagation of the gray soliton after the annihilation of vortex dipole. The higher the value, higher the number density dip at that point. From (a)-(c), $t = 3.2$, 3.4 and 3.6 respectively.

It is to be mentioned that for the parameters considered in the present work, the speed of sound is 2190 μm s^{-1} and the coherence length of the system is ~ 0.229 μm. These are in agreement with the minimum separation between the vortex and antivortex observed in the analytical work. The energy gap for vortex dipole and gray soliton for the same size matches with the estimates from the ansatz based on TF approximation. The vortex dipole annihilation is not only observed for $V_{\rm obs} = 120$ μm s^{-1}, it also occurs for other obstacle velocities as well. Once such case, for $V_{\rm obs} = 160$ μm s^{-1}, is shown in Fig. 6.7. In this case, the difference in energy of vortex dipole and gray soliton is 0.0025 $\hbar\omega$.

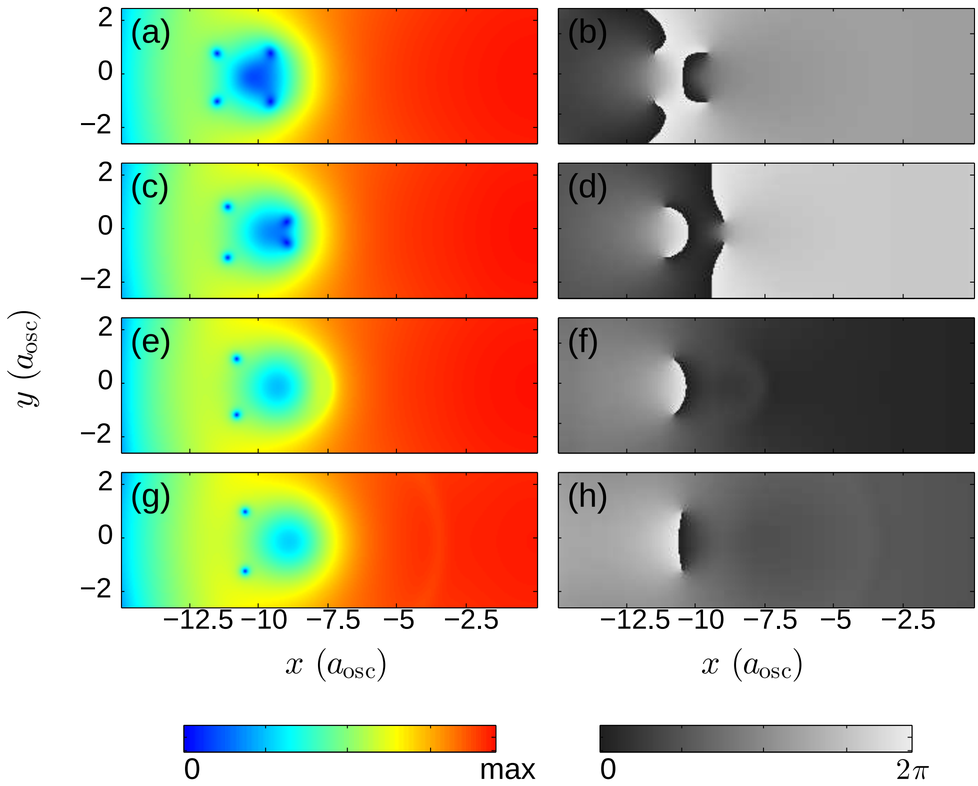

Figure 6.7: A vortex dipole is nucleated as the obstacle potential traverses the BEC with a speed of 160 μm s^{-1}. The figures in the left panel shows the density with time, where time progresses from top to bottom. Figures on the right panel show the phase pattern of the condensate. From top to bottom, $t = 1.6$, 1.8, 2.0, and 2.2 respectively.

One observation, which is common to all the vortex dipoles getting annihilated, is the nature of their trajectories. All of them traverse through $V_{\rm obs}$, whereas the ones which do not get annihilated avoid $V_{\rm obs}$. The vortex dipoles are generally nucleated at the aft region of the $V_{\rm obs}$ where there is a trailing superflow. When nucleated very close to each other ($v_2 < 0.5$) and with high velocity, the mutual force further increases the velocity of the vortex dipoles. At the same time, it decreases the distance separating vortex and antivortex. So, the kinetic energy is high enough to surpass $V_{\rm obs}$. Later, at some point vortex and antivortex separation is less than ξ, and they annihilate.

6.3.3 Effect of noise and dissipation

In the numerical studies, the annihilation events are not rare. But, this is in contradiction with the experimental results of Neely and collaborators [47]; they observed no signatures of annihilation events. One possible reason is that our numerical calculations are too ideal, and an immediate remedy is to include quantum and thermal fluctuations. The rigorous way to study these fluctuations is to use methods like Truncated Wigner approximation (TWA) [139, 140], however, in this work, we use the simple but widely accepted method of adding white noise [141, 142]. As white noise constitutes random fluctuations and hence it is able to change number density of the condensate. White noise is added numerically using random number generator. We have used Mersenne Twister pseudo random number generator. The strength of random noise used in our numerical calculation is 0.01% of maximum density of the condensate. This noise is added/subtracted at every time-step of the real-time evolution of the condensate. One immediate outcome is, the symmetry in the position of the vortex and antivortex is lost. The superflow around the vortex is no longer a mirror reflection of the antivortex, which was nearly the case without the white noise. The deviations are shown for an example case in Fig. 6.8, where $V_{\rm obs} = 180\ \mu{\rm m\ s}^{-1}$. This change in path leads to the suppression of annihilation events of vortex dipoles. We have also studied the effect of large white noise (10%) added in the beginning and not at latter time-step. In such cases, the noise gets damped throughout the condensate and consequently not able to show any change in the annihilation event.

The other important effect is the loss of atoms from the trap. We have examined the effect of loss terms, which arise from inelastic collisions in the condensate. There are two types of inelastic collisions that lead to the loss of atoms from the trap: two body inelastic collision loss and the three body loss. To model the effect of loss of atoms from the trap, we add the loss terms

$$\frac{-i\hbar}{2}\left[K_2|\Psi(\mathbf{r},t)|^2 + K_3|\Psi(\mathbf{r},t)|^4\right], \tag{6.33}$$

to the Hamiltonian $\mathcal{H}$. Based on the previous work [143] for ^{87}Rb, the inelastic two-body loss rate coefficient $K_2 = 4.5\times10^{-17}\ {\rm cm}^3\ {\rm s}^{-1}$, and inelastic three-body

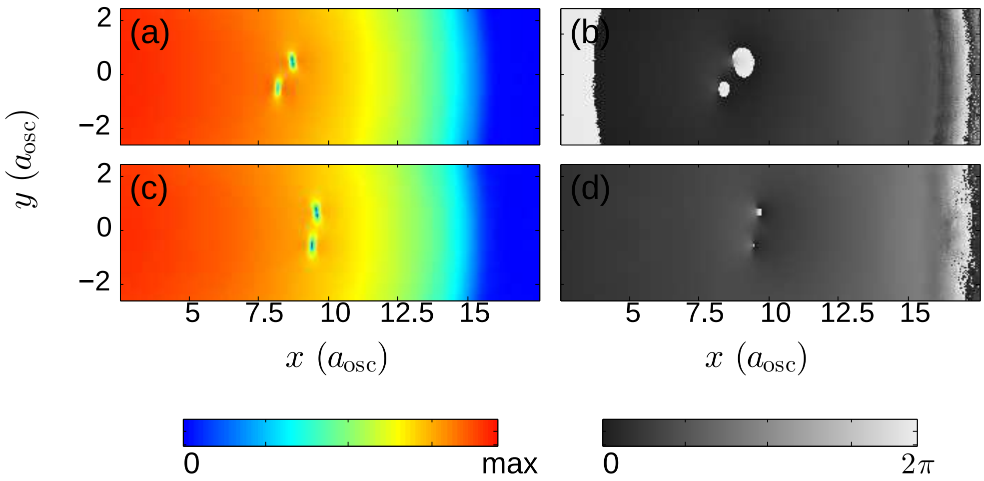

Figure 6.8: The figures in the left (right) panel show the density (phase) of the condensate in the presence of white noise at time $t = 4.1$ (top) and 4.2 (bottom). Lack in diametrical symmetry of the position of vortex dipole can be observed. This reduces the possibility of an annihilation event significantly. In this case, the speed of the obstacle is 180 μm s^{-1}.

loss rate coefficient $K_3 = 3.8 \times 10^{-29}$ cm^6 s^{-1}. With trap loss, the annihilation events continue to occur. However, during the time of flight observations in the experiments, the decreased atom numbers may lower the contrast and reduce the possibility of observing an annihilation event.

6.3.4 Optical vortex as obstacle to generate vortex dipole

When we consider optical vortex as obstacle, at the speed of 60 μm s^{-1}, one pair of dipole is generated. As the time progresses, the generated vortex dipole gets annihilated. One major outcome of using optical vortex as obstacle is that the dipoles are generated at very low speed of 60 μm s^{-1}. At this speed, no dipoles were getting generated in the case of Gaussian beam as obstacle. In this case, the critical velocity for obstacle is less than that of using Gaussian obstacle. The number density and phase profile for condensate with optical vortex obstacle at the speed of 60 μm s^{-1} is shown in Fig. 6.9.

As optical vortices are ring-shaped, these type of obstacles steer the conden-

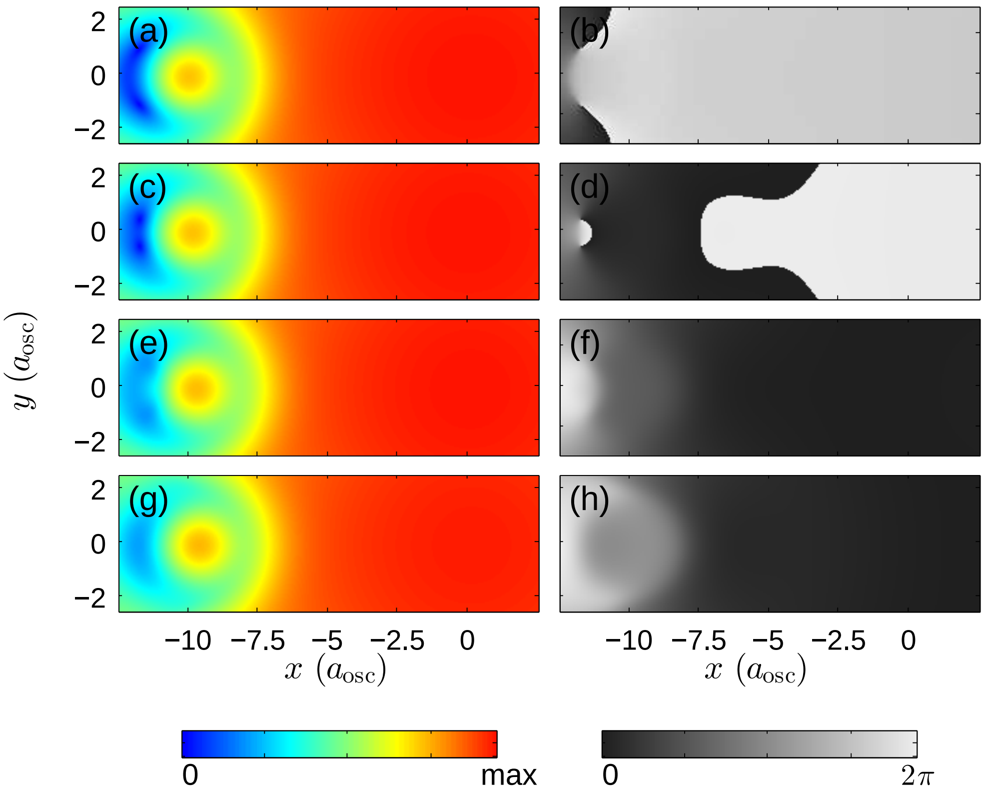

Figure 6.9: A pair of vortex dipoles are nucleated when optical vortex, as the obstacle, traverses the BEC with a speed of 60 μm s^{-1}. The figures in the left panel shows the density with time, where time progresses from top to bottom. Figures on the right panel show the phase pattern of the condensate. From top to bottom, t = 2.7, 2.9, 3.1, and 3.3 respectively.

sate more strongly than the Gaussian obstacle. This is one of the reasons for the decrease in critical velocity for the generation of vortices in the condensate.

6.4 Conclusion

When an obstacle moves through a condensate above a critical speed, it nucleates vortex dipoles and the number of dipoles seeded depends on the obstacle velocity. Depending on the initial condition of nucleation, vortex and antivortex annihilation events occur under ideal conditions: at zero temperature, no loss, and without noise. These events are found to be energetically favorable theoretically and observed numerically. In the case of weakly interacting condensates, the energy of gray soliton is always less than that of vortex dipole and provides higher possibility for annihilation events. Similarly, in the case of strongly interacting condensates, we use TF approximation to study the system and find that if the separation between the vortex anti-vortex pair is less than the coherence length, the energy of vortex dipole is more than that of gray soliton and this leads to annihilation. The generated gray soliton propagates through the condensate and shows the phenomena of reflection from the circular edge of the condensate. The speed of propagation is found to be similar to the speed of sound in BEC. However, noise, thermal fluctuations and dissipation destroy superflow reflection symmetry around the vortex and antivortex. Breaking the symmetry reduces the possibility of annihilation events and may explain the lack of annihilation events in experimental observations.

Chapter 7

Summary and Scope for Future Work

This thesis deals with the study of interaction of optical vortices with matter. For this dissertation, the chosen systems are non-linear crystal β-Barium Borate (BBO) and Bose-Einstein condensates (BEC). The optical vortices are generated using computer-generated holography technique. A new method for characterization of optical vortex from just the intensity distribution of a vortex has been proposed and verified experimentally. We have shown that the number of dark rings in the Fourier transform (FT) of the intensity is the order of vortex. We have studied the non-linear interaction of optical vortices with BBO crystal. The SPDC ring due to optical vortex forms two concentric bright rings with an intensity minimum in the middle. We have also experimentally verified the quantum inspired optical entanglement of classical optical vortex beams. The extent of violation of Bell's inequality increases with the increase in their topological charge. Quantum elliptic vortex (QEV) state can be generated in idler beam by using beam-splitters in signal beam of SPDC process. We have studied the entanglement and its control for these quantum optical vortices using Wigner distribution function (WDF).

Next, we have taken BEC and studied the annihilation of vortex dipoles formed in the BEC. It is observed that the vortex dipole annihilation is critically dependent on the initial conditions for their nucleation. The noise in the system destroys the symmetry in the position of the vortex and antivortex and consequently, the annihilation events are also suppressed. In case of optical vortex as obstacle, as optical vortices are ring-shaped, these type of obstacles steer the condensate more strongly than the Gaussian obstacle. This is one of the reason for the decrease in critical velocity for the generation of vortices in the condensate.

7.1 Summary of work-done

Chapter 1 gives the elementary background for the work presented in this thesis. We have briefly described the optical vortices and orbital angular momentum in this chapter. We have also described the process of SPDC and shown the SPDC rings generated by type-I and type-II SPDC process. The process of SPDC generates entanglement in the down-converted photons. The propagation of optical vortex and vortex dipole in free space has also discussed. We have also briefly described the theory of Bose-Einstein condensate and dynamics of vortex dipoles in these condensates.

In Chapter 2, we have discussed generation and characterization of optical vortex beams. The computer generated holography technique has been introduced briefly with explanation of different types of holograms. The steps of computer-generated holography are presented in this chapter. The working principle of the SLM has been highlighted. We have briefly described the generation of optical vortices using spiral phase plate. In this chapter, we have proposed new techniques for the measurement of OAM or topological charge of the vortex. We have outlined a simple technique to determine the order of a vortex based on the FT of its intensity profile and the orthogonality of the Laguerre polynomials. This method is effective in determining the order of the higher charged vortex also.

Chapter 3 describes the spatial distribution of entangled photons generated by pumping the non-linear crystal with the Gaussian as well as optical vortex beams. We have observed a linear increase in thickness of the SPDC ring with beam radius of the Gaussian pump. We have also observed the formation of two concentric SPDC rings if the crystal is pumped with optical vortex beams. One of the reasons for generation of two rings is the dark core of optical vortex i.e. unique intensity distribution of the vortex. The formation of two rings takes place when the pump beam size is more than the critical beam size. These observations would be useful in the experiments to maximize the coincidence counts while working with entangled OAM states of the photons.

Chapter 4 describes the experimental verification of quantum inspired optical entanglement of classical optical vortex beams. We have found that these classical beams violate Bell's inequality for continuous variable written in terms of the WDF. The extent of violation of Bell's inequality increases with the increase in its topological charge. To obtain this, we have used the FT of two-point correlation function that provides us WDF of such beams.

In Chapter 5, we proposed the mechanism to generate a QEV state and studied their entanglement using the logarithmic negativity of the lowest eigenvalue of the covariance matrix for the QEV. The four-dimensional WDF was used to find out covariance matrix and therefore, the logarithmic negativity. We have shown that by changing the squeezing parameter one can control the entanglement. We have also observed a critical point above which the increase in vorticity decreases the entanglement.

Chapter 6 is devoted towards the annihilation of vortex dipoles in Bose-Einstein condensates. These dipoles are created by moving an obstacle, a Gaussian or a vortex beam of light, through a condensate above a critical speed. Depending on the initial condition of nucleation, vortex and antivortex gets annihilated. In case of optical vortex as obstacle, the critical velocity for the generation of vortex dipoles is less than that of Gaussian obstacle. In the case of weakly interacting condensates, the energy of gray soliton is always less than that of vortex dipole and hence supports annihilation events. Similarly, in the case of strongly interacting condensates, we use TF approximation to study the system and found that if the separation between the vortex anti-vortex pair is less then the coherence length, the energy of vortex dipole is more than that of gray soliton and this leads to annihilation. However, noise, thermal fluctuations and dissipation destroy the superflow reflection symmetry around the vortex and antivortex.

7.2 Scope for future work

We have verified experimentally that the photon coming out of laser follows Poissonian probability distribution. We have studied this by using both single photon counting modules (SPCM) as well as EMCCD. As the process of SPDC generates two photons from one photon of the pump, we would like to study the photon number probability distribution of down-converted photons. The study of photon statistics may find application in quantum optics and quantum information.

During the course of our study, we have found that the constrained optimization algorithm can be used for accurate phase measurement even at the very low light levels. We plan to use this technique for measuring the down-converted optical vortex states which find use in quantum information and computation.

In this thesis work, we have used Gaussian beam as obstacle while studying the dynamics of the condensate. We have found that the generated vortex dipoles gets annihilated during the time-evolution of the condensate. In our preliminary studies, we have observed that while using optical vortex as obstacle, the critical velocity for the nucleation of vortex dipoles decreases. We would like to study the effect on annihilation events due to the vortex obstacle numerically as well as analytically. We also wish to study effect of quantum turbulence on the annihilation events of vortex dipoles.

Recently, we are involved with generation of radially and azimuthally polarized beams to study the non-separability of polarization and spatial modes of light. These results may boost the application of the optical vortex beams as information carriers.

Bibliography

[1] T. Young, *The bakerian lecture: Experiments and calculations relative to physical optics,* Philosophical Transactions of the Royal Society of London **94**, 1–16 (1804).

[2] M. Beijersbergen, L. Allen, H. van der Veen, and J. Woerdman, *Astigmatic laser mode converters and transfer of orbital angular momentum,* Optics Communications **96**, 123–132 (1993).

[3] E. Wolf, *Progress in optics. Volume 39* (Elsevier, Amsterdam; New York, 1999).

[4] J. F. Nye and M. V. Berry, *Dislocations in wave trains,* Proceedings of the Royal Society of London. A. Mathematical and Physical Sciences **336**, 165–190 (1974).

[5] I. Basistiy, V. Bazhenov, M. Soskin, and M. Vasnetsov, *Optics of light beams with screw dislocations,* Optics Communications **103**, 422–428 (1993).

[6] L. Allen, M. Beijersbergen, R. Spreeuw, and J. Woerdman, *Orbital angular momentum of light and the transformation of Laguerre-Gaussian laser modes,* Physical Review A **45**, 8185–8189 (1992).

[7] M. V. Berry, *Disruption of wavefronts: statistics of dislocations in incoherent gaussian random waves,* Journal of Physics A: Mathematical and General **11**, 27–37 (1978).

[8] R. P. Singh, A. Kuar, and J. Bhatt, *Vortices of Light: Generation, Characterization and Applications* (Nova Science Pub, New York, 2008).

[9] J. Leach, M. R. Dennis, J. Courtial, and M. J. Padgett, *Laser beams: Knotted threads of darkness,* Nature **432**, 165–165 (2004).

[10] D. G. Grier, *A revolution in optical manipulation,* Nature **424**, 810–816 (2003).

[11] T. Kuga, Y. Torii, N. Shiokawa, T. Hirano, Y. Shimizu, and H. Sasada, *Novel optical trap of atoms with a doughnut beam,* Physical Review Letters **78**, 4713–4716 (1997).

[12] G. Molina-Terriza, J. P. Torres, and L. Torner, *Twisted photons,* Nature Physics **3**, 305–310 (2007).

[13] T. Brunet, J. Thomas, and R. Marchiano, *Transverse shift of helical beams and subdiffraction imaging,* Physical Review Letters **105**, 034301 (2010).

[14] A. Mair, A. Vaziri, G. Weihs, and A. Zeilinger, *Entanglement of the orbital angular momentum states of photons,* Nature **412**, 313–316 (2001).

[15] C. V. Raman and S. Bhagavantam, *Experimental proof of the spin of the photon.* Nature **129**, 22–23 (1932).

[16] L. Allen, M. J. Padgett, and M. Babiker, *The orbital angular momentum of light,* in "Progress in Optics," , vol. 39, E. Wolf, ed. (Elsevier, 1999), pp. 291–372.

[17] A. T. O'Neil, I. MacVicar, L. Allen, and M. J. Padgett, *Intrinsic and extrinsic nature of the orbital angular momentum of a light beam,* Physical Review Letters **88**, 053601 (2002).

[18] R. W. Boyd, *Nonlinear optics* (Academic Press, San Diego, CA, 2003), 3rd ed.

[19] C. Hong and L. Mandel, *Theory of parametric frequency down conversion of light,* Physical Review A **31**, 2409–2418 (1985).

[20] D. Burnham and D. Weinberg, *Observation of simultaneity in parametric production of optical photon pairs,* Physical Review Letters **25**, 84–87 (1970).

[21] L. Zhang, A. B. U'ren, R. Erdmann, K. A. O'Donnell, C. Silberhorn, K. Banaszek, and I. A. Walmsley, *Generation of highly entangled photon pairs for continuous variable bell inequality violation,* Journal of Modern Optics **54**, 707–719 (2007).

[22] P. Kok, K. Nemoto, T. C. Ralph, J. P. Dowling, and G. J. Milburn, *Linear optical quantum computing with photonic qubits,* Reviews of Modern Physics **79**, 135–174 (2007).

[23] W. H. Louisell, A. Yariv, and A. E. Siegman, *Quantum fluctuations and noise in parametric processes. I.* Physical Review **124**, 1646–1654 (1961).

[24] J. P. Gordon, W. H. Louisell, and L. R. Walker, *Quantum fluctuations and noise in parametric processes. II,* Physical Review **129**, 481–485 (1963).

[25] A. Ling, A. Lamas-Linares, and C. Kurtsiefer, *Absolute emission rates of spontaneous parametric down-conversion into single transverse Gaussian modes,* Physical Review A **77**, 043834 (2008).

[26] M. Rubin, *Transverse correlation in optical spontaneous parametric down-conversion,* Physical Review A **54**, 5349–5360 (1996).

[27] H. Di Lorenzo Pires, F. M. G. J. Coppens, and M. P. van Exter, *Type-I spontaneous parametric down-conversion with a strongly focused pump,* Physical Review A **83**, 033837 (2011).

[28] L.-A. Wu, H. J. Kimble, J. L. Hall, and H. Wu, *Generation of squeezed states by parametric down conversion,* Physical Review Letters **57**, 2520–2523 (1986).

[29] Y.-H. Kim, *Quantum interference with beamlike type-II spontaneous parametric down-conversion,* Physical Review A **68**, 013804 (2003).

[30] Y.-H. Kim and W. P. Grice, *Measurement of the spectral properties of the two-photon state generated via type-II spontaneous parametric downconversion,* Optics Letters **30**, 908 (2005).

[31] A. Bandyopadhyay and R. P. Singh, *Wigner distribution of elliptical quantum optical vortex,* Optics Communications **284**, 256–261 (2011).

[32] G. Agarwal, R. Puri, and R. Singh, *Vortex states for the quantized radiation field,* Physical Review A **56**, 4207–4215 (1997).

[33] M. J. Bastiaans, *The Wigner distribution function applied to optical signals and systems,* Optics Communications **25**, 26–30 (1978).

[34] R. P. Singh and S. R. Chowdhury, *Trajectory of an optical vortex: canonical vs. non-canonical,* Optics Communications **215**, 231–237 (2003).

[35] V. Bazhenov, M. Soskin, and M. Vasnetsov, *Screw dislocations in light wavefronts,* Journal of Modern Optics **39**, 985–990 (1992).

[36] G. Indebetouw, *Optical vortices and their propagation,* Journal of Modern Optics **40**, 73–87 (1993).

[37] F. S. Roux, *Spatial evolution of the morphology of an optical vortex dipole,* Optics Communications **236**, 433–440 (2004).

[38] F. S. Roux, *Canonical vortex dipole dynamics,* Journal of the Optical Society of America B **21**, 655–663 (2004).

[39] M. Chen and F. S. Roux, *Accelerating the annihilation of an optical vortex dipole in a Gaussian beam,* Journal of the Optical Society of America A **25**, 1279 (2008).

[40] Z. Chen, J. Pu, and D. Zhao, *Tight focusing properties of linearly polarized Gaussian beam with a pair of vortices,* Physics Letters A **375**, 2958–2963 (2011).

[41] H. Chen, Z. Gao, H. Yang, F. Wang, and X. Huang, *Propagation of a pair of vortices through a tilted lens,* Optik - International Journal for Light and Electron Optics **124**, 4201–4205 (2013).

[42] C. Pethick and H. Smith, *Bose-Einstein condensation in dilute gases* (Cambridge University Press, Cambridge; New York, 2008), 2nd ed.

[43] L. Landau, *Theory of the superfluidity of Helium II,* Physical Review **60**, 356–358 (1941).

[44] M. Greiner, O. Mandel, T. Esslinger, T. W. Hänsch, and I. Bloch, *Quantum phase transition from a superfluid to a mott insulator in a gas of ultracold atoms,* Nature **415**, 39–44 (2002).

[45] J. R. Anglin and W. Ketterle, *Bose-Einstein condensation of atomic gases,* Nature **416**, 211–218 (2002).

[46] M. Matthews, B. Anderson, P. Haljan, D. Hall, C. Wieman, and E. Cornell, *Vortices in a Bose-Einstein condensate,* Physical Review Letters **83**, 2498–2501 (1999).

[47] T. W. Neely, E. C. Samson, A. S. Bradley, M. J. Davis, and B. P. Anderson, *Observation of vortex dipoles in an oblate Bose-Einstein condensate,* Physical Review Letters **104**, 160401 (2010).

[48] D. V. Freilich, D. M. Bianchi, A. M. Kaufman, T. K. Langin, and D. S. Hall, *Real-time dynamics of single vortex lines and vortex dipoles in a Bose-Einstein condensate,* Science **329**, 1182–1185 (2010).

[49] G. Andrelczyk, M. Brewczyk, ł. Dobrek, M. Gajda, and M. Lewenstein, *Optical generation of vortices in trapped Bose-Einstein condensates,* Physical Review A **64**, 043601 (2001).

[50] J. Brand and W. Reinhardt, *Solitonic vortices and the fundamental modes of the "snake instability": Possibility of observation in the gaseous Bose-Einstein condensate,* Physical Review A **65**, 043612 (2002).

[51] S. Middelkamp, P. J. Torres, P. G. Kevrekidis, D. J. Frantzeskakis, R. Carretero-Gonzlez, P. Schmelcher, D. V. Freilich, and D. S. Hall, *Guiding-center dynamics of vortex dipoles in Bose-Einstein condensates,* Physical Review A **84**, 011605 (2011).

[52] T. Aioi, T. Kadokura, T. Kishimoto, and H. Saito, *Controlled generation and manipulation of vortex dipoles in a Bose-Einstein condensate,* Physical Review X **1**, 021003 (2011).

[53] Y. Couder and C. Basdevant, *Experimental and numerical study of vortex couples in two-dimensional flows,* Journal of Fluid Mechanics **173**, 225 (2006).

[54] A. Fetter, *Rotating trapped Bose-Einstein condensates,* Reviews of Modern Physics **81**, 647–691 (2009).

[55] E. Sonin, *Vortex oscillations and hydrodynamics of rotating superfluids,* Reviews of Modern Physics **59**, 87–155 (1987).

[56] S. V. Alekseenko, P. A. Kuibin, and V. L. Okulov, *Theory of concentrated vortices: an introduction* (Springer, Berlin; New York, 2007).

[57] B. Jackson, J. McCann, and C. Adams, *Vortex line and ring dynamics in trapped Bose-Einstein condensates,* Physical Review A **61**, 013604 (1999).

[58] W. Li, M. Haque, and S. Komineas, *Vortex dipole in a trapped two-dimensional Bose-Einstein condensate,* Physical Review A **77**, 053610 (2008).

[59] M. W. Beijersbergen, R. P. C. Coerwinkel, M. Kristensen, and J. P. Woerdman, *Helical-wavefront laser beams produced with a spiral phaseplate,* Optics Communications **112**, 321–327 (1994).

[60] V. Y. Bazhenov, M. V. Vasnetsov, and M. S. Soskin, *Laser beams with screw dislocations in their wavefronts,* Journal of Experimental and Theoretical Physics **52**, 429 (1990).

[61] N. R. Heckenberg, R. McDuff, C. P. Smith, and A. G. White, *Generation of optical phase singularities by computer-generated holograms,* Optics Letters **17**, 221–223 (1992).

[62] N. R. Heckenberg, R. McDuff, C. P. Smith, H. Rubinsztein-Dunlop, and M. J. Wegener, *Laser beams with phase singularities,* Optical and Quantum Electronics **24**, S951–S962 (1992).

[63] J. E. Curtis, B. A. Koss, and D. G. Grier, *Dynamic holographic optical tweezers,* Optics Communications **207**, 169–175 (2002).

[64] A. V. Carpentier, H. Michinel, J. R. Salgueiro, and D. Olivieri, *Making optical vortices with computer-generated holograms,* American Journal of Physics **76**, 916 (2008).

[65] D. P. Ghai, S. Vyas, P. Senthilkumaran, and R. S. Sirohi, *Detection of phase singularity using a lateral shear interferometer,* Optics and Lasers in Engineering **46**, 419–423 (2008).

[66] H. I. Sztul and R. R. Alfano, *Double-slit interference with Laguerre-Gaussian beams,* Optics Letters **31**, 999–1001 (2006).

[67] E. Fraczek, W. Fraczek, and J. Masajada, *The new method of topological charge determination of optical vortices in the interference field of the optical vortex interferometer,* Optik - International Journal for Light and Electron Optics **117**, 423–425 (2006).

[68] J. Arlt, K. Dholakia, L. Allen, and M. J. Padgett, *The production of multiringed Laguerre-Gaussian modes by computer-generated holograms,* Journal of Modern Optics **45**, 1231–1237 (1998).

[69] A. Kumar, S. Prabhakar, P. Vaity, and R. P. Singh, *Information content of optical vortex fields,* Optics Letters **36**, 1161 (2011).

[70] C.-S. Guo, L.-L. Lu, and H.-T. Wang, *Characterizing topological charge of optical vortices by using an annular aperture,* Optics Letters **34**, 3686 (2009).

[71] D. P. Ghai, P. Senthilkumaran, and R. S. Sirohi, *Single-slit diffraction of an optical beam with phase singularity,* Optics and Lasers in Engineering **47**, 123–126 (2009).

[72] L. Yongxin, T. Hua, P. Jixiong, and L. Baida, *Detecting the topological charge of vortex beams using an annular triangle aperture,* Optics & Laser Technology **43**, 1233–1236 (2011).

[73] I. Moreno, J. A. Davis, B. M. Pascoguin, M. J. Mitry, and D. M. Cottrell, *Vortex sensing diffraction gratings,* Optics Letters **34**, 2927 (2009).

[74] L. E. E. de Araujo and M. E. Anderson, *Measuring vortex charge with a triangular aperture,* Optics Letters **36**, 787 (2011).

[75] J. Curtis and D. Grier, *Structure of optical vortices,* Physical Review Letters **90**, 133901 (2003).

[76] A. Kumar, P. Vaity, Y. Krishna, and R. Singh, *Engineering the size of dark core of an optical vortex,* Optics and Lasers in Engineering **48**, 276–281 (2010).

[77] I. S. Gradshtein, I. M. Ryzhik, A. Jeffrey, and D. Zwillinger, *Table of integrals, series and products* (Academic, Oxford, 2007).

[78] G. Agarwal and R. Singh, *Complementarity and phase distributions for angular momentum systems,* Physics Letters A **217**, 215–218 (1996).

[79] D. F. V. James, H. C. Kandpal, and E. Wolf, *A new method for determining the angular separation of double stars,* The Astrophysical Journal **445**, 406 (1995).

[80] M. Edgar, D. Tasca, F. Izdebski, R. Warburton, J. Leach, M. Agnew, G. Buller, R. Boyd, and M. Padgett, *Imaging high-dimensional spatial entanglement with a camera,* Nature Communications **3**, 984 (2012).

[81] C. Law and J. Eberly, *Analysis and interpretation of high transverse entanglement in optical parametric down conversion,* Physical Review Letters **92**, 127903 (2004).

[82] J. C. Howell, R. S. Bennink, S. J. Bentley, and R. W. Boyd, *Realization of the Einstein-Podolsky-Rosen paradox using momentum- and position-entangled photons from spontaneous parametric down conversion,* Physical Review Letters **92**, 210403 (2004).

[83] P. Kwiat, K. Mattle, H. Weinfurter, A. Zeilinger, A. Sergienko, and Y. Shih, *New high-intensity source of polarization-entangled photon pairs,* Physical Review Letters **75**, 4337–4341 (1995).

[84] C. Simon and J.-P. Poizat, *Creating single time-bin-entangled photon pairs,* Physical Review Letters **94**, 030502 (2005).

[85] R. Ramírez-Alarcón, H. Cruz-Ramírez, and A. B. URen, *Effects of crystal length on the angular spectrum of spontaneous parametric downconversion photon pairs,* Laser Physics **23**, 055204 (2013).

[86] T. Grayson and G. Barbosa, *Spatial properties of spontaneous parametric down-conversion and their effect on induced coherence without induced emission,* Physical Review A **49**, 2948–2961 (1994).

[87] H. Cruz-Ramírez, R. Ramírez-Alarcón, F. J. Morelos, P. A. Quinto-Su, J. C. Gutiérrez-Vega, and A. B. URen, *Observation of non-diffracting behavior at the single-photon level,* Optics Express **20**, 29761 (2012).

[88] T. Pittman, D. Strekalov, D. Klyshko, M. Rubin, A. Sergienko, and Y. Shih, *Two-photon geometric optics,* Physical Review A **53**, 2804–2815 (1996).

[89] R. Fickler, M. Krenn, R. Lapkiewicz, S. Ramelow, and A. Zeilinger, *Real-time imaging of quantum entanglement,* Scientific Reports **3**, 1914 (2013).

[90] O. Bryngdahl, *Formation of blazed gratings,* Journal of the Optical Society of America **60**, 140_1 (1970).

[91] P. S. K. Lee, M. P. van Exter, and J. P. Woerdman, *How focused pumping affects type-II spontaneous parametric down-conversion,* Physical Review A **72**, 033803 (2005).

[92] A. Einstein, B. Podolsky, and N. Rosen, *Can Quantum-Mechanical description of physical reality be considered complete?* Physical Review **47**, 777–780 (1935).

[93] J. S. Bell, *On the Einstein-Podolsky-Rosen paradox,* Physics **1**, 195–200 (1964).

[94] A. Aspect, P. Grangier, and G. Roger, *Experimental realization of Einstein-Podolsky-Rosen-Bohm gedankenexperiment: A new violation of Bell's inequalities,* Physical Review Letters **49**, 91–94 (1982).

[95] J. S. Ivan, S. Chaturvedi, E. Ercolessi, G. Marmo, G. Morandi, N. Mukunda, and R. Simon, *Entanglement and nonclassicality for multimode radiation-field states,* Physical Review A **83**, 032118 (2011).

[96] R. Pratap Singh, S. Roychowdhury, and V. Kumar Jaiswal, *Wigner distribution of an optical vortex,* Journal of Modern Optics **53**, 1803–1808 (2006).

[97] P. Chowdhury, A. S. Majumdar, and G. S. Agarwal, *Nonlocal continuous-variable correlations and violation of Bell's inequality for light beams with topological singularities,* Physical Review A **88**, 013830 (2013).

[98] K. H. Kagalwala, G. Di Giuseppe, A. F. Abouraddy, and B. E. A. Saleh, *Bell's measure in classical optical coherence,* Nature Photonics **7**, 72–78 (2012).

[99] C. V. S. Borges, M. Hor-Meyll, J. A. O. Huguenin, and A. Z. Khoury, *Bell-like inequality for the spin-orbit separability of a laser beam,* Physical Review A **82**, 033833 (2010).

[100] C. Iaconis and I. A. Walmsley, *Direct measurement of the two-point field correlation function,* Optics Letters **21**, 1783 (1996).

[101] C.-C. Cheng, M. G. Raymer, and H. Heier, *A variable lateral-shearing sagnac interferometer with high numerical aperture for measuring the com-*

plex spatial coherence function of light, Journal of Modern Optics **47**, 1237–1246 (2000).

[102] R. Simon and G. S. Agarwal, *Wigner representation of Laguerre-Gaussian beams,* Optics Letters **25**, 1313 (2000).

[103] J. Clauser, M. Horne, A. Shimony, and R. Holt, *Proposed experiment to test local hidden-variable theories,* Physical Review Letters **23**, 880–884 (1969).

[104] K. Banaszek and K. Wódkiewicz, *Direct probing of quantum phase space by photon counting,* Physical Review Letters **76**, 4344–4347 (1996).

[105] K. Banaszek and K. Wódkiewicz, *Nonlocality of the Einstein-Podolsky-Rosen state in the wigner representation,* Physical Review A **58**, 4345–4347 (1998).

[106] A. Kumar, J. Banerji, and R. P. Singh, *Hanbury browntwiss-type experiments with optical vortices and observation of modulated intensity correlation on scattering from rotating ground glass,* Physical Review A **86**, 013825 (2012).

[107] G. S. Agarwal and J. Banerji, *Entanglement by linear SU(2) transformations: generation and evolution of quantum vortex states,* Journal of Physics A: Mathematical and General **39**, 11503 (2006).

[108] B. C. Sanders, *Entangled coherent states,* Physical Review A **45**, 6811–6815 (1992).

[109] B. C. Sanders, K. S. Lee, and M. S. Kim, *Optical homodyne measurements and entangled coherent states,* Physical Review A **52**, 735–741 (1995).

[110] M. G. A. Paris, *Entanglement and visibility at the output of a mach-zehnder interferometer,* Physical Review A **59**, 1615–1621 (1999).

[111] M. S. Kim, W. Son, V. Buek, and P. L. Knight, *Entanglement by a beam splitter: Nonclassicality as a prerequisite for entanglement,* Physical Review A **65**, 032323 (2002).

[112] V. Parigi, A. Zavatta, M. Kim, and M. Bellini, *Probing quantum commutation rules by addition and subtraction of single photons to/from a light field,* Science **317**, 1890–1893 (2007).

[113] E. Wigner, *On the quantum correction for thermodynamic equilibrium,* Physical Review **40**, 749–759 (1932).

[114] E. C. G. Sudarshan, *Equivalence of semiclassical and quantum mechanical descriptions of statistical light beams,* Physical Review Letters **10**, 277–279 (1963).

[115] R. Glauber, *Coherent and incoherent states of the radiation field,* Physical Review **131**, 2766–2788 (1963).

[116] R. P. Singh, S. Roychowdhury, and V. K. Jaiswal, *Non-axial nature of an optical vortex and Wigner function,* Optics Communications **274**, 281–285 (2007).

[117] L. Allen, S. M. Barnett, and M. J. Padgett, *Optical angular momentum* (Institute of Physics Pub, Bristol; Philadelphia, 2003).

[118] M. G. Genoni and M. G. A. Paris, *Quantifying non-Gaussianity for quantum information,* Physical Review A **82**, 052341 (2010).

[119] A. Rai, S. Das, and G. S. Agarwal, *Non-Gaussian and Gaussian entanglement in coupled leaky waveguides,* arXiv:0907.2432 (2009).

[120] A. Bandyopadhyay and J. Rai, *Uncertainties of schwinger angular-momentum operators for squeezed radiation in interferometers,* Physical Review A **51**, 1597–1603 (1995).

[121] K. Staliunas, *Dynamics of optical vortices in a laser beam,* Optics Communications **90**, 123–127 (1992).

[122] I. Freund, *Optical vortex trajectories,* Optics Communications **181**, 19–33 (2000).

[123] A. V. Mamaev, M. Saffman, and A. A. Zozulya, *Propagation of a mutually incoherent optical vortex pair in anisotropic nonlinear media,* Journal of Optics B: Quantum Semiclassical Optics **6**, S318 (2004).

[124] S. G. Reddy, S. Prabhakar, A. Aadhi, J. Banerji, and R. P. Singh, *Propagation of an arbitrary vortex pair through an astigmatic optical system and determination of its topological charge,* Journal of the Optical Society of America A **31**, 1295–1302 (2014).

[125] I. Velchev, A. Dreischuh, D. Neshev, and S. Dinev, *Interactions of optical vortex solitons superimposed on different background beams,* Optics Communications **130**, 385–392 (1996).

[126] Y. S. Kivshar, J. Christou, V. Tikhonenko, B. Luther-Davies, and L. M. Pismen, *Dynamics of optical vortex solitons,* Optics Communications **152**, 198–206 (1998).

[127] S. Nazarenko and M. Onorato, *Freely decaying turbulence and Bose-Einstein condensation in gross-pitaevski model,* Journal of Low Temperature Physics **146**, 31–46 (2006).

[128] S. J. Rooney, P. B. Blakie, B. P. Anderson, and A. S. Bradley, *Suppression of kelvon-induced decay of quantized vortices in oblate Bose-Einstein condensates,* Physical Review A **84**, 023637 (2011).

[129] B. Nowak, D. Sexty, and T. Gasenzer, *Superfluid turbulence: Nonthermal fixed point in an ultracold bose gas,* Physical Review B **84**, 020506 (2011).

[130] R. Dum, J. Cirac, M. Lewenstein, and P. Zoller, *Creation of dark solitons and vortices in Bose-Einstein condensates,* Physical Review Letters **80**, 2972–2975 (1998).

[131] K.-P. Marzlin, W. Zhang, and E. Wright, *Vortex coupler for atomic Bose-Einstein condensates,* Physical Review Letters **79**, 4728–4731 (1997).

[132] K. Staliunas, *Vortex creation in Bose-Einstein condensates by laser-beam vortex guiding,* Applied Physics B: Lasers and Optics **71**, 555–559 (2000).

[133] P. Kuopanportti, J. A. M. Huhtamäki, and M. Möttönen, *Size and dynamics of vortex dipoles in dilute Bose-Einstein condensates,* Physical Review A **83**, 011603(R) (2011).

[134] E. G. M. van Kempen, S. J. J. M. F. Kokkelmans, D. J. Heinzen, and B. J. Verhaar, *Interisotope determination of ultracold rubidium interactions from three high-precision experiments,* Physical Review Letters **88**, 093201 (2002).

[135] P. Muruganandam and S. Adhikari, *Fortran programs for the time-dependent gross-pitaevskii equation in a fully anisotropic trap,* Computer Physics Communications **180**, 1888–1912 (2009).

[136] Q. Zhou and H. Zhai, *Vortex dipole in a trapped atomic Bose-Einstein condensate,* Physical Review A **70**, 043619 (2004).

[137] L. D. Landau, L. D. Landau, and L. D. Landau, *Statistical physics, Part 2* (Pergamon Press, Oxford; New York, 1980).

[138] N. Parker and C. Adams, *Emergence and decay of turbulence in stirred atomic Bose-Einstein condensates,* Physical Review Letters **95**, 145301 (2005).

[139] A. D. Martin and J. Ruostekoski, *Quantum and thermal effects of dark solitons in a one-dimensional Bose gas,* Physical Review Letters **104**, 194102 (2010).

[140] E. A. L. Henn, J. A. Seman, G. Roati, K. M. F. Magalhães, and V. S. Bagnato, *Emergence of turbulence in an oscillating Bose-Einstein condensate,* Physical Review Letters **103**, 045301 (2009).

[141] K. Sasaki, N. Suzuki, D. Akamatsu, and H. Saito, *Rayleigh-Taylor instability and mushroom-pattern formation in a two-component Bose-Einstein condensate,* Physical Review A **80**, 063611 (2009).

[142] T. Kadokura, T. Aioi, K. Sasaki, T. Kishimoto, and H. Saito, *Rayleigh-Taylor instability in a two-component Bose-Einstein condensate with rotational symmetry,* Physical Review A **85**, 013602 (2012).

[143] J. P. Burke, J. L. Bohn, B. D. Esry, and C. H. Greene, *Prospects for mixed-isotope Bose-Einstein condensates in rubidium,* Physical Review Letters **80**, 2097–2100 (1998).

List of Publications

Publications in journals

1. Salla Gangi Reddy, **Shashi Prabhakar**, Chithrabhanu P, R. P. Singh, and R. Simon, *A polarization gadget with two quarter wave plates: Application to Mueller Polarimetry*, arXiv:1412.7805.

2. **Shashi Prabhakar**, Salla Gangi Reddy, A. Aadhi, Chithrabhanu P, and R. P. Singh, *Violation of Bell's inequality for phase singular beams*, arXiv: 1406.6239.

3. Chithrabhanu P, A. Aadhi, Salla Gangi Reddy, **Shashi Prabhakar**, Goutam K. Samanta, Gautam Paul and R. P. Singh, *Three particle Hyper Entanglement: Teleportation and Quantum Key Distribution*, arXiv:1311.7318.

4. Mandeep Singh, Kedar Khare, Anand K. Jha, **Shashi Prabhakar**, and R. P. Singh, *Accurate multipixel phase measurement with classical-light interferometry*, Physical Review A **91**, 021802(R) (2015), doi: 10.1103/PhysRevA.91.021802.

5. Salla Gangi Reddy, **Shashi Prabhakar**, Ashok Kumar, J. Banerji, and R. P. Singh, *Higher order optical vortices and formation of speckles*, Optics Letters **39**, 4364–4367 (2014), doi: 10.1364/OL.39.004364.

6. Salla Gangi Reddy, **Shashi Prabhakar**, A. Aadhi, J. Banerji, and R. P. Singh, *Propagation of an arbitrary vortex pair through an astigmatic optical system and determination of its topological charge*, Journal of the Optical Society of America A **31**, 1295-1302 (2014), doi: 10.1364/JOSAA.31.001295.

7. **Shashi Prabhakar**, Salla Gangi Reddy, A. Aadhi, Ashok Kumar, Chithrabhanu P, Goutam K. Samanta, and R. P. Singh, *Spatial distribution of Spontaneous Parametric Down-Converted Photons*, Optics Communication **326**, 64 (2014), doi: 10.1016/j.optcom.2014. 04.017.

8. Salla Gangi Reddy, **Shashi Prabhakar**, A. Aadhi, Ashok Kumar, Megh Shah, R. P. Singh, and R. Simon, *Measuring Mueller matrix of an arbitrary optical element with a universal SU(2) polarization gadget*, Journal of the Optical Society of America A **31**, 610–615 (2014), doi: 10.1364/JOSAA.31. 000610.

9. Salla Gangi Reddy, Ashok Kumar, **Shashi Prabhakar**, R. P. Singh, *Experimental generation of ring-shaped beams with random sources*, Optics Letters **38**, 4441–4444 (2013), doi: 10.1364/OL.38.004441.

10. **Shashi Prabhakar**, R. P. Singh, S. Gautam and D. Angom, *Annihilation of vortex dipole in an Oblate Bose-Einstein Condensate*, Journal of Physics B: Atomic, Molecular and Optical Physics **46**, 125302 (2013), doi: 10.1088/0953-4075/46/12/125302.

11. **Shashi Prabhakar**, Ashok Kumar, J. Banerji and R. P. Singh, *Revealing the order of a vortex through its intensity record*, Optics Letters **36**, 4398–4400 (2011), doi: 10.1364/OL. 36.004398.

12. Ashok Kumar, **Shashi Prabhakar**, Pravin Vaity, and R. P. Singh, *Information content of optical vortex fields*, Optics Letters **36**, 1161–1163 (2011), doi: 10.1364/OL.36.001161.

13. Abir Bandyopadhyay, **Shashi Prabhakar** and R. P. Singh, *Entanglement of a quantum optical elliptic vortex*, Physics Letters A **375**, 1926–1929 (2011), doi: 10.1016/j.physleta. 2011.03.044.

Conference Papers

1. Chithrabhanu P, A.Aadhi, Salla Gangi Reddy, **Shashi Prabhakar**, and R. P. Singh, *Construction of Coherent and Partially Coherent Orbital Angular Momentum Poincare Sphere*, Photonics-2014, IIT Kharagpur, West Bengal, India, paper M4A.82, December 13-16, 2014, URL: Photonics-2014-M4A.82.

2. **Shashi Prabhakar**, Salla Gangi Reddy, A. Aadhi, Chithrabhanu P, Goutam K. Samanta, and R. P. Singh, *Continuous-variable Entanglement in Optical Vortex Beams*, Photonics-2014, IIT Kharagpur, West Bengal, India, paper M4A.83, December 13-16, 2014, URL: Photonics-2014-M4A.83.

3. Salla Gangi Reddy, Chithrabhanu P, A. Aadhi, **Shashi Prabhakar**, and R. P. Singh, *Recovery of orbital angular momentum states after scattering*, Photonics-2014, IIT Kharagpur, West Bengal, India, paper S4C.4, December 13-16, 2014, URL: Photonics-2014-S4C.4.

4. Salla Gangi Reddy, **Shashi Prabhakar**, A. Aadhi, Alianwar M. A., J. Banerji, and R. P. Singh, *Modelling of scattered optical vortices*, Photonics-2014, IIT Kharagpur, West Bengal, India, paper S5A.32, December 13-16, 2014, URL: Photonics-2014-S5A.32.

5. Sean Nomoto, A. Aadhi, **Shashi Prabhakar**, R. P. Singh, R. Vyas, and S. Singh, *Observation of cross polarization of linearly polarized Airy beam*, Frontiers in Optics 2014, Arizona, United States, paper JTu3A.11, October 19-23, 2014, URL: FiO-2014-JTu3A.11.

6. Salla Gangi Reddy, **Shashi Prabhakar**, Ashok Kumar, J. Banerji, and R. P. Singh, *Variation of speckle size with the order of an optical vortex*, International conference on Optics & Optoelectronics, IRDE Dehradun, India, March 05-08, 2014.

7. Salla Gangi Reddy, Ashok Kumar, J. Banerji, **Shashi Prabhakar**, and R. P. Singh, *Optical vortices through a ground glass*, International conference on Optics & Optoelectronics, IRDE Dehradun, India, March 05-08, 2014.

8. Chithrabhanu P, A. Aadhi, Salla Gangi Reddy, **Shashi Prabhakar**, Goutam K. Samanta, and R. P. Singh, *A novel entangled source for higher dimensional quantum teleportation and QKD*, International conference on Optics & Optoelectronics, IRDE Dehradun, India, March 05-08, 2014.

9. Salla Gangi Reddy, **Shashi Prabhakar**, Ashok Kumar, and R. P. Singh, *Spatial Intensity Distribution of optical vortex beams*, presented at Workshop in recent advances in Photonics during December 17-18, 2013 at IIT Delhi, New Delhi, India.

10. Salla Gangi Reddy, Ashok Kumar, **Shashi Prabhakar**, R. P. Singh *Revival of the dark core in scattered optical vortices*, Proc. SPIE 8840, Optical Modeling and Performance Predictions VI, 884008, doi: 10.1117/12.2023037.

11. Ashok Kumar, Pravin Vaity, **Shashi Prabhakar**, R. P. Singh, *Topological aberration of phase singular light beams*, Photonics-2012, IIT Madras, Andhra Pradesh, India, paper M1C.2, December 10-12, 2012, URL: Photonics-2012-M1C.2.

12. **Shashi Prabhakar**, Salla Gangi Reddy, Ashok Kumar, A. Aadhi, Ashok Kumar, Goutam K. Samanta, R. P. Singh, *Spatial distribution of Spontaneous Parametric Down-Converted Photons*, Photonics-2012, IIT Madras, Andhra Pradesh, India, paper T1C.2, December 10-12, 2012, URL: Photonics-2012-T1C.2.

13. Salla Gangi Reddy, **Shashi Prabhakar**, A. Aadhi, Ashok Kumar, Megh Shah, R. P. Singh, R. Simon,*Determination of Mueller matrix of an optical element with Simon-Mukunda gadget*, Photonics-2012, IIT Madras, Andhra Pradesh, India, paper M1B.2, December 10-12, 2012, URL: Photonics-2012-M1B.2.

14. Ashok Kumar, **Shashi Prabhakar**, Pravin Vaity, R. P. Singh, *Spatial coherence properties of the one-dimensional projection of optical vortices*, Frontiers in Optics, OSA Technical Digest (2011), paper FThG6, URL FiO-2011-FThG6.

15. **Shashi Prabhakar**, Ashok Kumar, J. Banerji and R. P. Singh, *Revealing the order of a vortex through its intensity record*, Proceedings of 99$^{\text{th}}$ Session of Indian Science Congress, Section of Physical Sciences, KIIT University, Odisha, India, page 120, January 3-7, 2012.

16. **Shashi Prabhakar**, Ashok Kumar, Gangi Reddy, A. Aadhi, R. P. Singh, *Determination of Order of Vortex from Intensity Distribution*, Proceedings of IConTOP II, University of Calcutta, West Bengal, India, page 115, December 7-9, 2011.

17. Abir Bandyopadhyay, **Shashi Prabhakar**, R. P. Singh, *Wigner Distribution Function and Entanglement of Quantum Optical Elliptical Vortex*, AIP Conference Proceedings **1384**, 177–182 (2011), doi: 10.1063/1.3635861.

18. Pravin Vaity, Ashok Kumar, **Shashi Prabhakar**, R. P. Singh, *Airy beams interaction through photorefractive material in presence of an applied electric field*, Proceeddings of SPIE **8173**, 81730N (2010), doi: 10.1117/12.897797.

19. Ashok Kumar, **Shashi Prabhakar**, Pravin Vaity, R. P. Singh, *Two point correlation function for an optical vortex*, Photonics-2010, IIT Guwahati, Assam, India, page 556, December 12-15, 2010.

20. Ashok Kumar, Pravin Vaity, **Shashi Prabhakar**, R. P. Singh, *Decoherence of optical vortices in scattering*, Photonics-2010, IIT Guwahati, Assam, India, page 555, December 12-15, 2010.

21. Pravin Vaity, Ashok Kumar, **Shashi Prabhakar**, R. P. Singh, *2-D Airy beam propagation through photorefractive materials*, Photonics-2010, IIT Guwahati, Assam, India, page 523, December 12-15, 2010.

Publications attached with thesis

1. **Shashi Prabhakar**, Ashok Kumar, J. Banerji, and R. P. Singh, *Revealing the order of a vortex through its intensity record*, Optics Letters **36**, 22, 4398–4400 (2011), doi: 10.1364/OL.36.004398.

2. **Shashi Prabhakar**, Salla Gangi Reddy, Aadhi A, Ashok Kumar, Chithrabhanu P, G. K. Samanta, and R. P. Singh, *Spatial distribution of Spontaneous Parametric Down-Converted Photons*, Optics Communication **326**, 64 (2014), doi: 10.1016/j.optcom.2014.04.017.

3. **Shashi Prabhakar**, R. P. Singh, S. Gautam and D. Angom, *Annihilation of vortex dipole in an Oblate Bose-Einstein Condensate*, Journal of Physics B: Atomic, Molecular and Optical Physics **46**, 12, 125302 (2013), doi: 10.1088/0953-4075/46/12/125302.

Revealing the order of a vortex through its intensity record

Shashi Prabhakar,* Ashok Kumar, J. Banerji, and R. P. Singh

Theoretical Physics Division, Physical Research Laboratory, Ahmedabad 380 009, India
*Corresponding author: shaship@prl.res.in

Received August 22, 2011; revised October 6, 2011; accepted October 8, 2011;
posted October 11, 2011 (Doc. ID 153239); published November 15, 2011

We show that the intensity distribution of an optical vortex contains information of its order. Specifically, the number of dark rings in the Fourier transform of the intensity is found to be equal to the order of the vortex. Based on this property and the orthogonality of Laguerre polynomials, we demonstrate the feasibility of an experimental technique for determining the order of optical vortices. It shows the beauty of going to complementary spaces, which has been employed earlier also to find the information not available in other domains. © 2011 Optical Society of America

OCIS codes: 050.4865, 260.6042.

Optical vortices are singular points in the phase distribution of a light field and observed as dark points on the screen [1]. Light beams with such a feature have found a variety of applications in the optical manipulation of microscopic particles [2] and quantum information and computation [3].

Detection and determination of the charge of optical vortices is one of the basic requirements in singular optics. Most of the techniques to determine the order of vortices are based on interferometry [4–7]. The interferometry has been further extended to find the spatial coherence function that also provides information about the order of vortex [8]. All these methods require a good number of optical elements and their fine alignment. Aberrations in optical elements, scratch and dig, dust particles on these elements, and their misalignments disturb the characteristic interference pattern of the vortex. Therefore, efforts have been made to find the order of the vortex using techniques other than the interferometry [9–13].

In this Letter, we show that the order of a vortex can be obtained from the record of its intensity distribution itself. We know that when the order of the vortex increases, the size of the dark core at the center increases [14]. Moreover, the size of the dark core may vary depending on the resolution of the hologram used in the spatial light modulator (SLM) [15]. Therefore, just by measuring the size of the dark core, it is difficult to discriminate between the orders experimentally.

We provide a method to discriminate between the orders of the vortices by taking the Fourier transform (FT) of the recorded intensity of the vortex and using the orthogonality of the Laguerre polynomials. Our main result is based on Eq. (12) and Fig. 4.

The field of a vortex of order m can be written as

$$E_m(x,y) = (x+iy)^m \exp[-(x^2+y^2)/\sigma^2], \qquad (1)$$

where $\sigma = 1.69\,\text{mm}$ is the radius of the first diffraction order Gaussian beam at the CCD (see Fig. 1). The beam was generated by placing a grating without fork pattern at the SLM. The intensity of the vortex is given by

$$I_m(x,y) = (x^2+y^2)^m \exp[-2(x^2+y^2)/\sigma^2]. \qquad (2)$$

The FT of $I_m(x,y)$ has the expression

$$\mathcal{F}_m(\omega_1,\omega_2) = \int_{-\infty}^{\infty}\int_{-\infty}^{\infty}(x^2+y^2)^m \times \exp[-2(x^2+y^2)/\sigma^2 - i(\omega_1 x+\omega_2 y)]\mathrm{d}x\mathrm{d}y, \qquad (3)$$

where ω_1 and ω_2 are spatial frequencies. Expanding $(x^2+y^2)^m$ in a binomial series, Eq. (3) can be written as

$$\mathcal{F}_m(\omega_1,\omega_2) = \sum_{n=0}^{m}\binom{m}{n}\mathcal{I}_n(\omega_1)\mathcal{I}_{m-n}(\omega_2), \qquad (4)$$

where

$$\mathcal{I}_n(\omega_1) = \int_{-\infty}^{\infty} x^{2n}\exp(-2x^2/\sigma^2 - i\omega_1 x)\mathrm{d}x. \qquad (5)$$

Using the formulas [16]

$$\int_0^{\infty} x^{2n}\exp(-\beta^2x^2)\cos ax\,dx = (-1)^n\frac{\sqrt{\pi}}{(2\beta)^{2n+1}}\exp\left(-\frac{a^2}{4\beta^2}\right)H_{2n}\left(\frac{a}{2\beta}\right), \qquad (6)$$

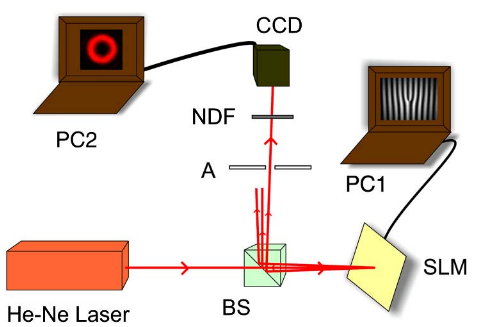

Fig. 1. (Color online) Experimental setup to generate optical vortices and to find their order.

$$H_{2n}(x) = (-1)^n 2^{2n} n! L_n^{-1/2}(x^2), \quad (7)$$

we get

$$\mathcal{I}_n(\omega_1) = \sqrt{\pi} \frac{\sigma^{2n+1}}{2^{n+1/2}} n! \exp\left(-\frac{\omega_1^2 \sigma^2}{8}\right) L_n^{-1/2}\left(\frac{\omega_1^2 \sigma^2}{8}\right), \quad (8)$$

and similarly for $\mathcal{I}_{m-n}(\omega_2)$. Substituting in Eq. (4) and performing the summation over n by means of the formula [16]

$$\sum_{n=0}^{m} L_n^{\alpha}(x) L_{m-n}^{\beta}(y) = L_m^{\alpha+\beta+1}(x+y), \quad (9)$$

we get

$$\mathcal{F}_m(\omega_1, \omega_2) = \frac{\pi \sigma^{2m+2}}{2^{m+1}} m! \exp(-\zeta) L_m(\zeta), \quad (10)$$

where $\zeta = (\omega_1^2 + \omega_2^2)\sigma^2/8$. In Eqs. (6)–(10), we have used the standard notations $H_n(x)$, $L_n(x)$, and $L_n^{\alpha}(x)$ to denote Hermite, Laguerre, and generalized Laguerre polynomials, respectively. By using the following orthogonality property of Laguerre polynomials

$$\int_0^{\infty} \exp(-\zeta) L_m(\zeta) L_n(\zeta) d\zeta = \delta_{m,n} \quad (11)$$

one finds that the integral

$$C_{mn} = \int_0^{\infty} \mathcal{F}_m(\zeta) L_n(\zeta) \mathrm{d}\zeta \quad (12)$$

will give a peak value for $m = n$. We have evaluated C_{mn} numerically by using the FT of the measured intensity profiles. We expect this method to be sensitive enough to detect any order of the vortex.

The experimental setup to find the order of the vortices is shown in Fig. 1. A Gaussian beam from an intensity stabilized He-Ne laser (Spectra-Physics, 117A) is sent toward a beam splitter (BS). The transmitted beam from BS goes toward the SLM (Holoeye, LC-R 2500). SLM is a liquid crystal based device that can modulate light in amplitude as well as in phase and therefore it can be used as a dynamic diffractive optical element. The positions of the BS and the SLM are aligned in such a way that the transmitted beam from the BS falls normal to the SLM. Higher order vortices are produced in the first diffraction order by introducing different fork patterns onto the SLM via a computer (PC1). An aperture A is used to select the required first diffraction order produced from the SLM. It is then passed through a neutral density filter (NDF) to decrease the intensity of the vortex so that it does not saturate the CCD camera. The final images of the vortices are recorded with a CCD camera and stored in a computer (PC2) for further processing. In Fig. 2, we show the intensity distribution of the optical vortex obtained from Eq. (2) and from experiment, i.e., the CCD camera. We would like to make it clear that the aperture A is being used just to select a particular diffracted order from the SLM, not to diffract the vortex. We take care that the selection does not introduce any diffraction ring to the vortex, which can be seen from the experimental intensity profiles of the vortices in Fig. 2.

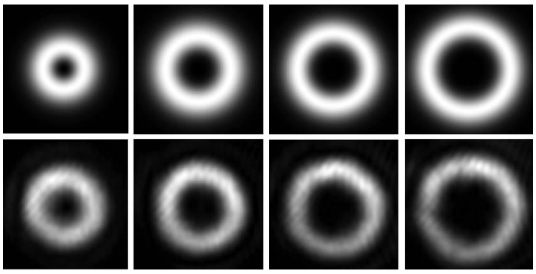

Fig. 2. Intensity distribution of optical vortices of orders $m = 1$ to 4 (from left to right): theoretical (top) and experimental (bottom).

Before proceeding to our main result, it is important to realize that the FT of the vortex intensity can, in principle, determine the order of the vortex as the number of zeroes of $L_m(\zeta)$ in Eq. (10) equals the order of the vortex. This is most clearly seen in the contour plot of the following quantity:

$$\mathcal{G}_m(\omega_1, \omega_2) = \log[1 + |\mathcal{F}_m(\omega_1, \omega_2)|]. \quad (13)$$

The zeros will appear as dark rings and thus the order of the vortex will be equal to the number of dark rings in the contour plot of $\mathcal{G}_m(\omega_1, \omega_2)$. The rationale behind plotting $\mathcal{G}_m$ instead of $\mathcal{F}_m$ was to identify the zeros more clearly.

The fast-Fourier transform (FFT) of the measured intensity distributions is carried out numerically using Matlab. These images are processed in Matlab to reduce the noise and adjust the brightness and contrast. In Fig. 3, we show the contour plots of $\mathcal{G}_m(\omega_1, \omega_2)$ for vortices of different orders. The corresponding theoretical results are obtained by using Eqs. (10) and (13). It is clearly seen that the number of dark rings in each plot equals the order of the corresponding vortex and the experimental results are in excellent agreement with the theoretical predictions. We mention parenthetically that for lower order vortices, a contour plot of $\mathcal{G}_m(\omega_1, \omega_2)$ will suffice to determine the order of the vortex. For higher order vortices, however, it will become difficult to see the rings beyond a certain order because of the dampening effect of the exponential factor in Eq. (10). This is why our chosen method is based on the orthogonality property of Laguerre polynomials rather than relying upon a contour plot of $\mathcal{F}_m$ or $\mathcal{G}_m$.

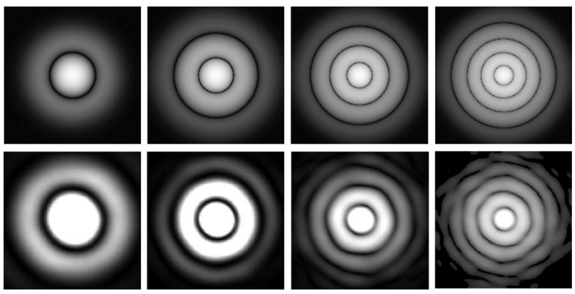

Fig. 3. Distribution of $\mathcal{G}_m(\omega_1, \omega_2)$ computed from the intensity distributions of Fig. 2: theoretical (top) and experimental (bottom).

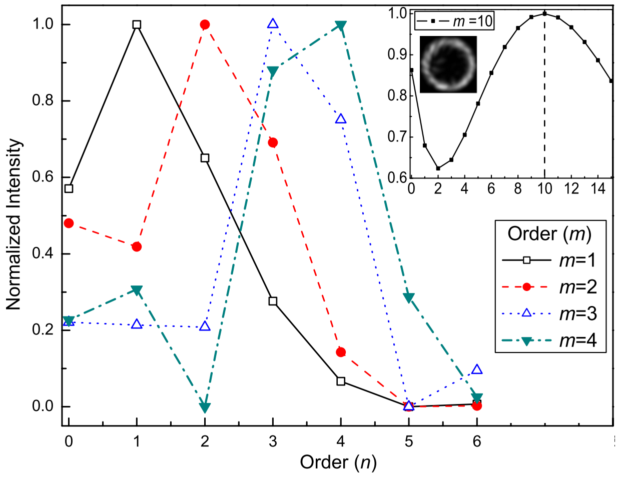

Fig. 4. (Color online) Normalized orthogonal integrals C_{mn} for optical vortices of orders $m = 1$ to 4. Inset shows C_{mn} and the intensity record of vortex for $m = 10$.

Using orthogonal relations of Laguerre polynomials, one can detect any order of the vortex. The results are shown in Fig. 4. It shows that for an optical vortex of order m, the normalized orthogonal integral has maximum value when $m = n$ and lesser values for $m \neq n$.

The sensitivity of this method can be easily established in the present context. For example, note that the outermost dark ring for fourth order vortex is not so distinct in Fig. 3 and thus it is not clear whether the vortex is of order 3 or 4. The orthogonality integral, in contrast, shows a clear peak for order $m = 4$. In fact, our method applies even for a vortex of order $m = 10$, as shown in the inset of Fig. 4.

We would like to point out that in [9], it is the FT of the field that has been absolute squared and gives the diffracted intensity, which is again Fourier transformed to find the spatial frequency and order of the vortex. In our case, it is the FT of the intensity of an undiffracted vortex. This can be seen in our analytical treatment as well. Furthermore, our method does not use any annular aperture for diffraction. Therefore, the maximal topological charge that can be measured is not limited by the width of the annular aperture. As a demonstration, we have successfully applied our method for a vortex of order as high as $m = 10$. Moreover, for a given vortex, the only optical element one really requires is an NDF to reduce the intensity of the vortex to avoid saturation of the CCD. Thus, we have the least optics and the least aberrations.

In this Letter, we have outlined a technique to determine the order of a vortex based on the FT of its intensity profile and the orthogonality of the Laguerre polynomials. Since the phase information is lost in the intensity record of a vortex, our method cannot, however, determine the sign of its charge. At present, the method works for on-axis, isotropic vortices embedded in a Gaussian host. These limitations notwithstanding, the strong point of this technique is its simplicity and novelty. Since the experimentally recorded vortices do not have ideal Gaussian hosts, one experiences noise in the experimentally determined $\mathcal{G}_m(\omega_1, \omega_2)$ (see bottom row of Fig. 3) and in Fig. 4, C_{mn} does not reduce to zero for $m \neq n$. However, it still shows peaks for $m = n$ and is thus effective in determining the order of the vortex. Moreover, our method is fast. It takes just a fraction of a second (0.85 seconds on Pentium IV, 3.4 GHz with 1.2 GB RAM) to calculate $\mathcal{G}_m(\omega_1, \omega_2)$ and a similar time in finding the C_{mn}. A graphical user interface can be created using a standard FFT routine for automating the process. This will help to get the order of vortex in real time. In conclusion, we have shown how complementary space can provide us with the order of the vortex [17,18].

References

1. L. Allen, S. M. Barnett, and M. J. Padgett, *Optical Angular Momentum* (IOP, 2003).
2. D. G. Grier, Nature **424**, 810 (2003).
3. G. Molina-Terriza, J. P. Torres, and L. Torner, Nat. Phys. **3**, 305 (2007).
4. D. P. Ghai, S. Vyas, P. Senthilkumaran, and R. S. Sirohi, Opt. Lasers Eng. **46**, 419 (2008).
5. H. I. Sztul and R. R. Alfano, Opt. Lett. **31**, 999 (2006).
6. E. Fraczek, W. Fraczek, and J. Masajada, Optik **117**, 423 (2006).
7. J. Arlt, K. Dholakia, L. Allen, and M. J. Padgett, J. Mod. Opt. **45**, 1231 (1998).
8. A. Kumar, S. Prabhakar, P. Vaity, and R. P. Singh, Opt. Lett. **36**, 1161 (2011).
9. C.-S. Guo, L.-L. Lu, and H.-T. Wang, Opt. Lett. **34**, 3686 (2009).
10. D. P. Ghai, P. Senthilkumaran, and R. S. Sirohi, Opt. Lasers Eng. **47**, 123 (2009).
11. L. Yongxin, T. Hua, P. Jixiong, and L. Baida, Opt. Laser Technol. **43**, 1233 (2011).
12. I. Moreno, J. A. Davis, B. Melvin, L. Pascoguin, M. J. Mitry, and D. M. Cottrell, Opt. Lett. **34**, 2927 (2009).
13. L. E. E. de Araujo and M. E. Anderson, Opt. Lett. **36**, 787 (2011).
14. J. E. Curtis and D. G. Grier, Phys. Rev. Lett. **90**, 133901 (2003).
15. A. Kumar, P. Vaity, Y. Krishna, and R. P. Singh, Opt. Lasers Eng. **48**, 276 (2010).
16. I. S. Gradshteyn and I. M. Ruzhik, *Table of Integrals, Series and Products* (Academic, 2007).
17. G. S. Agarwal and R. P. Singh, Phys. Lett. A **217**, 215 (1996).
18. D. E. James, H. C. Kandpal, and E. Wolf, Astrophys. J. **445**, 406 (1995).

Optics Communications 326 (2014) 64–69

Contents lists available at ScienceDirect

Optics Communications

journal homepage: www.elsevier.com/locate/optcom

Spatial distribution of spontaneous parametric down-converted photons for higher order optical vortices

Shashi Prabhakar [a,*], Salla Gangi Reddy [a], A. Aadhi [a], Ashok Kumar [b], P. Chithrabhanu [a], G.K. Samanta [a], R.P. Singh [a]

[a] Physical Research Laboratory, Navrangpura, Ahmedabad 380009, India
[b] Instituto de Fisica, Universidade de Sao Paulo, Sao Paulo 66318, Brazil

ARTICLE INFO

Article history:
Received 28 January 2014
Received in revised form
7 April 2014
Accepted 8 April 2014
Available online 24 April 2014

Keywords:
Parametric down-conversion
Optical vortex
Entanglement
Critical beam-width

ABSTRACT

We make a source of entangled photons using spontaneous parametric down-conversion (SPDC) in a non-linear crystal and study the spatial distribution of photon pairs obtained through the down-conversion of different modes of light including higher order vortices. We observe that for the Gaussian pump, the thickness of the SPDC ring varies linearly with the radius of pump beam. However, in case of vortex carrying beams, two concentric SPDC rings are formed for beams above a critical radius. The full width at half maximum (FWHM) of SPDC rings increase with increase in the order of optical vortex beams. The presence of a critical beam width for the vortices as well as the observed FWHM of the SPDC rings are supported with our numerical results.

1. Introduction

The process of spontaneous parametric down-conversion (SPDC) has been used extensively for the generation of entangled photon pairs in many recent experiments. The purpose of these experiments range from Bell's inequality violation [1] to the implementation of quantum information protocols [2]. In the process of SPDC, a laser pump beam photon interacts with second-order nonlinear $\chi^{(2)}$ crystal, gets annihilated and gives rise to the emission of two photons. These two photons are generated simultaneously and follow the laws of energy and momentum conservation. The phenomena of SPDC was first observed by Burnham and Weinberg [3] and theoretically studied by Hong and Mandel [4].

The photon pairs generated through SPDC are entangled in the spatial degrees of freedom i.e. position-momentum entanglement [5] as well as entanglement in orbital angular momentum (OAM) [6]. This OAM entanglement can be described by a multi-dimensional Hilbert space [7–9], compared to the case of polarization entanglement which is limited to two dimensions only [10]. These photon pairs have been found to be entangled in time-bin also [11].

Optical vortices (OV) carry a dark core in a bright background [12]. If there is a phase change of $2\pi l$ around the point of darkness, it is called a vortex of topological charge l, where l is an integer. The sense of rotation determines the sign of topological charge of the vortex. A beam with such a phase structure has a helical wavefront and, therefore, carries an OAM of $l\hbar$ per photon [13] for a vortex of topological charge l. These beams have found a variety of applications, such as optical trapping of atoms [14], optical tweezing and spanning [15], optical communication [16], imaging [17], and quantum information and computation [8].

For any application of entangled photons generated through the SPDC, it is important to know the spatial distribution of photons arising from the SPDC process. For the Gaussian pump beam, the spatial distribution of SPDC photons has already been reported [18–21]. However, for photons generated by pumping with higher order vortices, it has not been reported so far. Although, the phase-matching by optical vortex pump beam has been studied theoretically by Pittman et al. [22].

With the availability of low noise and high quantum-efficiency electron-multiplying CCDs (EMCCD), the experiments with low photon level imaging have become possible [23]. To observe the shape of the SPDC ring formed by the Gaussian as well as optical vortex beams, we have carried out experimental studies using EMCCD. The observed experimental results are supported with our numerical results. The theory regarding the SPDC has been

* Corresponding author.
E-mail address: shaship@prl.res.in (S. Prabhakar).

http://dx.doi.org/10.1016/j.optcom.2014.04.017
0030-4018/

discussed in Section 2, experiments performed in Section 3 and results in Section 4. Finally we conclude in Section 5.

2. Theory

The intensity distribution of an optical vortex of order l can be written as

$$I_l(x,y) = I_0(x^2+y^2)^{|l|} \exp\left(-\frac{x^2+y^2}{\sigma^2}\right), \tag{1}$$

where σ is the beam radius of host beam, I_0 is the maximum intensity in the bright ring. Clearly, Eq. (1) shows that the Gaussian beam is a special case of optical vortex with $l=0$.

The nonlinear effects in crystals have been exploited in a number of applications such as frequency doubling, optical parametric oscillation and the SPDC [24]. When a nonlinear crystal, for example Beta-Barium Borate (BBO), with non-zero second order electric susceptibility ($\chi^{(2)}$) is pumped by an intense laser, a *pump* photon (frequency ω_p and wave-vector $\mathbf{K}_p$) splits into a photon pair called *signal* and *idler*. The energy and momentum conservation provides us with

$$\hbar\omega_p = \hbar\omega_s + \hbar\omega_i, \tag{2}$$

$$\mathbf{K_p} = \mathbf{K_s} + \mathbf{K_i}, \tag{3}$$

where suffices s and i denote signal and idler photons respectively. The phase matching is determined by the frequency of pump laser beam and the orientation of crystal optic axis with respect to the pump. Eq. (2) can be simplified as

$$\frac{1}{\lambda_p} = \frac{1}{\lambda_s} + \frac{1}{\lambda_i}, \tag{4}$$

where λ_p, λ_s and λ_i denote wavelengths of pump, signal and idler photons respectively. We have considered e→o + o type (e: extraordinary, o: ordinary) interaction. Hence, Eq. (3) can be written as

$$\frac{2\pi n_e(\lambda_p,\Theta)}{\lambda_p} = \frac{2\pi n_o(\lambda_s)}{\lambda_s}\cos(\phi_s) + \frac{2\pi n_o(\lambda_i)}{\lambda_i}\cos(\phi_i) \tag{5}$$

$$\frac{2\pi n_o(\lambda_s)}{\lambda_s}\sin(\phi_s) = \frac{2\pi n_o(\lambda_i)}{\lambda_i}\sin(\phi_i) \tag{6}$$

where ϕ_s is the angle between $\mathbf{K_p}$ and $\mathbf{K_s}$, ϕ_i is the angle between $\mathbf{K_p}$ and $\mathbf{K_i}$ and Θ is the direction of optic axis with respect to $\mathbf{K_p}$. $n_e(\lambda_p,\Theta)$ and $n_o(\lambda_{s,i})$ are the extraordinary and ordinary refractive indices for respective wavelengths. They are obtained from the Sellmeier equations [24] and for the BBO crystal used in the experiment can be written as

$$n_o(\lambda) = \sqrt{2.7359 + \frac{0.01878}{\lambda^2 - 0.01822} - 0.01354\lambda^2} \tag{7}$$

$$n_e(\lambda) = \sqrt{2.3753 + \frac{0.01224}{\lambda^2 - 0.01667} - 0.01516\lambda^2} \tag{8}$$

$$n_e(\lambda,\Theta) = n_o(\lambda)\sqrt{\frac{1+\tan(\Theta)^2}{1+\left[\frac{n_o(\lambda)}{n_e(\lambda)}\times\tan(\Theta)\right]^2}} \tag{9}$$

where λ is in μm.

In Fig. 1, we have given a sketch of the SPDC photon pair generation in non-collinear type-I SPDC process. **C** denotes the crystal optic axis. The angular separation between $\mathbf{K_p}$ and $\mathbf{K_s}$ is due to energy and phase-matching conditions (Eqs. (5) and (6)) required for the SPDC process. We have also shown generation of a pair of signal and idler photons and formation of the ring

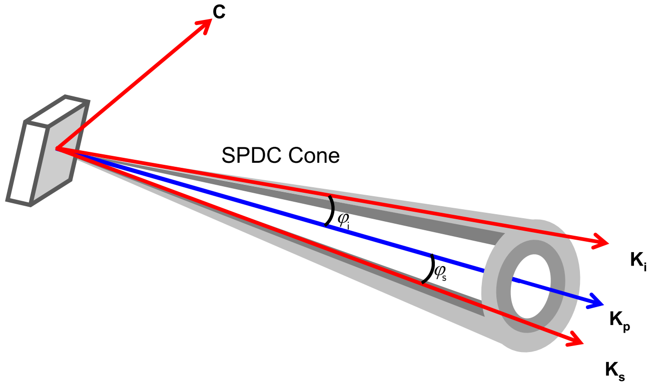

Fig. 1. Sketch diagram for the SPDC ring emission after passing the pump beam through the BBO crystal. Light and dark gray levels represent generation of idler and signal photon SPDC rings respectively.

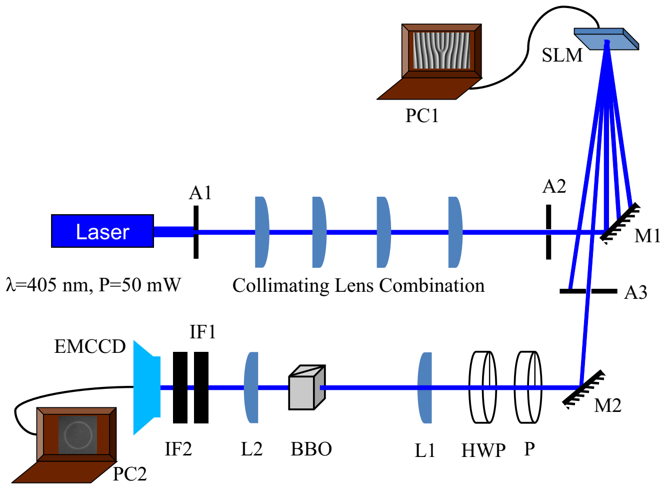

Fig. 2. Experimental setup for the study of SPDC photon pair distribution with an optical vortex as pump beam.

centered around $\mathbf{K_p}$. In the present case, we have assumed that the pump beam has same horizontal and vertical widths.

We have used a negative-uniaxial BBO crystal with non-linear coefficient $d_{\text{eff}} = 2.00$ pm/V, thickness 5 mm and optic axis $\Theta = 29.7^\circ$. The pump beam with wavelength $\lambda_p = 405$ nm is incident normal to the crystal. We plan to study the degenerate or near-degenerate case in which the signal and idler photons have almost same wavelength $\lambda_{s,i} = 810 \pm 5$ nm. The wavelength for down-converted photons is chosen from the interference filters (IF) used in the experiment. With these experimental parameters, Eqs. (5) and (6) have been solved to determine ϕ_s and ϕ_i by Runge–Kutta (RK) method for a particular value of λ_s and λ_i satisfied by Eq. (4).

Numerical simulations have been performed by first considering a particular value of λ_s and λ_i. Angles ϕ_s and ϕ_i are evaluated using RK method for chosen λ_s, λ_i and experimental parameters. The signal and idler photons are generated in cones having half-opening angle ϕ_s and ϕ_i as represented in Fig. 1 and appear as two rings on the detector plane. The center of these rings is concentric with the pump beam. Now, consider a single point on the intensity distribution of pump falling on the crystal. The stream of single photons passing through the chosen point generates SPDC rings whose radius depends on the distance between crystal and EMCCD. The intensity of the rings is proportional to the intensity at the selected point. The rings corresponding to signal and idler photons are then added to obtain the SPDC ring for the pump photons. In a similar way, rings for all other points of pump intensity distribution are obtained and added. The obtained spatial

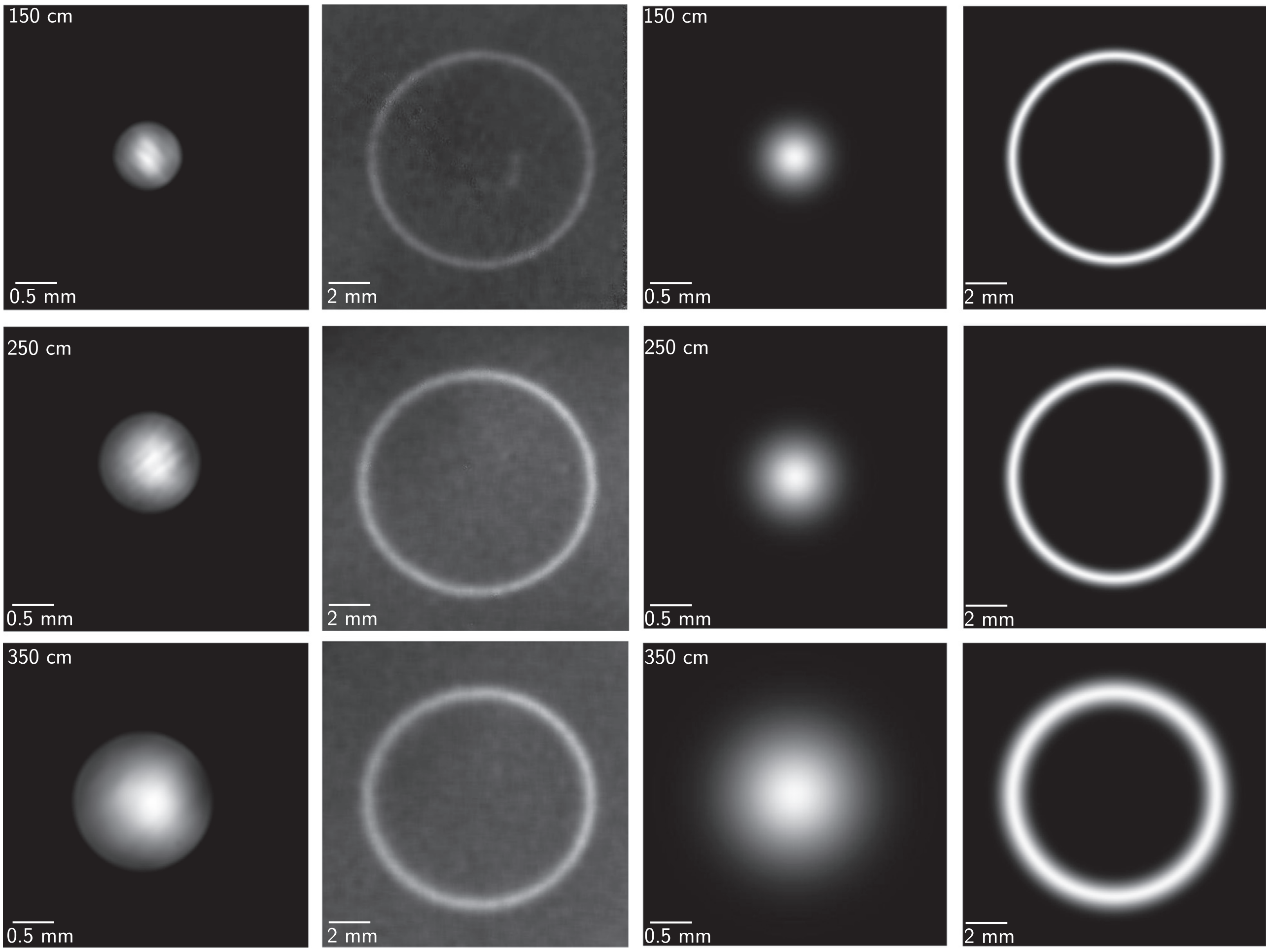

Fig. 3. Experimental (left) and numerical (right) are Gaussian pump and their corresponding SPDC rings recorded at distances 150 cm, 250 cm and 350 cm from the SLM.

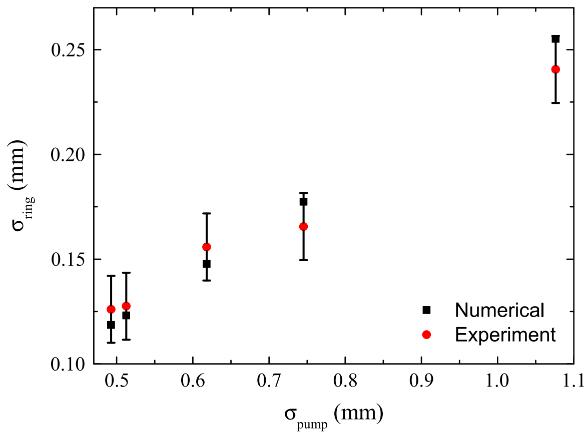

Fig. 4. Variation of σ_{ring} with σ_{pump}. The curve shows the linear variation in thickness of the SPDC ring with the beam-width of Gaussian pump beam.

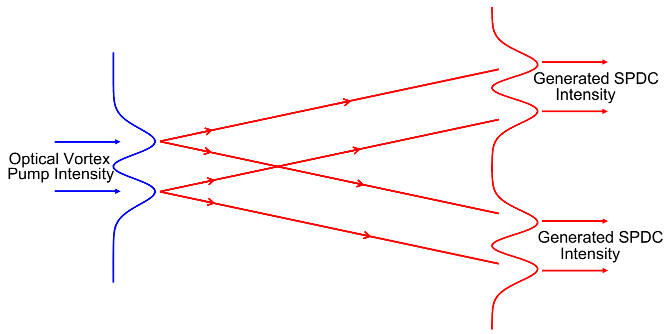

Fig. 5. Schematic diagram for the generation of two rings when pumped with optical vortex beams. (For interpretation of the references to color in this figure caption, the reader is referred to the web version of this article.)

distribution will depend on the shape and size of the pump beam. This will provide the SPDC ring for λ_s and λ_i. The contributions due to whole wave-length range (810 ± 5 nm) allowed by the IF have been considered to obtain the resultant spatial distribution of SPDC ring.

3. Experimental setup

The experimental set-up to study the SPDC photon distribution generated by the Gaussian as well as the optical vortex pump beam is shown in Fig. 2. The astigmatism of the diode laser (RGBLase 405 nm, 50 mW) has been removed by using a combination of lenses. The collimated beam is then sent to a spatial light modulator (SLM) (Hamamatsu LCOS SLM X-10468-05), which is interfaced with computer (PC1). Blazed holograms have been used to generate OV with higher power in the first diffraction order [25]. The first diffracted order is selected with an aperture A3. Polarizer (P) and half-wave plate (HWP) are used to select and rotate the polarization of pump beam respectively. BBO crystal ($6 \times 6 \times 5$ mm^3) with optic axis at 29.7° is used for the parametric down-conversion. As the size of OV beams of higher order becomes bigger than the size of the crystal, we have used a lens L1 ($f = 15$ cm) to loosely focus the vortex beam on the crystal. The BBO crystal is

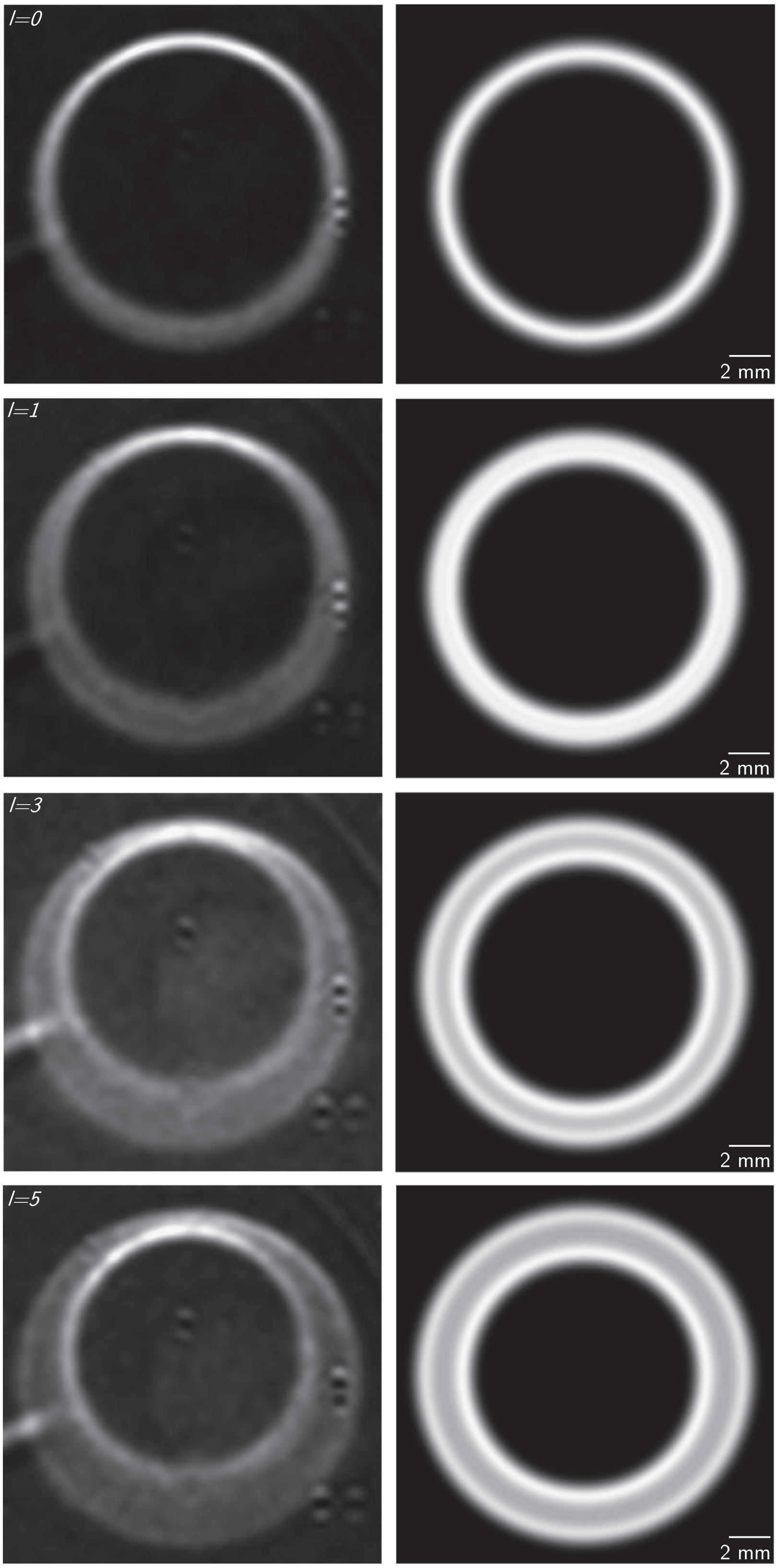

Fig. 6. Experimental (left) and numerical (right) SPDC rings due to an optical vortex pump beam for orders 0, 1, 3 and 5. Spot in the center of experimental images corresponds to the unfiltered pump beam.

mounted on a rotation stage, so that phase-matching angle can be achieved by rotating the crystal along its optic axis. After achieving phase-matching, the crystal remains unaltered for all the observations.

When phase-matched, the output cone makes half angle of $\sim 4^\circ$ with pump direction $\mathbf{K_p}$. The BBO crystal is kept in such a way that it can down-convert only vertically polarized light. Therefore, when angle of the HWP is 0° (45°), then we will get (not get) down-converted photons. Image of the down-converted ring is recorded by Andor iXon$_3$ EMCCD camera using an imaging lens of focal length 5 cm. We have used the EMCCD in background correction mode. In this mode, background is obtained when $\lambda/2$ plate is at 45° and signal is obtained when $\lambda/2$ plate is at 0°. The central bright spot in experimental observations show the unfiltered pump beam. This could not be subtracted while subtracting the background due to shift in its position during the rotation of HWP from 45° to 0°. The interference filters IF1 and IF2 pass only the down-converted photons of wave-length 810 ± 5 nm and block the pump photons of wave-length 405 nm. Two interference filters have been used to reduce the pump photons as much as possible.

The power of 405 nm laser falling on the BBO crystal was 2 mW. EMCCD was operated at −80 °C. Further, we have taken images by accumulating 50 frames exposure time of 1 s. We have used the complete 512×512 pixels of the camera. The readout rate was set at 1 MHz 16-bit. Since the observed SPDC rings were sufficiently intense, we have not enabled the electron-multiplication gain.

The size of pump beam has been measured by imaging the beam at the position of crystal with Point-Grey (FL2-20S4C) CCD camera. The images obtained from the CCD camera are read in Matlab for further processing. The 2-D curve fitting is used to obtain the best-fit intensity distribution obtained in Eq. (1) that provides us with beam-width of the pump (σ_{pump}). For our numerical calculations, we have used the best-fit value of σ_{pump} obtained experimentally.

4. Result and discussion

The objective of the experimental work is to characterize the spatial distribution of degenerate SPDC photon pairs produced by higher order vortices and verify the results obtained with numerical calculations. Before pumping the nonlinear crystal with high order vortices, we study the distribution of SPDC photons generated by the Gaussian beam of different widths.

To make a comparison of spatial distribution of down-converted photons due to the Gaussian and the vortex beams, the Gaussian beam is generated using the SLM by transferring the blazed grating hologram of topological charge 0 to the SLM. To vary the width of the Gaussian beam, we have used the beam at different propagation distances from the SLM (150–350 cm in the steps of 50 cm s). As the size of beam was lower than the aperture of the crystal at 350 cm from the SLM, lens (L1) was not used. The experimentally and numerically obtained SPDC rings are shown in Fig. 3. We observe an increase in thickness of the SPDC ring as the pump beam size increases.

To obtain a quantitative variation of SPDC ring, we use the line profile through the SPDC rings along their center. Numerically, we have observed that the SPDC ring fits with a Gaussian function. To calculate the width of SPDC ring (σ_{ring}), the profiles obtained are fitted with a Gaussian function as in Eq. (1) for $l=0$. The variation of thickness of the SPDC rings with the size of the pump beam is shown in Fig. 4. Numerical and experimental results are found to be in good agreement with each other. We find that our results are similar to the one obtained earlier [19].

Fig. 5 shows the generation of two rings when the BBO crystal is pumped with OV. The blue and red lines show the intensity distribution of the pump and the SPDC photons. As the size of optical vortex goes beyond the aperture of BBO crystal, we have used lens (L1) to loosely focus it. It has been observed that the SPDC ring due to optical vortex forms two concentric bright rings with non-zero intensity in middle. The SPDC rings due to optical vortices are shown in Fig. 6. From these images, we can observe the increase in thickness of the SPDC ring.

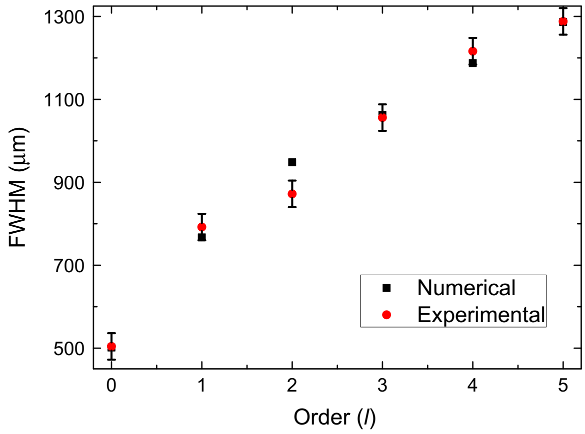

Fig. 7. Variation of FWHM of SPDC ring for optical vortex pump beams with the order of optical vortices.

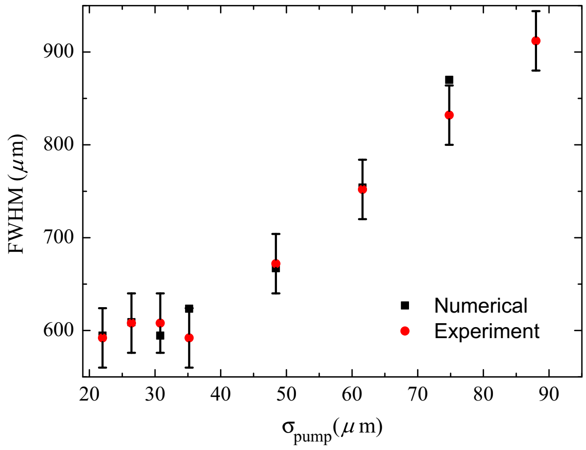

Fig. 8. Variation of FWHM of SPDC ring for optical vortex pump beam of order $l=2$ with beam width of host beam.

With the increase in topological charge of vortices, the full width at half maximum (FWHM) of the ring increases. The separation between the inner and the outer ring also increases with the increase in order as shown in Fig. 7. However, we can observe the asymmetry caused due to the crystal length. This asymmetry arises due to the longitudinal phase matching and depends on nonlinear crystal properties of the crystal, including crystal length [19]. This is one of the factors which affects the selection of entangled photons and consequently the total coincidence counts.

We have also observed that if σ_{pump} is lower than a particular value for the OV of topological charge l, then there will not be any change in FWHM. This variation has been studied by varying σ_{pump} and keeping the order l fixed. We have observed that the FWHM of the ring starts increasing only when σ_{pump} is more than a particular beam size, called critical beam size. The variation of FWHM of SPDC ring for order $l=2$ with σ_{pump} is shown in Fig. 8. In case of OV, the numerical and experimental results are in good agreement with each other.

5. Conclusion

The spatial distribution of entangled photons generated by non-linear crystal is of importance in the field of quantum information and quantum computation. We have observed a linear increase in thickness of the SPDC ring with beam radius of the pump.

We have also observed the formation of two concentric SPDC rings if the crystal is pumped with optical vortex beams. One of the reasons for generation of two rings is the dark core of optical vortex i.e. specific intensity distribution of the vortex. The numerical and experimental widths of the SPDC ring are in good agreement with each other. The formation of two rings takes place when the pump beam size is more than the critical beam size. These observations would be useful in the experiments to maximize the coincidence counts. Physically, the broadened SPDC is a consequence of the greater spread of pump transverse wave-vectors, resulting in phase matching for a greater spread of signal and idler transverse wave-vectors.

Acknowledgments

Authors wish to acknowledge Dr. A.K. Jha for fruitful discussion and experimental techniques. The numerical calculations reported in this paper have been performed on a 3 TeraFlop high-performance cluster at Physical Research Laboratory (PRL), Ahmedabad, India.

References

[1] L. Zhang, A.B. U'ren, R. Erdmann, K.A. ODonnell, C. Silberhorn, K. Banaszek, I.A. Walmsley, J. Mod. Opt. 54 (5) (2007) 707.
[2] P. Kok, K. Nemoto, T.C. Ralph, J.P. Dowling, G.J. Milburn, Rev. Mod. Phys. 79 (1) (2007) 135.
[3] D. Burnham, D. Weinberg, Phys. Rev. Lett. 25 (2) (1970) 84.
[4] C. Hong, L. Mandel, Phys. Rev. A 31 (4) (1985) 2409.
[5] M.P. Edgar, D.S. Tesca, F. Izdebski, R.E. Warburton, J. Leach, M. Agnew, G.S. Buller, R.W. Boyd, M.J. Padgett, Nat. Commun. 3 (2012) 984.
[6] G. Molina-Terriza, J.P. Torres, L. Torner, Nat. Phys. 3 (5) (2007) 305.
[7] C. Law, J. Eberly, Phys. Rev. Lett. 92 (12) (2004) 127903.
[8] A. Mair, A. Vaziri, G. Weihs, A. Zeilinger, Nature 412 (6844) (2001) 313.
[9] J.C. Howell, R.S. Bennink, S.J. Bentley, R.W. Boyd, Phys. Rev. Lett. 92 (21) (2004) 210403.
[10] P. Kwiat, K. Mattle, H. Weinfurter, A. Zeilinger, A. Sergienko, Y. Shih, Phys. Rev. Lett. 75 (24) (1995) 4337.
[11] C. Simon, J.-P. Poizat, Phys. Rev. Lett. 94 (3) (2005) 030502.
[12] L. Allen, S.M. Barnett, M.J. Padgett, Optical Angular Momentum, Institute of Physics Pub, London, 2003.
[13] M. Soskin, V. Gorshkov, M. Vasnetsov, J. Malos, N. Heckenberg, Phys. Rev. A 56 (5) (1997) 4064.
[14] T. Kuga, Y. Torii, N. Shiokawa, T. Hirano, Y. Shimizu, H. Sasada, Phys. Rev. Lett. 78 (25) (1997) 4713.
[15] D.G. Grier, Nature 424 (6950) (2003) 810.
[16] N. Bozinovic, Y. Yue, Y. Ren, M. Tur, P. Kristensen, H. Huang, A.E. Willner, S. Ramachandran, Science 340 (6140) (2007) 1545.
[17] T. Brunet, J.-L. Thomas, R. Marchiano, Phys. Rev. Lett. 105 (3) (2010) 034301.
[18] H. Di Lorenzo Pires, F.M.G.J. Coppens, M.P. van Exter, Phys. Rev. A 83 (3) (2011) 033837.
[19] R. Ramírez-Alarcón, H. Cruz-Ramírez, A.B. U'Ren, Laser Phys. 23 (5) (2013) 055204.
[20] T. Grayson, G. Barbosa, Phys. Rev. A 49 (4) (1994) 2948.
[21] H. Cruz-Ramírez, R. Ramírez-Alarcón, F.J. Morelos, P.A. Quinto-Su, J.C. Gutiérrez-Vega, A.B. U'Ren, Opt. Express 20 (28) (2012) 29761.
[22] T. Pittman, D. Strekalov, D. Klyshko, M. Rubin, A. Sergienko, Y. Shih, Phys. Rev. A 53 (4) (1996) 2804.
[23] R. Fickler, M. Krenn, R. Lapkiewicz, S. Ramelow, A. Zeilinger, Sci. Rep. 3 (2013) 1914.
[24] R.W. Boyd, Nonlinear Optics, Academic Press, San Diego, CA, USA, 2003.
[25] O. Bryngdahl, J. Opt. Soc. Am. 60 (1) (1970) 1401.

J. Phys. B: At. Mol. Opt. Phys. **46** (2013) 125302 (8pp) doi:10.1088/0953-4075/46/12/125302

Annihilation of vortex dipoles in an oblate Bose–Einstein condensate

Shashi Prabhakar[1], R P Singh[1], S Gautam[2] and D Angom[1]

[1] Physical Research Laboratory, Navrangpura, Ahmedabad 380 009, India
[2] Department of Physics, Indian Institute of Science, Bangalore 560 012, India

E-mail: angom@prl.res.in

Received 29 December 2012, in final form 23 April 2013
Published 22 May 2013
Online at stacks.iop.org/JPhysB/46/125302

Abstract
We theoretically explore the annihilation of vortex dipoles, generated when an obstacle moves through an oblate Bose–Einstein condensate, and examine the energetics of the annihilation event. We show that the grey soliton, which results from the vortex dipole annihilation, is lower in energy than the vortex dipole. We also investigate the annihilation events numerically and observe that annihilation occurs only when the vortex dipole overtakes the obstacle and comes closer than the coherence length. Furthermore, we find that noise reduces the probability of annihilation events. This may explain the lack of annihilation events in experimental realizations.

(Some figures may appear in colour only in the online journal)

1. Introduction

One of the important developments in recent experiments on atomic Bose–Einstein condensates (BECs) is the creation of vortices and the study of their dynamics [1, 2]. Equally important is the recent experimental observation of a vortex dipole, which consists of a vortex–antivortex pair, when an obstacle moves through a BEC [3], and the observation of vortex dipoles produced through phase imprinting [4, 5]. In superfluids, the vortices carry quantized angular momenta and are the topological defects, which often serve as the conclusive evidence of superfluidity. In a vortex dipole, vortices of opposite circulation cancel each other's angular momentum and thus carry only linear momentum. This is the cause of several exotic phenomena such as leap frogging, snake instability [6], orbital motion [7], trapping [8] and others. The effects of vortices are widespread in classical fluid flow [9] and optical manipulation [10]. A good description of vortices in superfluids is given in [11] and the review articles [12, 13]. A detailed discussion of vortices is given in [14].

Among the important phenomena associated with the BEC, the creation, dynamics and annihilation of vortex dipoles carry useful information associated with the system. Several methods have been suggested to nucleate vortices and recently, nucleation of the vortices has been observed experimentally by passing a Gaussian obstacle through the BEC with a speed greater than some critical speed [3]. The trajectories of these vortex dipoles are ring-structured as described in [15, 16]. The annihilation of vortices or the vortex dipole in the BEC has been mentioned in a number of theoretical studies [17–19]. However, there is the lack of extensive study on this topic and more importantly, no definite signatures of vortex dipole annihilation were observed in the experiment [3]. The study of vortex dipole annihilation will shed light on the process which influences the separation between the vortex and antivortex, as well as the conditions for annihilation along with other phenomena arising from the dynamics of vortex dipoles.

In this work, we present analytical as well as numerical results related to vortex dipole annihilation for an oblate BEC at zero temperature. The results are obtained using the Gross–Pitaevskii (GP) equation. In section 2 of this paper, we provide a brief description of the two-dimensional (2D) GP equation and vortex dipole solutions. Condensates with a diametric vortex dipole and a grey soliton are studied, and this is described in section 3. Section 3 contains studies done in the strong as well as weak interacting systems. The annihilation of vortex dipoles is analysed from the energies obtained from the analytical calculations. The numerical results, confirming the analytic results, are discussed in section 4, and we then conclude.

2. Superfluid vortex dipole and its generation

In the mean-field approximation, the dynamics of a dilute BEC is very well described by the GP equation:

$$i\hbar\partial_t\Psi(\mathbf{r},t) = [\mathcal{H} + U|\Psi(\mathbf{r},t)|^2]\Psi(\mathbf{r},t), \tag{1}$$

where $\mathcal{H}$, U and Ψ are the single-particle Hamiltonian, interaction strength and order parameter of the condensate, respectively. The order parameter, Ψ, is normalized to N, the total number of atoms in the condensate. In the present case, the single-particle Hamiltonian $\mathcal{H}$ consists of the kinetic energy operator, an axis-symmetric harmonic trapping potential and a Gaussian obstacle potential, that is,

$$\mathcal{H} = -\frac{\hbar^2}{2m}\nabla^2 + \frac{m\omega^2}{2}(x^2 + \alpha^2y^2 + \beta^2z^2) + V_{\text{obs}}(x,y,t), \tag{2}$$

where α and β are the anisotropies along the y- and z-axes, respectively, m is the mass of particles used in the condensate, ω is the trapping potential frequency along the x-axis and $V_{\text{obs}}(x,y,t)$ is the repulsive Gaussian obstacle potential. Experimentally, a blue-detuned laser beam is used to generate the $V_{\text{obs}}(x,y,t)$, and it can be written as

$$V_{\text{obs}}(x,y,t) = V_0(t)\exp\left[-2\frac{(x-vt)^2+y^2}{w_0^2}\right], \tag{3}$$

where $V_0(t)$ is the potential at the centre of the Gaussian obstacle at time t, v is the velocity of the obstacle along the x-axis, and w_0 is the radius of the repulsive obstacle potential. In this work, we consider the motion of the obstacle along the x-axis only. Defining the oscillator length of the trapping potential as $a_{\text{osc}} = \sqrt{\hbar/(m\omega)}$ and considering $\hbar\omega$ as the unit of energy, we can then rewrite the equations in a dimensionless form with the transformations $\tilde{\mathbf{r}} = \mathbf{r}/a_{\text{osc}}$, $\tilde{t} = t\omega$, and the transformed order parameter assumes the form

$$\phi(\tilde{\mathbf{r}},\tilde{t}) = \sqrt{\frac{a_{\text{osc}}^3}{N}}\Psi(\mathbf{r},t). \tag{4}$$

For the sake of notational simplicity, hereafter, we denote the scaled quantities without the tilde in the rest of the paper. In a pancake-shaped trap, $\alpha = 1$ and $\beta \gg 1$, and the order parameter can then be written as

$$\phi(\mathbf{r},t) = \psi(x,y,t)\zeta(z)\exp(-i\beta t/2), \tag{5}$$

where $\zeta(z) = (\beta/(2\pi))^{1/4}\exp(-\beta z^2/4)$. Equation (1) is then reduced to the 2D form

$$\left[-\frac{1}{2}\left(\frac{\partial^2}{\partial x^2} + \frac{\partial^2}{\partial y^2}\right) + \frac{x^2+y^2}{2} + \frac{V_{\text{obs}}(x,y,t)}{\hbar\omega} + u|\psi(\mathbf{r},t)|^2 - i\frac{\partial}{\partial t}\right]\psi(\mathbf{r},t) = 0, \tag{6}$$

where $u = 2aN\sqrt{2\pi\beta}/a_{\text{osc}}$, with a being the s-wave scattering length, is the modified interaction strength. In this work, we consider a condensate consisting of ^{87}Rb atoms in the $F = 1$, $m_F = -1$ state, with $a = 99a_0$ [20]. We have neglected a constant term corresponding to the energy along the axial direction as it only shifts the energies and chemical potentials by a constant without affecting the dynamics. We solve this equation numerically using the Crank–Nicolson method [21].

There are several theoretical and experimental proposals to generate vortices in non-rotating traps. These include stirring of the condensate using a blue-detuned laser or several laser beams [3, 15], an adiabatic passage [22], Raman transitions in binary condensate systems [23], laser beam vortex guiding [24] and phase imprinting [5]. Among these methods, the easiest way to nucleate vortex dipoles is by stirring a BEC with a blue-detuned laser beam. When the velocity of the laser beam exceeds a critical velocity, vortex–antivortex pairs are released from the localized dip in the number density created due to the laser beam. These vortex dipoles then move through the BEC and exhibit various interesting dynamics [4, 15, 25]. The critical velocity depends on the number density, width and intensity of the laser beam and the frequency of the trapping potential. This nucleation process exhibits a high degree of coherence and stability, allowing us to map out the annihilation of the dipoles. In an axis-symmetric trap, a vortex dipole is a metastable state of superfluid flow with a long lifetime.

3. Condensates with a vortex dipole or grey soliton

To analyse the vortex dipole annihilation, we consider a model system where the vortex–antivortex dipole pair and grey soliton, which may be generated when the annihilation of vortex dipole occurs, are static. However, we vary the distance of separation and examine the energy of the total system. The present system can be studied under two regimes: a strongly interacting system and a weakly interacting system. The strongly interacting system is studied considering ϕ with the Thomas–Fermi (TF) approximation, and the weakly interacting system is studied considering the Gaussian form of ϕ.

3.1. Strongly interacting system with TF approximation

For the $Na/a_{\text{osc}} \gg 1$ case, we use the TF approximation to determine the steady-state density profile and energy of the condensate. To begin with, we consider a condensate with a vortex dipole and later with a grey soliton.

3.1.1. Diametric vortex dipole. We consider a condensate consisting of N atoms in a purely harmonic potential

$$V(x,y) = \frac{x^2+y^2}{2}. \tag{7}$$

Consider that the condensate has a vortex dipole, consisting of a vortex and an antivortex located at $(0, v_2)$ and $(0, -v_2)$, respectively. The cores of the vortex and antivortex can be approximated as circular regions centred around $(0, v_2)$ and $(0, -v_2)$ and with radii equal to the coherence length ξ. At the cores, we consider the density to be equal to zero. Hence, we use the TF approximation and adopt the following piecewise ansatz for the density of the condensate:

$$n(x,y) = \begin{cases} 0 & \text{for} \quad x^2+y^2 > R^2 \\ 0 & \text{for} \quad [x^2+(y\pm v_2)^2] \leqslant \xi^2 \\ \left[\frac{\mu - V(x,y)}{u}\right] & \text{for} \quad \begin{cases} x^2+y^2 \leqslant R^2 \text{ and} \\ [x^2+(y\pm v_2)^2] > \xi^2, \end{cases} \end{cases} \tag{8}$$

where $R = \sqrt{2\mu}$ is the spatial extent of the condensate in the TF approximation, and $\xi = 1/R$ is the coherence length at the centre of the trap. Normalizing this ansatz yields

$$\frac{\pi\left(2 - 4R^4 + R^8 + 4R^2 v_2^2\right)}{4R^4 u} = 1. \tag{9}$$

This equation defines the radius of the condensate. The TF ansatz can be used to calculate the total potential energy arising from the regions outside the cores of the vortices and is given as

$$E_0 = \frac{\pi\left[1 - 3R^8 + R^{12} + 3R^2 v_2^2\left(2 + R^2 v_2^2\right)\right]}{12R^6 u}. \tag{10}$$

The main energy contribution from the vortex dipole is the kinetic energy due to the velocity field associated with it. This energy can be approximated as [26]

$$E_{\mathrm{KE}} = \frac{R^2}{u}\mathrm{Log}\left(\frac{2v_2}{\xi}\right). \tag{11}$$

This relation is valid when $\xi \ll v_2 \ll R$ and in this work, $\xi \sim 0.06$ and $R = 15.5a_{\mathrm{osc}}$. In order to estimate the energy contributions from the cores of the vortices, we approximate the density within the cores as

$$n(x,y) = \begin{cases} \dfrac{2n_0[x^2 + (y - v_2)^2]}{x^2 + (y - v_2)^2 + \xi^2} & \text{for } [x^2 + (y - v_2)^2] < \xi^2 \\ \dfrac{2n_0[x^2 + (y + v_2)^2]}{x^2 + (y + v_2)^2 + \xi^2} & \text{for } [x^2 + (y + v_2)^2] < \xi^2, \end{cases} \tag{12}$$

where n_0 is the average TF density on the circle $x^2 + (y \pm v_2)^2 = \xi^2$. Assuming that the normalization is still defined by equation (9), equation (12) can be used to calculate energy contribution from the core region. The energy within the core consists of

$$E_{\mathrm{c}}^{\mathrm{q}} = \frac{6\pi n_0}{8}, \tag{13}$$

$$E_{\mathrm{c}}^{\mathrm{tr}} = \pi\xi^4(\mathrm{Log}[4] - 1)n_0, \tag{14}$$

$$E_{\mathrm{c}}^{\mathrm{int}} = 2\pi u\xi^2(3 - \mathrm{Log}[16])n_0^2, \tag{15}$$

where $E_{\mathrm{c}}^{\mathrm{q}}$, $E_{\mathrm{c}}^{\mathrm{tr}}$ and $E_{\mathrm{c}}^{\mathrm{int}}$ are the energies arising from the quantum pressure, trapping potential and interaction within the core region, respectively. Thus, the total energy of the condensate with a vortex dipole is

$$E_{\mathrm{vd}} = E_0 + E_{\mathrm{KE}} + E_{\mathrm{c}}^{\mathrm{q}} + E_{\mathrm{c}}^{\mathrm{tr}} + E_{\mathrm{c}}^{\mathrm{int}}. \tag{16}$$

The variation of E_{vd} as a function of v_2 is shown in figure 1.

3.1.2. Grey soliton. For the grey soliton extending from $(0, -v_2)$ to $(0, v_2)$ along the y-axis, we use the following piecewise ansatz in the TF approximation:

$$n(x,y) = \begin{cases} 0 & \text{for } x^2 + y^2 > R^2, \\ \left[\frac{\mu - V(x,y)}{u}\right] & \text{for } \begin{cases} x^2 + y^2 \leqslant R^2, \\ |x| > \xi, \\ |y| > v_2, \end{cases} \\ \left[\frac{\mu - V(x,y)}{u}\right]\frac{2x^2}{x^2+\xi^2} & \text{for } |x| \leqslant \xi \text{ and } |y| \leqslant v_2. \end{cases} \tag{17}$$

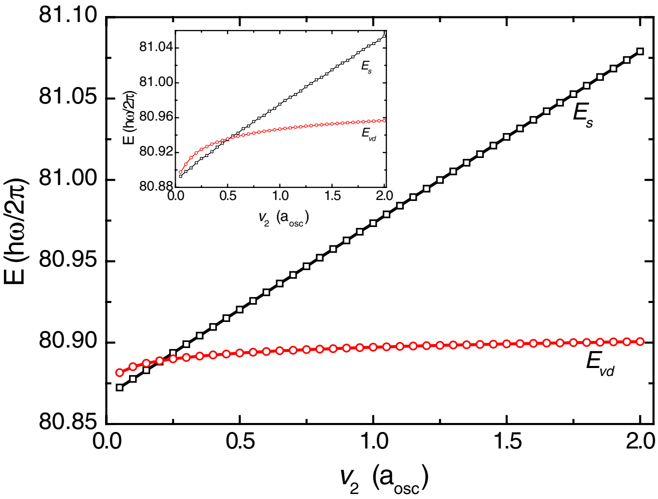

Figure 1. Comparing the energy of the vortex dipole and band soliton under TF approximations. The crossover in energy can be seen through the ansatz chosen and the analytical expressions obtained. The inset shows the variation of energy obtained by solving the GP equation numerically. The difference in the value of v_2 for the crossover in energy is due to the too-ideal wavefunction considered for analytical calculations.

And the normalization condition leads to the following constraint on the radius of the condensate:

$$\frac{1}{12R^3 u}\left[3\pi R^7 + 4v_2\left(10 + 6R^4 - 3\pi(1 + R^4)(-2 + \pi)R^2 v_2^2\right)\right] = 1. \tag{18}$$

For the grey soliton, other than the quantum pressure, there is no need to separate out the energy associated with the trapping and interaction potential within the soliton. So, the total energy of the system is

$$E_{\mathrm{s}} = E_0 + E_{\mathrm{c}}^{\mathrm{q}}, \tag{19}$$

where E_0 is the potential energy associated with the system and $E_{\mathrm{c}}^{\mathrm{q}}$ is the energy arising from the quantum pressure. These are given as

$$E_0 = \iint \left[V(x,y)n(x,y) + \frac{u}{2}n(x,y)^2\right]\mathrm{d}x\,\mathrm{d}y,$$
$$E_{\mathrm{c}}^{\mathrm{q}} = \frac{1}{2}\int_{-\xi}^{\xi}\left[\int_{-v_2}^{v_2}|\nabla_{xy}\sqrt{n(x,y)}|^2\mathrm{d}y\right]\mathrm{d}x. \tag{20}$$

From the expression $n(x,y)$ in equation (17), we obtained

$$E_0 = \frac{1}{180R^5 u}\{15\pi R^{11} + 3[236 - 75\pi + 20(19 - 6\pi)R^4 + 15(8 - 3\pi)R^8]v_2 + 10R^2[-28 + 9\pi + 6(-3 + \pi)R^4]v_2^3 - 9(-4 + \pi)R^4 v_2^5\} \tag{21}$$

$$E_{\mathrm{c}}^{\mathrm{q}} = -\frac{(8 + 3\pi)v_2(-3R^2 + 3\xi^2 + v_2^2)}{48u\xi}. \tag{22}$$

Interestingly, $E_{\mathrm{c}}^{\mathrm{q}}$ has a $1/\xi$ dependence, which is to be expected, as smaller ξ implies a larger density variation and translates to higher quantum pressure.

For illustration, the vortex dipole and grey soliton inside the condensate are shown in figure 2. The vortex dipole is

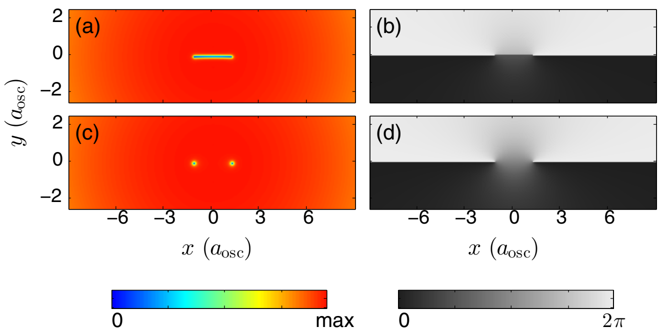

Figure 2. Band soliton (top) and vortex dipole (bottom) with the density profile (left) and phase profile (right) obtained numerically.

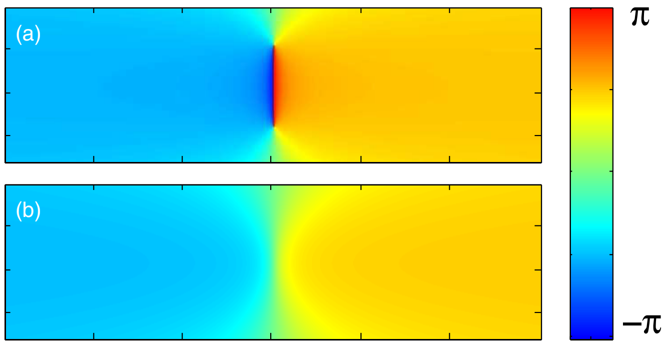

Figure 3. Phase pattern resulting due to a (a) vortex dipole and (b) grey soliton.

located at (1, 0) and (−1, 0), while the grey soliton extends from (−1, 0) to (1, 0) along the x-axis. In the case of the vortex dipole, the phase varies from 0 to 2π, if one goes around the point of singularity, whereas in the case of the grey soliton, there is a phase discontinuity of π along the line forming the soliton. The number density at the point of singularity is zero. In figure 1, E_s is plotted as a function of v_2 and the values vary from 0.05 $a_{\rm osc}$ to 2.0 $a_{\rm osc}$. From the figure, it is evident that for $v_2 \leqslant 0.2$, the value of $E_{\rm vd}$ is higher than E_s and hence, the grey soliton is the energetically favoured state of the system. However, when $v_2 > 0.2$, the vortex dipole state is the energetically favourable state. This analytical result provides a compelling reason to study the annihilation of vortex dipoles and formation of grey solitons.

3.2. Weakly interacting system with Gaussian approximation

In the $Na/a_{\rm osc} \ll 1$ regime, a simplistic model of a vortex dipole in the BEC of trapped dilute atomic gases can be considered as the superposition of harmonic oscillator eigenstates. The minimalist wavefunction which supports a vortex and an antivortex at the coordinates $(-a/c, -\sqrt{b/d})$ and $(-a/c, \sqrt{b/d})$ is

$$\psi(x, y, t) = \mathrm{e}^{-\mathrm{i}\mu t}(\mathrm{i}a - b + \mathrm{i}cx + \mathrm{d}y^2)\,\mathrm{e}^{-(x^2+y^2)/f}, \quad (23)$$

where a, b, c, d and f are positive variational parameters and μ is the chemical potential of the system. The wavefunction is a superposition of the scaled ground state and the first and second excited states of a harmonic oscillator along the x- and y-axes, respectively. The wavefunction is ideal for weakly interacting condensates.

We have considered that the vortex and antivortex are located on the diameter of the condensate. Without loss of generality, we consider the diameter as coinciding with the y-axis, which is equivalent to $a = 0$ in equation (23). Such an assumption does not modify qualitative descriptions, but expressions are far less complicated. The wavefunction is then

$$\psi(x, y, t) = \mathrm{e}^{-\mathrm{i}\mu t}[-b + \mathrm{i}cx + \mathrm{d}y^2]\,\mathrm{e}^{-(x^2+y^2)/f}. \quad (24)$$

The nontrivial phase of the wavefunction θ is discontinuous along the $x = 0$ line for $-\sqrt{b/d} \leqslant y \leqslant \sqrt{b/d}$. Across the discontinuity, there is a phase change from $-\pi$ to π as we traverse along the x-axis from 0^- to 0^+, and this phase variation is shown in figure 3. So, there is a discontinuity across the y-axis and this is the typical phase pattern associated with vortex dipoles. For the present case, the ground state wavefunction is

$$\psi_{\rm g}(x, y, t) = -b\mathrm{e}^{-\mathrm{i}\mu t}\mathrm{e}^{-(x^2+y^2)/f}, \quad (25)$$

and from the normalization condition $\int_{-\infty}^{\infty}\int_{-\infty}^{\infty}|\psi_{\rm g}|^2\,\mathrm{d}x\,\mathrm{d}y = 1$, we obtain the constraint equation

$$b^2 = \frac{2}{f\pi}. \quad (26)$$

For general considerations, rewrite the additional term as

$$\delta\psi(x, y, t) = \mathrm{e}^{-\mathrm{i}\mu t}(\mathrm{i}cx + \mathrm{d}y^2)\,\mathrm{e}^{-(x^2+y^2)/f}, \quad (27)$$

so that the total wavefunction $\psi = \psi_{\rm g} + \delta\psi$, where $\delta\psi$ represents an elementary excitation of the condensate. We can calculate the total energy of the system, without the obstacle potential, as

$$E_{\rm vd} = \int_{-\infty}^{\infty}\int_{\infty}^{\infty}\left[\frac{1}{2}|\nabla_\perp\psi(x, y)|^2 + \frac{x^2+y^2}{2}|\psi(x, y)|^2 + u|\psi(x, y)|^4\right]\mathrm{d}x\,\mathrm{d}y. \quad (28)$$

This is the energy of the condensate with a vortex dipole with the assumption that it is a weakly interacting system. Energy without the vortex may be calculated trivially [11]. In general, the energy added to the system due to the vortex dipole is not large compared to the total, and for obvious reasons, the angular momentum of the condensate is still zero.

A slight modification to the wavefunction can describe a solitonic solution along the y-axis. The form of the modified wavefunction is

$$\psi(x, y) = [b + \mathrm{i}cx + \mathrm{d}y^2]\,\mathrm{e}^{-(x^2+y^2)/f}, \quad (29)$$

where except for the change in the sign of b, all the terms remain unaltered as in equation (23). It is a grey soliton as the density $n \propto (b + \mathrm{d}y^2)^2 + (cx)^2$ has a dip but is different from zero. The phase varies smoothly from $-\pi/2$ to $\pi/2$ along the normal to the line which connects $(0, -\sqrt{b/d})$ and $(0, \sqrt{b/d})$. This phase variation is shown in figure 3(b).

Using the wavefunction in equation (29), we can then evaluate the total energy of the system $E_{\rm gs}$ and calculate the energy difference between two possible states of the system:

$$\Delta E = E_{\rm vd} - E_{\rm gs}, \quad (30)$$

which after evaluation is

$$\Delta E = \frac{\mathrm{b}\mathrm{d}f^2\pi}{256}[64b^2u + 15\mathrm{d}^2f^2u + 8f(8 + c^2u)]. \qquad (31)$$

The most general solution is that when all the constants are positive, then $\Delta E > 0$ and the grey soliton is lower in energy. This shows that when the vortex and antivortex collide, it is energetically favourable for them to decay into the grey soliton. As discussed in the results section, this is confirmed in the numerical calculations.

The analysis so far is for an ideal system at zero temperature, where we have neglected the quantum and thermal fluctuations and perturbations from imperfections. In addition, there is dissipation from three-body collision losses in the condensates of dilute atomic gases.

4. Numerical results

For the numerical computation, we choose ^{87}Rb with $N = 2 \times 10^6$ atoms. The trapping potential and obstacle laser potential parameters are similar to those considered in [3], i.e. $\omega/(2\pi) = 8$ Hz, $\beta = 11.25$, $V_0(0) = 93.0\ \hbar\omega$ and $w_0 = 10\,\mu$m. To nucleate the vortices on the edges of the condensate, the obstacle potential $V_{\rm obs}$ is initially located at $(-12.5a_{\rm osc}, 0)$ and moves along the x direction at a constant velocity with decreasing intensity, until $V_{\rm obs}$ vanishes at $(5.18a_{\rm osc}, 0)$.

4.1. Vortex dipole nucleation

We study the nucleation of vortices by $V_{\rm obs}$ with the translation speed v ranging from 80 to 200 μm s^{-1}. Vortices are not nucleated when the speed is 80 μm s^{-1}. However, a vortex–antivortex pair or a vortex dipole is nucleated when the speed is in the range of $90\,\mu\text{m s}^{-1} < v < 140\,\mu\text{m s}^{-1}$. Increasing the speed of the obstacle generates two pairs of vortex dipoles when $140\,\mu\text{m s}^{-1} \leqslant v < 160\,\mu\text{m s}^{-1}$, and more than two pairs when $v \geqslant 160\,\mu\text{m s}^{-1}$. In other words, the number of vortex dipoles created can be controlled with the speed of the obstacle. The creation of vortex dipoles above a critical speed v_c is natural as the vortex nucleation must satisfy the Landau criterion [27]. The density and phase of the condensate after the nucleation of the vortex dipole for $v = 120\,\mu\text{m s}^{-1}$ are shown in figure 4. The figure clearly shows the nucleation dynamics of the vortex dipoles.

From numerical calculations, we have determined $v_c \approx 90\,\mu\text{m s}^{-1}$. This is, however, less than the local acoustic velocity of the medium $s = \sqrt{nU/m}$, which depends on the local condensate density. This also explains the reason for the predominant vortex dipole nucleation around the edge of the condensate where n is lower and s is accordingly lower.

4.2. Vortex dipole annihilation

To determine the energetically preferred state of the system, we examine the energy of the condensate with the vortex dipole and grey soliton as a function of the separation v_2. The result is shown as the inset plot in figure 1. As in the TF calculations, the vortex dipole is the stable solution for larger v_2, but for $v_2 < 0.5a_{\rm osc}$, a grey soliton is the stable solution. However, in the numerical results, the critical value of v_2 at which the vortex soliton overtakes the grey soliton as the stable solution is higher than the TF values. This may be an account of the piecewise nature of the TF ansatz.

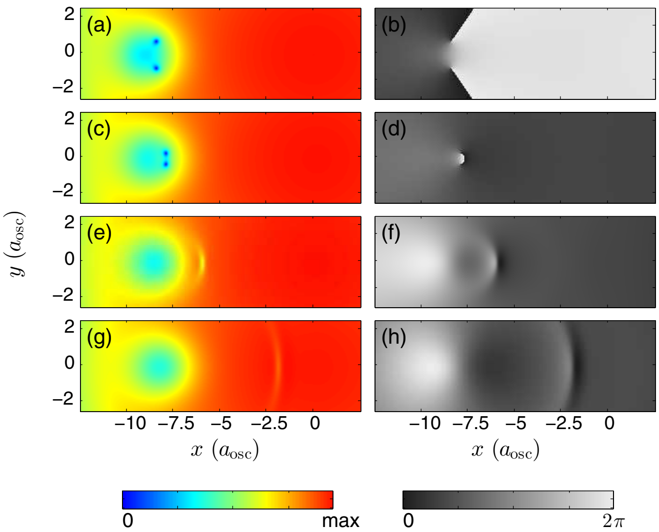

Figure 4. A vortex dipole is nucleated when the obstacle potential traverses the condensate at a speed of 120 μm s^{-1}. The vortex dipole, however, passes through and overtakes the obstacle. Later, as seen in (e), the vortex dipole annihilates and generates a grey soliton. The figures in the left panel show the density distribution and those on the right show the phase pattern of the condensate. From top to bottom, $t = 2.9$, 3.1, 3.3 and 3.5, respectively.

It is observed that the vortex dipole annihilation is critically dependent on the initial conditions of the nucleation, in particular, the vortex–antivortex separation, v_2. The annihilation occurs when the vortex dipole is generated with $v_2 < 0.5a_{\rm osc}$, which is consistent with the analytical results and solutions of the time-independent GP equation. The initial v_2 is, however, dependent on the velocity v of the obstacle potential. For this reason, the annihilation events are observed only for a specific range of v. As an example, the annihilation event when v is 120 μm s^{-1} is shown in figure 4. In figure 4, we can notice the density minima arising from the annihilation and propagating away from the obstacle potential.

A reliable and qualitative way to describe the occurrence of annihilation could be achieved by observing the density at the cores of the vortex and antivortex which form the dipole. For the vortex, the matter density at the core when v is 120 μm s^{-1} is shown in figure 5. In the plot, at time $\approx$3.19 (scaled units), the core density starts increasing. This is because the core starts to fill in with the atoms from around the vortex after the annihilation. This filling process may not complete till it reaches the edge of the condensate and gets reflected inside the condensate.

After the annihilation of the vortex–antivortex dipole pair, a grey soliton gets generated. We can clearly observe the propagation of this soliton in figure 6. The speed of propagation is 2000 μm s^{-1}, which is similar to the speed of sound in a condensate. During the propagation, the number density on the location of the soliton increases, which is clearly visible from figure 6 as well as from figure 5. To estimate the energy

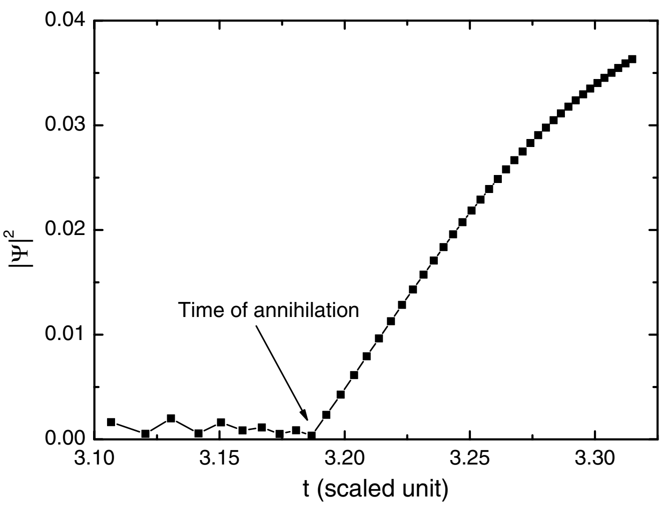

Figure 5. Density variation at the core of the vortex with time. After the vortex dipole annihilation, the density increases till it reaches the bulk value. The values correspond to the obstacle speed of $120\,\mu$m s^{-1}. After annihilation, the number density has been considered from the location of minimum density. The x-axis denotes the time elapsed from the starting of the obstacle at $(-12.5a_{\mathrm{osc}}, 0)$.

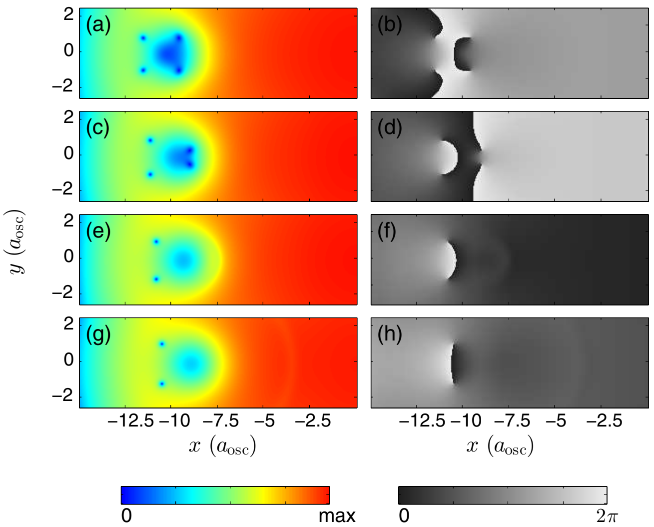

Figure 7. A vortex dipole is nucleated as the obstacle potential traverses the BEC with a speed of $160\,\mu$m s^{-1}. The figures in the left panel show the density with time, where time progresses from top to bottom. Figures in the right panel show the phase pattern of the condensate. From top to bottom, t = 1.6, 1.8, 2.0 and 4.2, respectively.

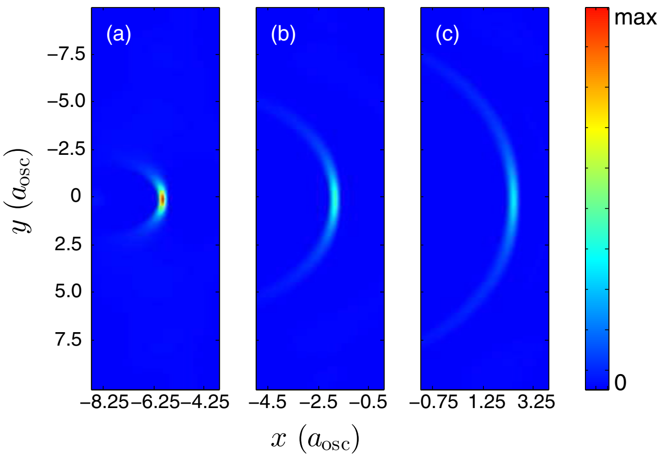

Figure 6. The propagation of the grey soliton after the annihilation of the vortex dipole. The higher the value, the higher is the number density dip at that point. From (a) to (c), t = 3.2, 3.4 and 3.6, respectively.

of the grey soliton, we have obtained the stationary state with the same position of vortex dipoles and the obstacle potential. The energy difference between the stationary and the dynamic state will provide us with the energy of the grey soliton, as discussed in [28]. The energy released due to the annihilation is 0.004 $\hbar\omega$ and is similar to the energy difference observed in figure 1, obtained from the TF approximation. We have also observed that this soliton gets reflected back and forth from the edge of the condensate. This reflection is similar to the reflection of any pulse from the circular edges.

It is to be mentioned that for the parameters considered in this work, the speed of sound is $2190\,\mu$m s^{-1} and the coherence length of the system is $\sim 0.229\,\mu$m. These are in agreement with the minimum separation between the vortex and antivortex observed in the analytical work. The energy gap for the vortex dipole and grey soliton of the same size matches with the estimates from the ansatz based on the TF approximation. The vortex dipole annihilation is not only observed for $V_{\mathrm{obs}} = 120\,\mu$m s^{-1}, it also occurs for other obstacle velocities as well. Once such case, for $V_{\mathrm{obs}} = 160\,\mu$m s^{-1}, is shown in figure 7. In this case, the difference in energy of the vortex dipole and grey soliton is 0.0025 $\hbar\omega$.

One observation which is common to all the vortex dipoles getting annihilated is the nature of their trajectories. All of them traverse through V_{obs}, whereas the ones which do not get annihilated avoid V_{obs}. The vortex dipoles are generally nucleated at the aft region of the V_{obs} where there is a trailing superflow. When nucleated very close to each other ($v_2 < 0.5$) and with high velocity, the mutual force further increases the velocity of the vortex dipoles. At the same time, it decreases the distance separating the vortex and antivortex. So, the kinetic energy is high enough to surpass V_{obs}. Later, at some point, the vortex and antivortex separation is less than ξ, and they annihilate.

4.3. Effect of noise and dissipation

In the numerical studies, the annihilation events are not rare. But this is in contradiction with the experimental results of Neely and collaborators [3]—they observed no signatures of annihilation events. One possible reason is that our numerical calculations are too ideal, and an immediate remedy is to include quantum and thermal fluctuations. The rigorous way to study these fluctuations is to use methods like the truncated Wigner approximation [29]; however, in this work, we use the simple but widely accepted method of adding white noise [30, 31], as white noise constitutes random fluctuations and is

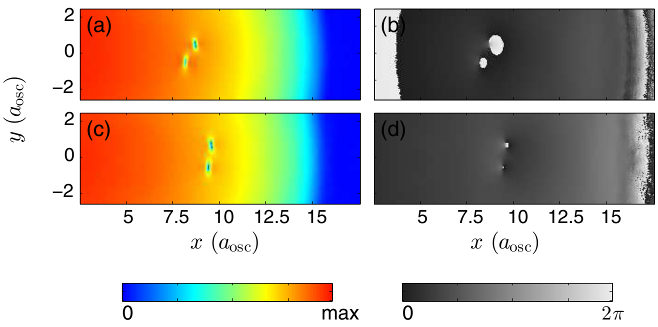

Figure 8. The figures in the left (right) panel show the density (phase) of the condensate in the presence of white noise at time t = 4.1 (top) and 4.2 (bottom). Lack of diametrical symmetry of the position of the vortex dipole can be observed. This reduces the possibility of an annihilation event significantly. In this case, the speed of the obstacle is 180 μm s^{-1}.

hence able to change the number density of the condensate.It is added numerically using a random number generator. We have used the Mersenne Twister pseudo-random number generator. The strength of random noise used in our numerical calculation is 0.01% of the maximum density of the condensate. This noise is added/subtracted at every time-step of the real-time evolution of the condensate. One immediate outcome is that the symmetry in the position of the vortex and antivortex is lost. The superflow around the vortex is no longer a mirror reflection of the antivortex, which was nearly the case without the white noise. The deviations are shown for an example case in figure 8, where $V_{\rm obs} = 180\,\mu$m s^{-1}. This change in path leads to the suppression of annihilation events of the vortex dipoles. We have also studied the effect of large white noise (10%) added at the beginning, and avoided adding any noise in the subsequent time-steps. In such cases, the noise gets damped throughout the condensate and there are no observable influences on the annihilation event.

The other important effect is the loss of atoms from the trap. We have examined the effect of loss terms, which arise from inelastic collisions in the condensate. There are two types of inelastic collisions that lead to the loss of atoms from the trap: the two-body inelastic collision loss and the three-body loss. To model the effect of loss of atoms from the trap, we add the loss terms

$$\frac{-i\hbar}{2}[K_2|\Psi(\mathbf{r},t)|^2 + K_3|\Psi(\mathbf{r},t)|^4], \qquad (32)$$

to the Hamiltonian $\mathcal{H}$. Based on the previous work [32], for ^{87}Rb, the inelastic two-body loss rate coefficient $K_2 = 4.5 \times 10^{-17}$cm^{3}s^{-1} and the inelastic three-body loss rate coefficient $K_3 = 3.8 \times 10^{-29}$ cm^6 s^{-1}. With trap loss, the annihilation events continue to occur. However, during the destructive time of flight observations in the experiments, the decreased atom numbers may lower the contrast and reduce the possibility of observing an annihilation event.

5. Conclusions

When an obstacle moves through a condensate above a critical speed, it nucleates the vortex dipoles, and the number of dipoles seeded depends on the obstacle velocity. Depending on the initial condition of nucleation, vortex and antivortex annihilation events occur under ideal conditions: at zero temperature, at no loss and without noise. These events are found to be energetically favourable theoretically and observed numerically. In the case of weakly interacting condensates, the energy of the grey soliton is always less than that of the vortex dipole, and provides higher possibility for annihilation events. Similarly, in the case of strongly interacting condensates, we use TF approximation to study the system and find that if the separation between the vortex–antivortex pair is less then the coherence length, the energy of the vortex dipole is more than that of the grey soliton, and this leads to annihilation. The generated grey soliton propagates through the condensate and shows the phenomena of reflection from the circular edge of the condensate. The speed of propagation is found to be similar to the speed of sound in a BEC. However, noise, thermal fluctuations and dissipation destroy the superflow reflection symmetry around the vortex and antivortex. Breaking the symmetry reduces the possibility of annihilation events and may explain the lack of annihilation events in experimental observations.

Acknowledgments

The numerical calculations reported in this paper have been performed on a 3 TeraFlop high-performance cluster at the Physical Research Laboratory (PRL), Ahmedabad. The authors also thank the anonymous reviewers for valuable comments and suggestions.

References

[1] Anglin J R and Ketterle W 2002 *Nature* **416** 211
[2] Matthews M R, Anderson B P, Haljan P C, Hall D S, Wieman C E and Cornell E A 1999 *Phys. Rev. Lett.* **83** 2498
[3] Neely T W, Samson E C, Bradley A S, Davis M J and Anderson B P 2010 *Phys. Rev. Lett.* **104** 160401
[4] Freilich D V, Bianchi D M, Kaufman A M, Langin T K and Hall D S 2010 *Science* **329** 1182
[5] Andrelczyk G, Brewczyk M, Dobrek Ł, Gajda M and Lewenstein M 2001 *Phys. Rev.* A **64** 043601
[6] Brand J and Reinhardt W P 2002 *Phys. Rev.* A **65** 043612
[7] Middelkamp S, Torres P J, Kevrekidis P G, Frantzeskakis D J, Carretero-González R, Schmelcher P, Freilich D V and Hall D S 2011 *Phys. Rev.* A **84** 011605
[8] Aioi T, Kadokura T, Kishimoto T and Saito H 2011 *Phys. Rev.* X **1** 021003
[9] Couder Y and Basdevant C 1986 *J. Fluid. Mech.* **173** 225
[10] Grier D G 2003 *Nature* **424** 810
[11] Pethick C J and Smith H 2008 *Bose–Einstein Condensation in Dilute Gases* (Cambridge: Cambridge University Press)
[12] Fetter A L 2009 *Rev. Mod. Phys.* **81** 647
[13] Sonin E B 1987 *Rev. Mod. Phys.* **59** 87
[14] Alekseenko S V, Kuibin P A and Okulov V L 2007 *Theory of Concentrated Vortices* (New York: Springer)
[15] Jackson B, McCann J F and Adams C S 1999 *Phys. Rev.* A **61** 013604
[16] Li W, Haque M and Komineas S 2008 *Phys. Rev.* A **77** 053610
[17] Nazarenko S and Onorato M 2007 *J. Low Temp. Phys.* **146** 146
[18] Rooney S J, Blakie P B, Anderson B P and Bradley A S 2011 *Phys. Rev.* A **84** 023637

[19] Nowak B, Sexty D and Gasenzer T 2011 *Phys. Rev.* B **84** 020506
[20] van Kempen E G M, Kokkelmans S J J M F, Heinzen D J and Verhaar B J 2002 *Phys. Rev. Lett.* **88** 093201
[21] Muruganandam P and Adhikari S K 2009 *Comput. Phys. Commun.* **180** 1888
[22] Dum R, Cirac J I, Lewenstein M and Zoller P 1998 *Phys. Rev. Lett.* **80** 2972
[23] Marzlin K P, Zhang W and Wright E M 1997 *Phys. Rev. Lett.* **79** 4728
[24] Staliunas K 2000 *Appl. Phys.* B **71** 555
[25] Kuopanportti P, Huhtamäki J A M and Möttönen M 2011 *Phys. Rev.* A **83** 011603
[26] Zhou Q and Zhai H 2004 *Phys. Rev.* A **70** 043619
[27] Lifshitz E M and Pitaevskii L P 1980 *Statistical Physics, Part* 2 (Oxford: Pergamon)
[28] Parker N G and Adams C S 2005 *Phys. Rev. Lett.* **95** 145301
[29] Martin A D and Ruostekoski J 2010 *Phys. Rev. Lett.* **107** 194102
[30] Sasaki K, Suzuki N, Akamatsu D and Saito H 2009 *Phys. Rev.* A **80** 063611
[31] Kadokura T, Aioi T, Sasaki K, Kishimoto T and Saito H 2012 *Phys. Rev.* A **85** 013602
[32] Burke J P, Bohn J L, Esry E D and Greene C H 1998 *Phys. Rev. Lett.* **80** 2097